Development of Graphene Encapsulated NiMo Alloys as Acid-stable Catalysts for Efficient Hydrogen Production

Kailong Hu

February 2020

Development of Graphene Encapsulated NiMo Alloys as Acid-stable Catalysts for Efficient Hydrogen Production

Kailong Hu

Doctoral Program in Applied Physics

Submitted to the Graduate School of
Pure and Applied Sciences
in Partial Fulfillment of the Requirements
for the Degree of Doctor of Philosophy in
Engineering

at the
University of Tsukuba

Abstract

Hydrogen production from water electrolysis is one of the most promising approaches to meet the booming global demand for clean and sustainable hydrogen energy. Compared with traditional steam reforming method, the renewable power supplied water electrolysis provides a “zero-emission” process for hydrogen production. Development of non-noble- and acid-stable-metal catalysts for hydrogen evolution reaction (HER) is important to reduce the overall cost of large-scale hydrogen productions by state-of-the-art proton exchange membrane (PEM) water electrolyzers. PEM water electrolysis has been considered to be the next-generation technology for hydrogen production as the advantages of high hydrogen purity (>99.99 vol.%), fast dynamic response, high current density (~ 5 A cm^{-2}), high discharge hydrogen pressure (30−76 bar), and no alkaline waste solution. Graphene encapsulation method has emerged as a promising approach to achieve acid-stable non-noble-metal HER catalysts, due to the chemically stable graphene as an efficient protective layer for undesired corrosions induced by proton penetration in acidic electrolytes. Optimizing the number of encapsulating graphene layers and the density of defects induced by chemical doing achieves the balance between corrosion resistance and catalytic activity, which retains the intrinsic HER activity and alleviates the undesired activity degradation by surface encapsulation.

However, several challenges still retain unsolved. For example, the HER mechanism of graphene-encapsulated catalysts in acidic electrolytes is not well studied so far. In addition, the influences of the layer number of encapsulating graphene, chemical doping, and structural defects on HER performances have not been systematically investigated and the optimal graphene layer number is not determined. In this dissertation, multiple synthesis methods, electrochemical measurements, and density functional theory (DFT) calculations towards the graphene-encapsulated NiMo catalysts have been summarized with an emphasis on my researches to make fundamental and systematical understandings of the mechanism of graphene encapsulation method to achieve acid-stable non-noble-metal HER catalysts.

Firstly, I designed and developed a novel two-step process to synthesize cost-efficient NiMo alloy with three-dimensional (3D) open porous structure as an efficient HER catalyst. The cost of synthesized precursor is as low as 37 JPY per gram, which shows a prospect for large-scale productions. NiMo alloy catalysts exhibits a platinum (Pt) comparable HER activity and excellent stability, i.e., a current density of 25 mA cm^{-2} retained for more than 12 days, in 1.0 M KOH electrolyte.

Secondly, the acid-soluble characteristic of NiMo alloy has been addressed by employing graphene as the protective layer for NiMo alloys. Encapsulation by 3 layers N-doped graphene achieves the optimal balance between corrosion resistance and catalytic activity. Experimental results indicate that NiMo alloy nanoparticles encapsulated by 3 layers N-doped graphene achieve a low potential of 80 mV vs. RHE to reach a current density of 10 mV cm^{-2} and a low Tafel slope value of 60 mV dec^{-1}; additionally, more than 92% of initial current density retained for 25 h in 0.5 M H_2SO_4, which confirms the remarkable acid resistance

ability and excellent HER activity.

Finally, the proton penetration through graphene layers, as the underlying reason of the corrosion of encapsulated NiMo catalysts under acidic media, has been investigated. Electrochemical experiments suggest that the resistance of proton penetration raised with increasing the number of graphene layers. DFT calculations indicate the doping-induced defects in graphene lattices are preferred penetration regions due to the low energy barrier for proton transfers. Additionally, the overall pathways and the energy barriers of proton penetration through various types of graphene lattice were further simulated and calculated. By observing proton penetration behaviour through electrochemical experiments and DFT simulations, the HER activity and corrosion of the graphene-encapsulated catalyst was found to be governed by the degree of proton penetration as determined by the number of encapsulating graphene layers.

This dissertation provides a new insight and fundamental understanding of the graphene encapsulation method to achieve acid-stable non-noble-metal HER catalysts, which contributes to the cost down of the catalysts used in PEM electrolyzers. The cost-efficient, flexible, and eco-friendly “zero-emission” hydrogen produced by renewable power supplied water electrolysis benefits to a sustainable, economic, and clean next-generation energy system.

Table of contents

List of figures

List of tables

Chapter 1 Introduction

1.1 Introduction of water electrolysis system for hydrogen productions

1.1.1 Hydrogen: the important chemical in our society

Hydrogen has been identified as one of the indispensable elements in modern industrial system. Today, 31% of the hydrogen produced in the world is used to produce ammonia[1], which is the main raw material in the fertilizer industry, through the Haber–Bosch process. The other 31% and 13% of hydrogen are consumed for oil refining and methanol production, and the rest 25% is accounted for other applications, such as the iron/coke production, the electronics industry, and the flat glass production[1, 2].

Hydrogen has also been considered as a viable alternative energy carrier for the eco-friendly next-generation energy system, which can generate electricity power for diverse energy demands, such as power grid, transportation, and industries[3]. Energy density is one of the crucial characteristics for large-scale and cost-efficient energy storages. As illustrated in **Figure 1.1**[4], the energy density of compressed hydrogen is about 140 MJ/kg, far higher than those of typical fossil fuels (50 MJ/kg)[5] and various batteries (less than 1.0 MJ/kg). Importantly, the conversion of chemical energy in hydrogen to electricity power through a fuel cell produces only water as byproduct, which contributes to cut down the emissions of greenhouse gases and achieve a "zero emission" energy system.

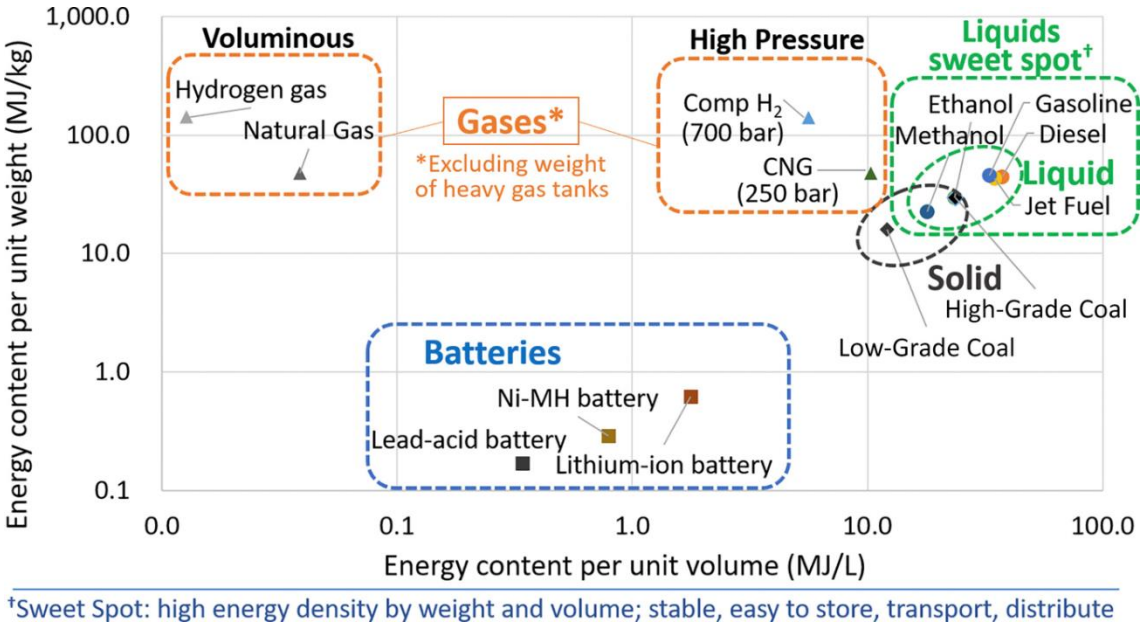

Figure 1.1 The energy density comparison of various energy carriers. Copyright 2018 Elsevier Inc.

The demand for hydrogen is about 70 million tons per year (70 Mt/yr) as depicted in **Figure 1.2**. Among various hydrogen production methods, the steam reforming of natural gas and the gasification of coal contribute to more than 98% of hydrogen production around the world. The production processes consume 6% of global natural gas and 2% of global coal supply[6]. As a result, the hydrogen production from fossil fuels is responsible for 830 million tons of carbon dioxide (CO_2) emissions per year. Although the hydrogen is a clean energy carrier, the production processes generate a huge amount of CO_2 emissions. In this case, the hydrogen cannot be account as a real "zero-emission" energy carrier. The development of low-carbon processes for hydrogen productions retains challenges.

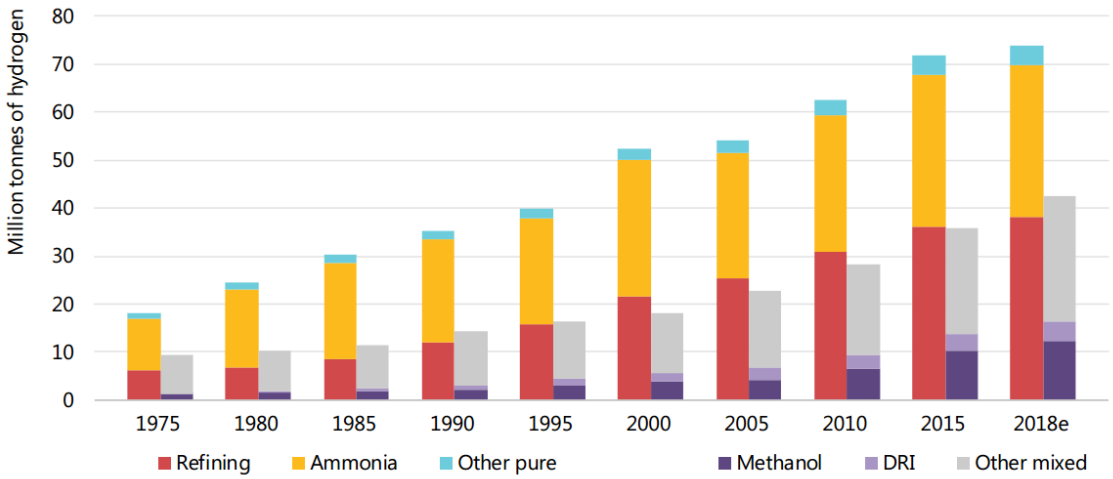

Figure 1.2[6] The annual global hydrogen demand since 1975. DRI represents direct reduced iron steel production. Refining, ammonia and "other pure" represent demand for specific applications that require hydrogen with only small levels of additives or contaminants tolerated. Methanol, DRI and "other mixed" represent demand for applications that use hydrogen as part of a mixture of gases, such as synthesis gas, for fuel or feedstock. Copyright 2019 International Energy Agency.

1.1.2 Hydrogen production from water electrolysis

One of the missing links for a renewable energy system is an efficient and flexible energy storage technology that can store the extra renewable energy during peak production times and can cover the energy demand during low power generation periods. This cooperated strategy of renewable energy and efficient energy carrier can smooth out the intermittent energy input from renewable sources, such as wind and sunlight, to achieve a stable and sustainable energy supply for our society[7].

Hydrogen has been considered as one of the most versatile energy storage systems and suitable energy carriers[8] among batteries, compressed gases, supercapacitors, pumped hydro. Recently, growing interest in the electrolysis of water for hydrogen productions mainly rest on its potential balance with power supplies from renewable energy sources[1, 5, 9], such as solar photovoltaics, hydro, wind energies, biomass. The

surplus electricity from intermittent renewable energy sources can be converted and stored in form of hydrogen through water electrolysis, which enable the boosting of the utilization ratio of surplus electricity and simultaneously achieve the hydrogen production in a real low-carbon process. The electrolysis approach to produce H_2 from water has been long targeted as a promising method[10, 11] among the variety of H_2 generation technologies, such as natural gas reforming[12], electrolysis of water[11], and microbial biomass conversion[13], because of the environmentally benign process without CO_2 emissions as well as the high H_2 purity (>99.5%).

The overall hydrogen energy system in an integrated or hybridized fashion is illustrated in **Figure 1.3**, which shows the vision of Hydrogen at Scale initiative[14] by the U.S. Department of Energy.

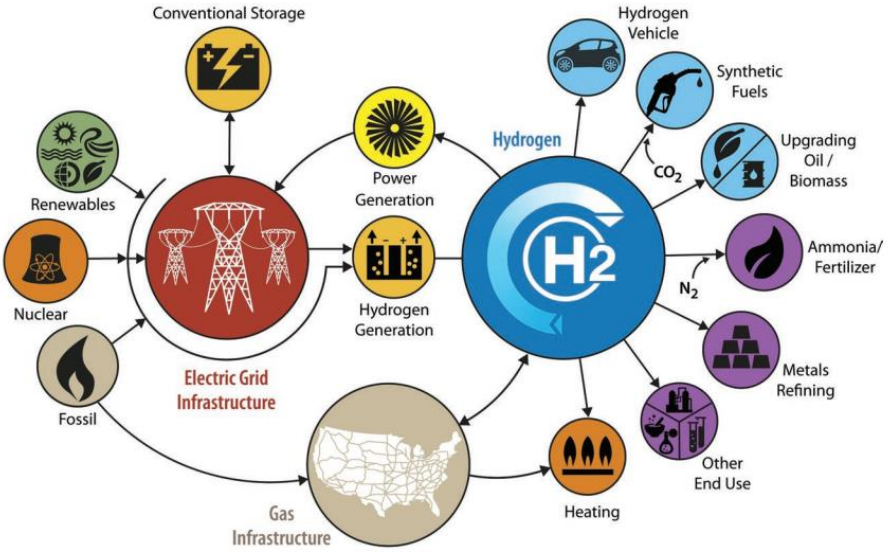

Figure 1.3[1] The schematic of the Hydrogen at Scale energy system. Copyright 2019 John Wiley and Sons.

Water can be decomposed into hydrogen and oxygen gases ($2H_2O \rightarrow 2H_2 + O_2$) by applying a cell voltage to two electrodes immersed in an electrolyte[10]. An energy input of 286 kJ mol^{-1} is required to drive the water electrolysis process at ambient conditions[15]. The archetypal water electrolysis cell is shown in **Figure 1.4**. The reaction occurs on the hydrogen generated cathodic side is called hydrogen evolution reaction (HER); and the oxygen evolution reaction (OER) occurs on the anodic side to generate oxygen gases (**Table 1.1**).

Table 1.1 The equations of HER and OER processes in acidic and alkaline electrolytes.

	Acidic electrolyte	**Alkaline electrolyte**
HER	$2H^+(aq) + 2e^- \rightarrow H_2(g)$	$4H_2O(l) + 4e^- \rightarrow 2H_2(g) + 4OH^-(aq)$
OER	$2H_2O(l) \rightarrow O_2(g) + 4H^+(aq) + 4e^-$	$4OH^- \rightarrow O_2(g) + 2H_2O(l) + 4e^-$

Theoretically, a reversible electrolysis cell voltage of 1.23 V is necessary to split water. In practice, a voltage larger than 1.23 V is usually required to drive the water electrolysis due to the electrode polarization and electrolyte concentration polarization[16]. The difference between the practical voltage and the theoretical voltage is called overpotential, which is usually given the symbol η. The "current density" represents the charge flow per unit area of the electrode. Generally, the larger current density from the water electrolysis device, the higher overpotential is needed to be applied between the two electrodes.

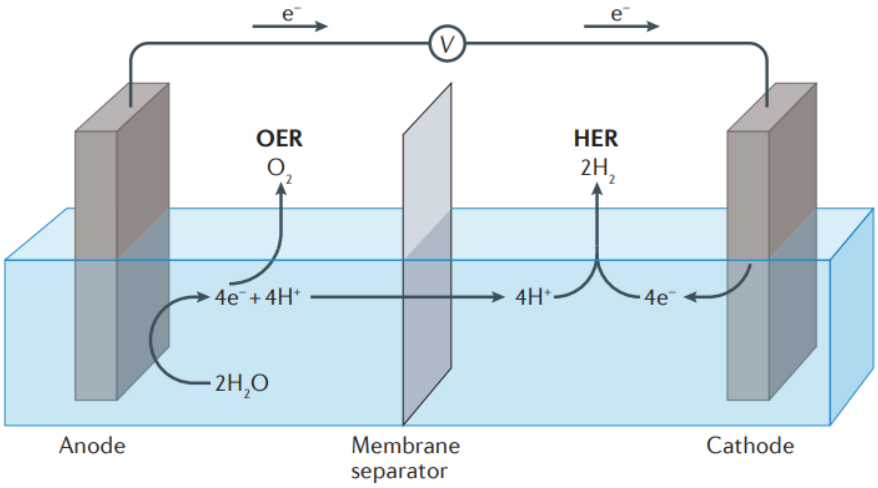

Figure 1.4[15] The typical water electrolysis cell under acidic environments. Copyright 2017 Springer Nature.

The whole HER process includes two steps[17], which are illustrated in **Figure 1.5** and **Table 1.2**. (1) Volmer step (black arrow in **Figure 1.5**): a proton diffuses to an empty active site on catalyst surface, and then couples with an electron that transferred to the site to form a hydrogen atom adsorbed on the catalyst. (2) The subsequent process has two different types of pathways: Tafel step (pink arrow in **Figure 1.5**) and Heyrovsky step (blue arrow in **Figure 1.5**). In the former case, two adsorbed hydrogen atoms combine and generate a desorbed hydrogen molecule. In the latter case, a proton couples with an adsorbed hydrogen atom and then form a hydrogen molecule. The proton sources are hydronium cations (H_3O^+) in acidic electrolytes, while they are water molecules in alkaline electrolytes. It means an extra step of water decomposition is required to generate protons for subsequent HER processes in alkaline electrolytes.

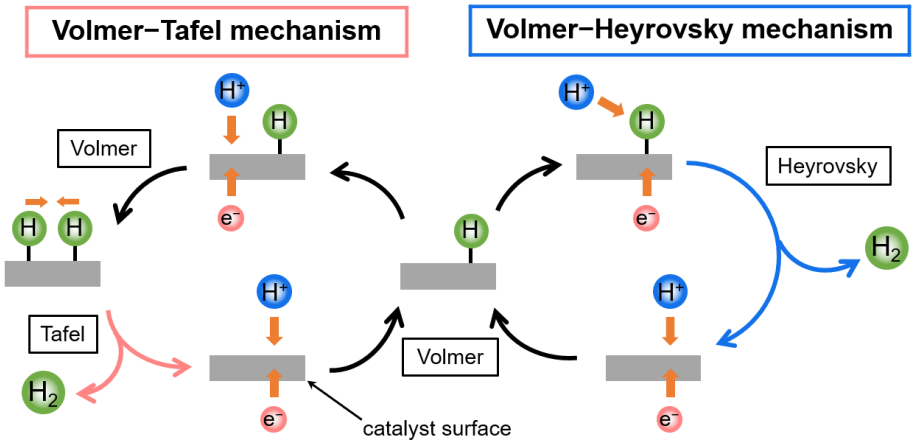

Figure 1.5[17] The schematic of HER mechanism in acidic electrolytes. Copyright 2014 The Royal Society of Chemistry.

Table 1.2 Summary of HER mechanism in acidic and alkaline electrolytes.

	HER in acid	**HER in alkali**
Volmer step	$H^+ + M + e^- \rightarrow M{-}H^*$	$H_2O + M + e^- \rightarrow M{-}H^* + OH^-$
Heyrovsky step	$M{-}H^* + H^+ + e^- \rightarrow M + H_2$	$M{-}H^* + H_2O + e^- \rightarrow M + OH^- + H_2$
Tafel step	$2M{-}H^* \rightarrow 2M + H_2$	$2M{-}H^* \rightarrow 2M + H_2$

Note: M and H* represent the metal catalyst surface and the adsorbed H atom on an active site, respectively.

1.1.3 Water electrolyzer

Proton exchange membrane (PEM) electrolyzers have attracted considerable attentions since this concept was firstly stated by Russell et al at 1973[18], and this technology is believed to be the promising type of next-generation electrolyzers to achieve large-scale hydrogen productions[11, 19]. Compared with the commercial alkaline electrolyzers, the PEM electrolyzers can achieve higher hydrogen gas purity (>99.99 vol.%)[11], larger current density up to 5000[1] mA cm^{-2}, higher voltage efficiency of 70−90%[20], faster dynamic response, and higher discharge hydrogen pressure of 30−76 bar[19], which are attributed to a thin solid perfluorosulfonic acid (usually known as Nafion^{TM}) membrane as the electrolyte. The characteristic comparison of alkaline electrolyzers and PEM electrolyzers is shown in **Table 1.3**. The configuration of these two types of water electrolyzers is illustrated in **Figure 1.6**[11].

Generally, catalysts are required to accelerate the sluggish HER and OER processes and reduce the overpotentials in both the cathode and the anode of water electrolyzers. Due to the internal corrosive low pH condition (pH 0.5~2)[11, 21], the suitable HER and OER catalysts are limited to acid-stable Pt group metals (e.g., Pt metal as the HER catalyst[22], IrO_2 and RuO_2 as OER catalysts[23, 24]). However, the high cost of such noble

metals-based catalysts and the scarcity impede the widespread applications of PEM water electrolyzers. Therefore, the development of earth-abundant metals catalysts to replace the Pt group catalysts is crucial to achieve a cost-efficient and sustainable hydrogen energy system.

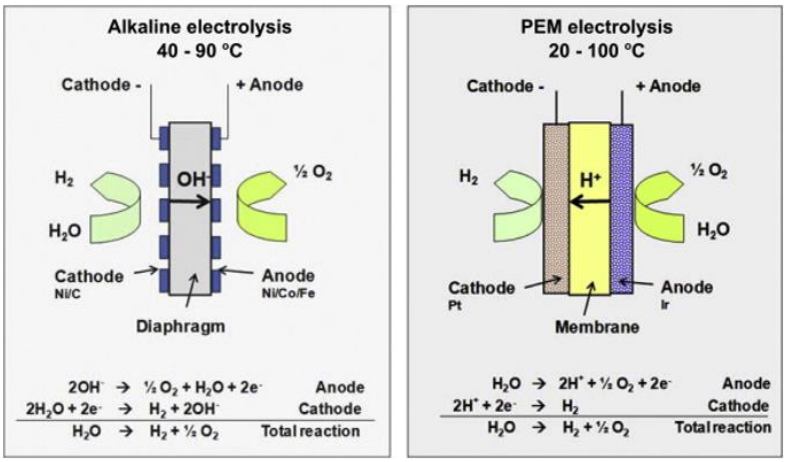

Figure 1.6 The schematic of the configuration of (a) alkaline electrolyzer and (b) PEM electrolyzer. Copyright 2013 Elsevier Inc.

Table 1.3 The characteristic comparison of alkaline electrolyzers and PEM electrolyzers[1].

	Alkaline electrolyzer	**PEM electrolyzer**
Technology status	Mature (stacks in MW range)	Mature for small scale (stacks below MW range)
Discharge H_2 pressure (bar)	atm.−30	30−76
Current density (mA cm^{-2})	250−450	1000−5000
Voltage efficiency (%)	76−82	70−90
System response	Slow (liquid electrolyte)	Fast (solid electrolyte)
Electrolyte	KOH solution	Nafion film

1.1.4 3D porous NiMo alloy: an efficient and earth-abundant HER electrocatalysts

One of the challenges for PEM electrolyzer is to overcome the catalyst degradation due to the internal acidic environments in cathode sides. Currently, Pt are is often employed as the cathode catalysts in PEM electrolyzers to accelerate the sluggish HER process, because of the high electrocatalytic activity and the outstanding chemical stability under harsh acidic environments. However, the scarcity and high cost of noble metal catalysts are the drawback for popular uses of PEM electrolyzers. Given such limiting factor for the use of the noble metal catalysts, developing cost-efficient and acid-stable noble metal-free catalysts

which possesses the HER activity comparable with Pt as well as the tolerance against its use under acidic conditions becomes extremely important.

Over the decades, numerous types of electrode materials have been developed to explore the replacement of noble metal catalysts by earth-abundant catalysts for the electrochemical HER process, including non-noble-metal alloys/oxides (NiMo, NiCo, FeCo)[25, 26, 27], metallic nitrides (WN, MoN)[28, 29], transition metal dichalcogenides MX_2 (M = Mo, W, Re, Fe, Co, Ni; X = S, Se)[30, 31, 32, 33, 34], metallic phosphides (NiP, CoP, NiMoP)[35, 36, 37], and metal-free carbon materials (C_3N_4, doped-graphene)[38, 39, 40, 41]. Among the various electrocatalysts, transition metal-based composites have been considered as desirable catalysts due to their remarkable HER activity, which is similar to that of Pt-group materials, and is explained by the particular d-band electronic structure[28, 42, 43, 44].

NiMo alloy, a typical transition metal alloy, exhibits Pt-comparable HER activities, such as the near-zero onset potential, the very low Tafel slope value, and the small electrical impedance. For example, Thomas F. Jaramillo *et al*[37, 45] reported that the electrochemical deposited NiMo alloy exhibited a lower overpotential to reach a current density of 10 mA cm^{-2} (η_{10}) than that of the Pt metal in both acidic and alkaline electrolytes (**Figure 1.7**). Based on the DFT calculations, Xinliang Feng *et al*[46] found that the NiMo alloy contributes to reduce the energy barrier of Volmer step and Mo atoms exhibits an excellent hydrogen adsorption property. Additionally, the Ni atoms are considered as the preferable sites for water molecules decomposition to generate protons in alkaline electrolytes[43].

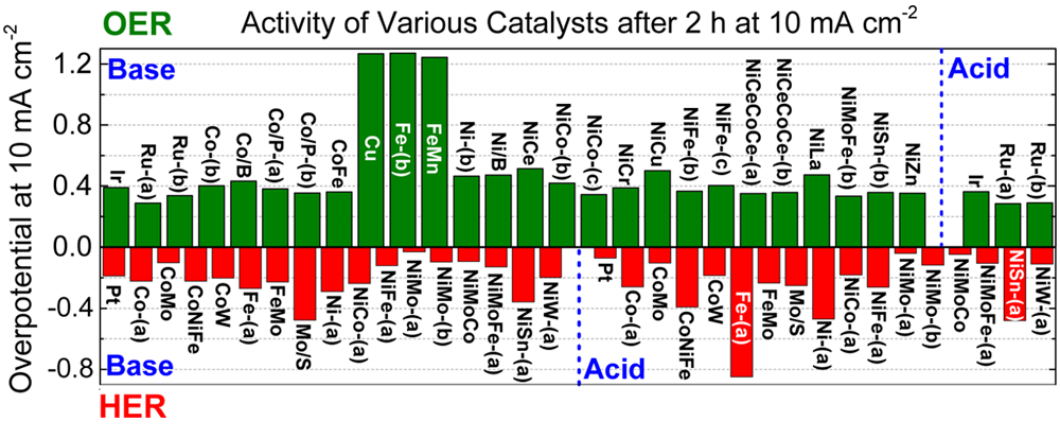

Figure 1.7 Comparison of HER and OER activities of various materials. Copyright 2015 American Chemical Society.

Porous metals are important materials for energy engineering fields because of outstanding conductivity, bi-continuous open porous structures with tunable porosity, large surface area, excellent catalytic activities and high mechanical strength[47, 48]. Recently, the study of porous non-noble metals has been focused as electrodes and catalysts such as supercapacitors[49], Li−O_2 batteries[50], fuel cells[51] and water electrolysis[52], showing great potentials as noble metal-free electrodes. The fabrication process of porous

metals employs a dealloying method in which the solid solution alloy of noble metal and non-noble metal is electrochemically corroded in acidic electrolytes[48]. However, in this method, the alloy combinations in the dealloying method is very limited and the non-noble metal of Ni, Fe and Cu is usually the one to be removed from the alloy, forming noble metal-based porous structures. Therefore, the desirable design of non-noble metal has been explored to expand their applications.

Porous non-noble metals have been synthesized by bottom-up approaches such as nanoparticle-sintering[53, 54] and reduction of metal oxides[46]. In particular, the reduction of metal oxide is a powerful method to prepare nanoporous non-noble metal. One of the most attractive porous metals is NiMo alloy which is known as one of the best performance hydrogen evolution electrode catalyst for cost-effective and highly efficient hydrogen production from water electrolysis[45]. Very recently, different kinds of NiMo alloy porous morphologies were investigated such as HER catalysts including Ni_4Mo[55], NiMo nanopowder[56], NiMo nanowire[57]. Indeed, the Ni foam supported Ni_4Mo nanoparticles, and the 3D NiMo nanowires significantly improved their HER activities. This means the nanosized morphological structure and monolithic 3D electrode catalysts contribute to high reaction kinetics and multiply diffusion pathways for generated gases. Therefore, NiMo alloy with open porous 3D structure can be a central electrode catalyst for the electrochemical water splitting.

1.1.5 Graphene encapsulation method

Although the outstanding HER activity makes NiMo alloy a promising alternative to Pt-based catalysts, the severe corrosion in acidic electrolytes[58] becomes the main obstacle for its potential large-scale applications in next-generation PEM water electrolyzers. Some endeavors have been made to overcome the disadvantage of corrosion. For instance, the sulfide, nitride, and phosphide of NiMo alloy were synthesized[36, 59, 60], which shows improved corrosion-resistant properties in acidic electrolytes. However, the corresponding HER activities exhibited an undesired declining trend in comparison to the bare NiMo alloy. Therefore, it becomes crucial to develop acid-stable and high-performance NiMo alloy-based catalysts.

Recently, an emerging encapsulation method that coats chemically stable graphene layers on the surface of non-noble and acid-soluble metals shows potential for achieving corrosion-resistant properties without undesired degradation in acidic environments[58, 61]. For example, Birbilis *et al*[61] coated graphene layers on Ni and Cu metal surfaces by a chemical vapor deposition (CVD) method to experimentally investigate the metal corrosion in 0.1 M NaCl electrolyte. They found that the coated graphene layers can serve as the protection barriers to the electrochemical corrosion of Ni and Cu metals in aqueous media. Burstein *et al*[58] synthesized graphene covered Ni metal particles by a magnetron sputtering method and investigated the passive nature of the as-synthesized materials in hot sulphuric acid (H_2SO_4). The experimental results exhibited that the graphene covered Ni particles had an excellent catalytic activity for hydrogen oxidation reaction and an improved stability even at the working temperature of 70 °C. It shows a promising for the applications as anode materials in acidic fuel cells. The schematic of various syntheses

methods of graphene-encapsulated metal/alloy materials is illustrated in **Figure 1.8**.

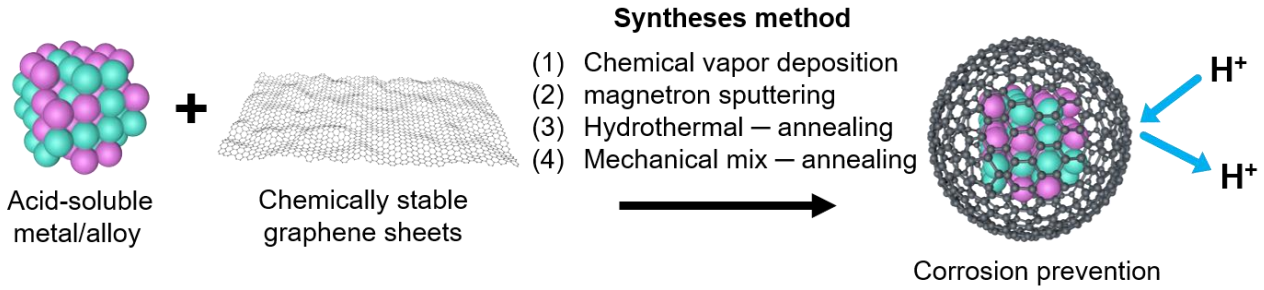

Figure 1.8 The schematic of various syntheses methods of graphene-encapsulated metal/alloy materials.

Graphene is a monolayer of carbon atoms in the form of honeycomb lattices, which was firstly mechanically exfoliated, isolated and characterized in 2004 by Andre Geim and Konstantin Novoselov at the University of Manchester[62]. One carbon atom in graphene lattice consists of three sp^2 hybrid orbits and one unhybridized p orbit. The p orbits overlap and hybridize together covalently to generate π band[63]. The high-mobile electrons in π band result in a delocalized electron cloud above and below each hexagonal carbon ring[63, 64]. The electron density distribution of graphene is exhibited in **Figure 1.9**. The dense electron cloud contributes to the impermeability of the defect-free graphene lattice for most of ions and all gases[65, 66] under the ambient conditions and without applied voltage. Therefore, graphene is an emerging material as the protective layer for acid-soluble catalysts under harsh environments.

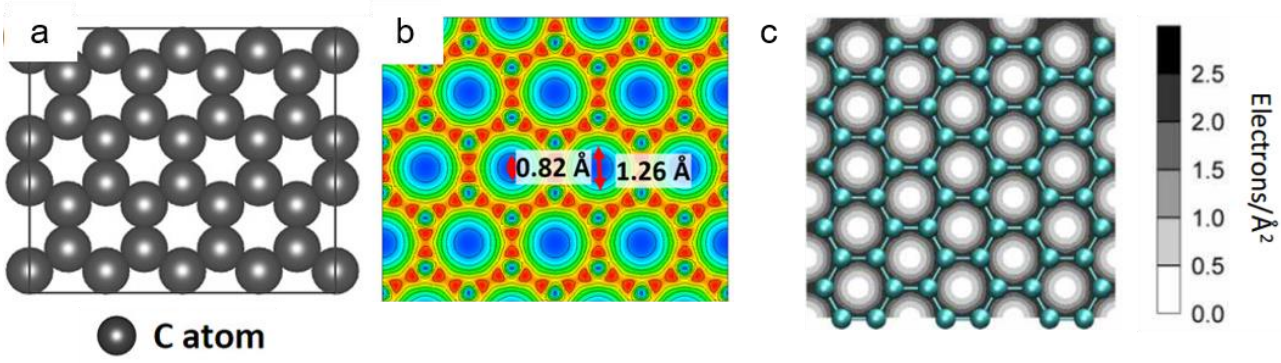

Figure 1.9 The geometries and electron density distribution diagram of monolayer graphene lattice. (a) The schematic of graphene lattice and (b) corresponding electron distribution diagram reported by Zhao *et al*[64]. The contour line in the charge density plots represents 0.05 e/Bohr^3. (c) The electron distribution of graphene lattice reported by Geim *et al*[67]. Copyright 2017 American Chemical Society & 2014 Springer Nature.

Currently, the studies of graphene-encapsulated HER catalysts mainly limit to three aspects. (1) The substrate material modification: numerous types of materials were developed as the substrates to support graphene layers, including CoNi alloy[68], NiCu alloy[69], molybdenum carbide (MoC_x)[70], FeCo alloy[71], and Ni

metal[72]. (2) The substrate structure engineering: encapsulated catalysts with various structures were synthesized, such as nanoparticles[68], nanocubes[73], nanowires[74]. (3) The chemical doping in graphene layers: encapsulating graphene layers were doped by different chemical elements to modify the electronic properties and HER activities. For example, doped encapsulating graphene layers include single doping by Nitrogen (N)[27, 68, 70] elements, co-doping by N and phosphorous (P)[75] or N and boron (B)[76, 77].

However, the fundamental understanding and HER mechanism of graphene-encapsulated catalysts have not been systematically studied so far. Especially, the effect of number of encapsulating graphene layers on HER performances, including catalytic activity and chemical stability, is not clear. Moreover, very limited studies focus on the influence of metal/alloy substrates towards encapsulating graphene layers, which is a crucial parameter to understand the individual contributions of graphene layers and encapsulated substrates to overall HER activities. In addition, there is still not a widely accepted HER mechanism of graphene-encapsulated catalysts in acidic electrolytes. More attentions are needed to be paid to the identification of catalytic sites of HER processes. A deep understanding of the fundaments and mechanisms, including the effect of graphene layer number on HER performances, the effect of metal/alloy substrate on graphene layers, the identification of catalytic sites, and the HER mechanism, is of great importance in the design and synthesis for state-of-the-art graphene-encapsulated HER catalysts applied in acidic electrolytes.

1.1.6 Proton penetration through graphene layers

The electrolysis approach to produce H_2 from water has been long targeted as a promising method[10, 11] among the variety of H_2 generation technologies, such as natural gas reforming[12], electrolysis of water[11], and microbial biomass conversion[13], because of the environmentally benign process without CO_2 emissions as well as the high H_2 purity (>99.5%). PEM water electrolysis is expected to be a next-generation technology for H_2 production, which has been reported to be more efficient than the alkaline water electrolysis, because of high H_2 gas purity (>99.99 vol.%), fast dynamic response, large current density (~5 A cm^{-2}), high discharge H_2 pressure (30−76 bar), downsizing of cell and no alkaline waste electrolyte[1, 11]. Here, one of the challenges for PEM electrolyzer is to overcome the catalyst degradation due to the internal acidic environments in cathode sides. Currently, Pt are is often employed as the cathode catalysts in PEM electrolyzers to accelerate the sluggish HER process, because of the high electrocatalytic activity and the outstanding chemical stability under harsh acidic environments. However, the scarcity and high cost of noble metal catalysts are the drawback for popular uses of PEM electrolyzers. Given such limiting factor for the use of the noble metal catalysts, developing cost-efficient and acid-stable noble metal-free catalysts which possesses the HER activity comparable with Pt as well as the tolerance against its use under acidic conditions becomes extremely important.

The main source for the catalytic degradation of HER catalysts under acidic media is the corrosion. To prevent corrosion of the catalysts, one can passivate or coat the catalyst surface. However, simply coating the materials leads to covering the catalytically active site on the surface of the catalysts, lowing the catalytic

activity. As such, balancing between corrosion resistance and catalytic activity is challenging. A smart solution is the encapsulation of the catalysts employs chemically stable graphene layers on the surface of non-noble metals[58, 78, 79, 80]. For example, the graphene-encapsulated Ni, Fe and CoNi alloy nanoparticles were synthesized as HER catalysts used in acidic electrolytes[68, 81, 82]. However, the fundamental HER mechanism and the reason of unavoidable degradation of catalytic activity have not been well studied for graphene-encapsulated catalysts so far.

Based on previous reports, the layer number of graphene sheets plays a significant role in not only long-term catalyst lifetime but also catalytic performances of encapsulated non-noble-metal catalysts in acidic electrolyte[68, 79]. For instance, encapsulation by thin graphene layers, such as monolayer or bilayer graphene, cannot effectively prevent the dissolution of encapsulated non-noble-metal catalysts in acidic electrolytes, while encapsulation by thick graphene layers results in extremely high chemical stability but reduced the catalytic activities due to the blocking of catalytically active sites on the catalyst surface. Accordingly, we hypothesize that the encapsulating graphene layers have two mechanisms in acidic electrolytes on viewpoints of sieving effect: (1) the penetration of limited protons through graphene layers to the encapsulated non-noble metal surface; (2) the prevention of exposure of the non-metal surface from excess number of protons by the thick encapsulating graphene sheets. Thus, the balance between corrosion resistance and catalytic activity could be achieved by understanding the behaviour of proton/hydrogen molecules in the interface of graphene/non-noble metal surface.

As reported by Geim *et al*[67, 83] in 2014 and 2016, the proton could penetrate through the electron cloud of defect-free monolayer graphene under applied voltage. From their experimental results, the monolayer graphene has a high permeable property to thermal protons at ambient conditions. The measured proton areal conductivity is around 5 mS cm^{-2} for monolayer graphene at room temperature, and this value can dramatically increase to 60 mS cm^{-2} at 60 °C, which exhibited Arrhenius-type behaviour as a function of temperature T, $\exp(-E/k \cdot T)$. The energy barrier to proton transport through graphene was calculated as 1.25−1.40 eV by *ab initio* molecular dynamics (AIMD) simulations and the climbing-image nudged elastic band (CI-NEB) method. These values are similar with the calculated results of 1.17−2.21 eV by Liu *et al*[84] and Kaxiras *et al*[85]. From the experimental results and theoretical calculations, the subatomic selectivity of graphene has been confirmed, which means, in another word, graphene is permeable to thermal protons and impermeable to larger, atomic species[65, 66, 86, 87].

This founding of graphene permeability through graphene inspires the study of HER mechanism of graphene-encapsulated catalysts. In previously published reports[27, 68, 88], some unexpected degradations of graphene-encapsulated non-noble-metal catalysts were observed in acidic electrolytes, especially during the long-term galvanostatic or potentiostatic measurements. The graphene penetration could be a sound reason for this situation. The proton could firstly penetrate through encapsulating graphene layers, and then dissolved the underlying acid-soluble metals/alloys, which would probably decrease the HER activities. In

order to verify the assumption proposed above, a systematical investigation of graphene penetration behaviour through graphene layers is necessary to clarify the long-standing unclear HER mechanism of graphene-encapsulated catalysts.

Among the approaches employed to fabricate catalysts, encapsulation of non-noble-metal nanoparticles using chemically stable graphene layers is particularly promising. Encapsulation by thick graphene[27, 89, 90] provides high chemical stability but often reduces the catalytic activity significantly. In contrast, single-layer encapsulation affords high-performance catalysts, but with short lifetimes[68]. To achieve excellent balance between HER performance and catalyst lifetime, holey graphene as a partial protection were used to encapsulate bulk porous NiMo alloys to minimize the surface area for desirable chemical reactions in the holes and to protect NiMo dissolution in acidic electrolytes by avoiding corrosion with the holey graphene covering[80]; this combination achieves better long-term durability in acidic electrolytes than pristine NiMo alloys without graphene covering. However, undesired dissolution arising from acid penetration through the holes of the graphene persisted. Therefore, on the basis of the theory that thin encapsulating graphene significantly enhance HER performance[68], a critical additional step for the practical application of this technique is optimizing the layer number of encapsulating graphene to balance the HER activity and catalyst lifetime. This requires precise control of the graphene layer present on the non-noble-metal catalyst surfaces. Thus, optimizing the graphene encapsulation method and understanding the effect of layer number of graphene on HER activity are required.

1.1.7 DFT calculation: a powerful tool to evaluate HER catalysts

DFT calculations play an important role in the evaluation and high-throughput screening of the electrochemical HER catalysts[22, 91], which has been confirmed as a powerful strategy to identify a new efficient HER catalyst among numerous potential materials.

The adsorbed H atom on the catalyst surface is an intermediate for HER processes that follow either the Volmer−Heyrovsky or the Volmer−Tafel mechanism (**Figure 1.10a**). This means that the Gibbs free energy of H adsorption and desorption (ΔG_{H^*}) is a key parameter to determine the rate of the overall HER process. Based on the Sabatier principle, the high-activity catalyst should have an intermediate bond strength between atoms or molecules and catalyst surface[92]. If the bond strength is too strong (i.e., the ΔG_{H^*} value is too low), the H desorption process is difficult to occur and costs large energy, thus the Heyrovsky/Tafel step becomes the rate-limiting step (**Figure 1.10b**). If the bond strength is too weak (i.e., the ΔG_{H^*} value is too high), the large energy is needed to activate the reactants and the Volmer step limits the overall reaction rate. Thus, a neither too low nor too high ΔG_{H^*} value corresponds to the optimal HER activity. As the theory of Sabatier principle, a volcano-type relationship between the HER activity and the ΔG_{H^*} value is illustrated in **Figure 1.10c**.

Plotting experimentally measured HER exchange current densities of various catalyst materials

against the ΔG_{H^*} values calculated by DFT, a volcano relationship emerges (**Figure 1.11**)[22]. From the volcano plot, the experimentally high-performance HER catalysts, such as Pt, present in the volcano peak with a ΔG_{H^*} value around zero, which represents an intermediate bond strength between H atoms and catalyst surfaces. These results are in an agreement with the Sabatier principle. Therefore, it was confirmed that the ΔG_{H^*} value is a reasonable descriptor of the HER activity for various catalyst materials.

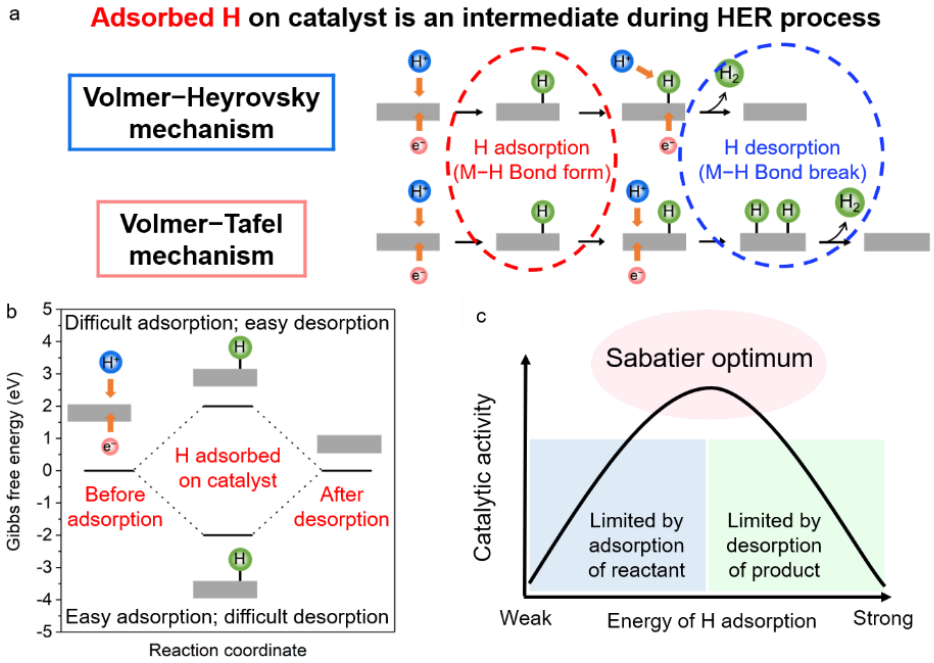

Figure 1.10 (a) Schematic of H adsorption and desorption during HER processes. (b) The energy diagram of H adsorption and desorption processes. (c) Schematic representation of the qualitative Sabatier principle.

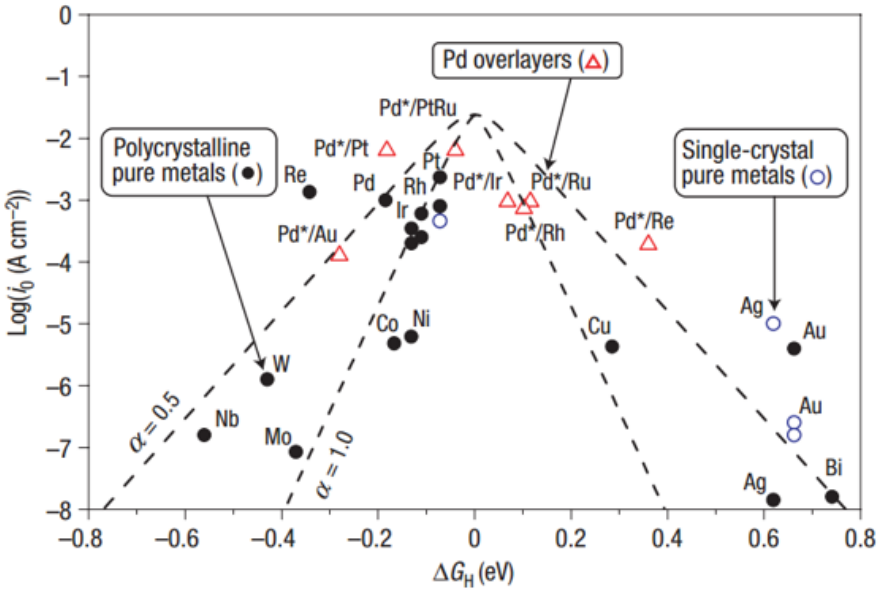

Figure 1.11 Volcano plot for the HER of various catalyst materials. The two curved lines correspond to the transfer coefficients (α) of 0.5 and 1.0, respectively. Copyright 2006 Springer Nature.

1.2 Introduction of important theories and methods

1.2.1 Butler−Volmer Equation

The Butler−Volmer equation is one of the most important and fundamental relationship to evaluate the electrode kinetics of catalytic reactions[16, 93]. In a typical Butler−Volmer equation (equation 1.1), it exhibits the relation between the electric current density *j* and the potential difference at the electrode interface (i.e., the surface overpotential η_s; $\eta_s = E - E^0$, E and E^0 are the electrode potential and the equilibrium electrode potential), which is expressed as

$$j = j^0 \exp\left(\frac{-\alpha z F}{RT}\eta_s\right) - j^0 \exp\left(\frac{(1-\alpha) z F}{RT}\eta_s\right) \quad (1.1)$$

where j^0 is the exchange current density; α is the charge transfer coefficient; *z*, *F*, *R*, and *T* represent the number of transferred electrons, the Faraday constant, the gas constant, and the temperature, respectively.

The derivation of the equation (1.1) shows as below.

According to the general transition state theory in electric kinetics, an activation energy is needed to be overcome to drive a reaction. As shown in **Figure 1.12**, the height of the peak is identified as the transition state or activated complex. The standard Gibbs free energy change between the reactants and the transition state is $\Delta G_f^{\ddagger}$, while the change between the products and the transition state is $\Delta G_b^{\ddagger}$.

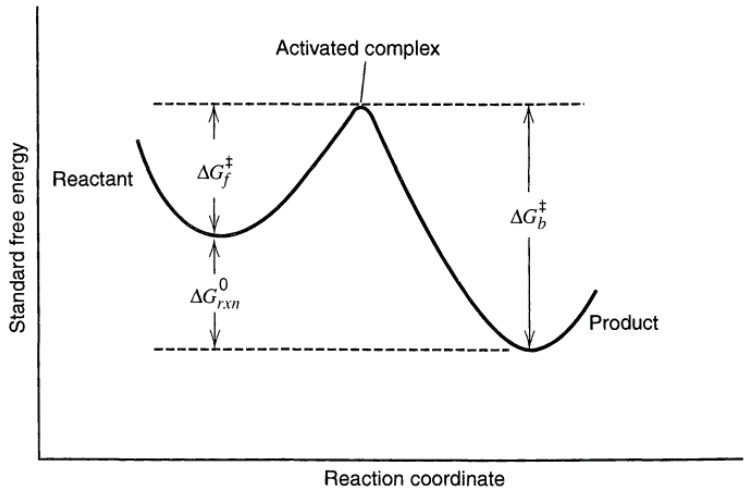

Figure 1.12 The change of free energy values during a reaction. The activated complex (or transition state) represents the maximum free energy value. Copyright 1980 John Wiley and Sons.

Here, a simplest one-step, one-electron transfer reaction ($n = 1$) is used as the example to derivate the Butler−Volmer equation.

$$O + e \Leftrightarrow R \tag{1.2}$$

The standard free energy is plotted with respect to the reaction coordinate (**Figure 1.13**). The curves represent the reaction path from reactant to products. The electrode potential in the upper curve on the O + e side is $E^{0'}$. The cathodic and anodic activation energies are $\Delta G_{0c}^{\ddagger}$ and $\Delta G_{0a}^{\ddagger}$, respectively. Thus, the energy barriers for reduction, $\Delta G_{c}^{\ddagger}$, and oxidation, $\Delta G_{a}^{\ddagger}$, are calculated as,

$$\Delta G_{c}^{\ddagger} = \Delta G_{0c}^{\ddagger} + \alpha F\left(E - E^{0'}\right) \tag{1.3}$$

$$\Delta G_{a}^{\ddagger} = \Delta G_{0a}^{\ddagger} - (1-\alpha) F\left(E - E^{0'}\right) \tag{1.4}$$

The reaction rate constant k_c and k_a in an Arrhenius form can be presented as,

$$k_c = A_c \exp\left(\frac{-\Delta G_{c}^{\ddagger}}{RT}\right) \tag{1.5}$$

$$k_a = A_a \exp\left(\frac{-\Delta G_{a}^{\ddagger}}{RT}\right) \tag{1.6}$$

Insert the activation energies (1.3) and (1.4) into equation (1.5) and (1.6), gives

$$k_c = A_c \exp\left(\frac{-\Delta G_{0c}^{\ddagger}}{RT}\right) \exp\left[\frac{-\alpha F\left(E-E^{0'}\right)}{RT}\right] = k^0 \exp\left[-\frac{\alpha F\left(E-E^{0'}\right)}{RT}\right] \tag{1.7}$$

$$k_a = A_a \exp\left(\frac{-\Delta G_{0a}^{\ddagger}}{RT}\right) \exp\left[\frac{(1-a) F\left(E-E^{0'}\right)}{RT}\right] = k^0 \exp\left[\frac{(1-a) F\left(E-E^{0'}\right)}{RT}\right] \tag{1.8}$$

where k^0 is the standard rate constant; A is the frequency constant.

The reaction current represents the current–potential characteristic as,

$$j = j_c - j_a = FA[k_c C_O(0,t) - k_a C_R(0,t)] \tag{1.9}$$

where $C_O(0,t)$ is the concentration of species O at the electrode surface at time t; $C_R(0,t)$ is the concentration of species R at the electrode surface at time t.

Inset the k_c (1.7) and k_a (1.8) into the equation 1.9, gives

$$j = nFAk^0 \left\{ C_O(0,t) \exp\left[-\frac{\alpha F\left(E-E^{0'}\right)}{RT}\right] - C_R(0,t) \exp\left[\frac{(1-a) F\left(E-E^{0'}\right)}{RT}\right] \right\} \tag{1.10}$$

The exchange current density (reaction current under the equilibrium state) is,

$$j_0 = FAk^0 \left[C_O^{*(1-\alpha)} C_R^{*\alpha}\right] \tag{1.11}$$

where C_O^* is the bulk concentration of species O; C_R^* is the bulk concentration of species R.

The reaction current density (1.10) divided by the exchange current density (1.11), gives

$$\frac{j}{j_0} = \frac{C_{\mathrm{O}}(0,t)\exp\left[-\frac{\alpha F\left(E-E^{0'}\right)}{RT}\right]}{C_{\mathrm{O}}^{*(1-\alpha)}C_{\mathrm{R}}^{*\alpha}} - \frac{C_{\mathrm{R}}(0,t)\exp\left[\frac{(1-a)F\left(E-E^{0'}\right)}{RT}\right]}{C_{\mathrm{O}}^{*(1-\alpha)}C_{\mathrm{R}}^{*\alpha}} \tag{1.12}$$

If the solution/electrolyte is well stirred, then we can assume no mass-transfer effect. In this case, the $C(0,t) \approx C^*$, and then the (1.12) becomes,

$$j = j_{\mathrm{c}} - j_{\mathrm{a}} = j_0 \exp\left(\frac{-\alpha F}{RT}\eta\right) - j_0 \exp\left(\frac{(1-\alpha)F}{RT}\eta\right) \tag{1.13}$$

which is the well-known Butler−Volmer equation, exhibiting a relation between the reaction current and the electrode overpotential.

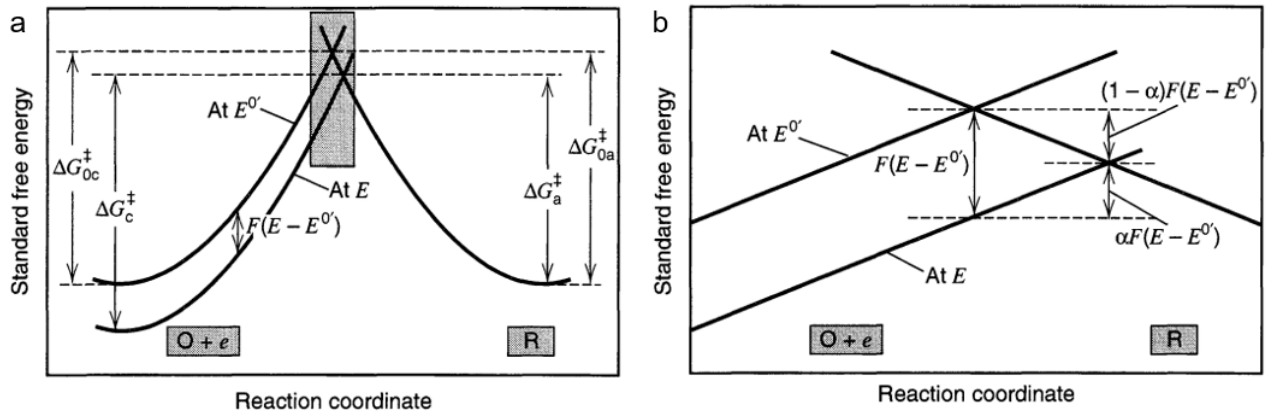

Figure 1.13 The plots of the potential changes during a reaction. (a) The potential change of the cathodic and anodic activation energies. (b) The zoom-in picture of the box area in (a). Copyright 1980 John Wiley and Sons.

1.2.2 Tafel plots

The Tafel equation, obtained by summarying large quantities of experimental data, reveals a quantitative relation between the rraction current and the electrode potential, which is of significance in electrochemical kinetics[16]. The Tafel plot is a diagram of logarithmic current density, $\log i$, vs. overpotential, η, (**Figure 1.14**), and the slope value is a powful tool to evaluate the reaction kinetics of HER catalysts[94].

Note that the characteristic of relation between current density and overpotential is logarithmic when the overpotential under a special region, which is usually considered as 15−300 mV vs. RHE[95]. When the electrode overpotential is less than 15 mV vs. RHE (i.e., a resistive and capacitive region), the relation is linear and it obeys Ohm's law. For a very small value *x*, the exponential e^x is approximated as *x* + 1. Thus, for a small overpotential value, the $e^{\eta} \approx \eta + 1$. The equation 1.13 can be expressed as,

$$j = -j_0 \frac{F}{RT}\eta \tag{1.14}$$

The relation of η to j is linear, and the ratio of η/j is called the *charge transfer resistance*, R_{ct},

$$R_{ct} = -\frac{RTj_0}{F} \tag{1.15}$$

When the electrode overpotential is large enough, the backward reaction becomes negligible. For instance, the eletrode is at large negative overpotentials, $\exp\left(\frac{-\alpha\eta F}{RT}\right) \gg \exp\left(\frac{(1-\alpha)\eta F}{RT}\right)$, and then the (1.13) becomes,

$$j = j_0 \exp\left(\frac{-\alpha F}{RT}\eta\right) \tag{1.16}$$

or

$$\eta = \frac{RT}{\alpha F}\ln j_0 - \frac{RT}{\alpha F}\ln j \tag{1.17}$$

Thus, the Tafel slope is $-\frac{2.303RT}{\alpha F}$. Since it is a one electron transferred reaction as the example, the Tafel slope value is 118 mV. If the overpotential is large than 118 mV (one-step, one-electron transfer reation case), the reaction current becomes *mass transfer limited*.

Under the Tafel region, the backward reaction can be regards as negligible, thus the (1.13) can be rewritten as,

$$j = j_c - j_a = j_c - 0 = j_0 \exp\left(\frac{-\alpha F}{RT}\eta\right) - 0 = j_0 \exp\left(\frac{-\alpha F}{RT}\eta\right) \tag{1.18}$$

or

$$\eta = \left(\frac{2.3RT}{\alpha F}\right)\log j_0 - \left(\frac{2.3RT}{\alpha F}\right)\log j = \mathrm{a} - \mathrm{b}\log j \tag{1.19}$$

which is termed as the Tafel equation. Abbreviated as $\eta = \mathrm{a} - \mathrm{b}\log j$.

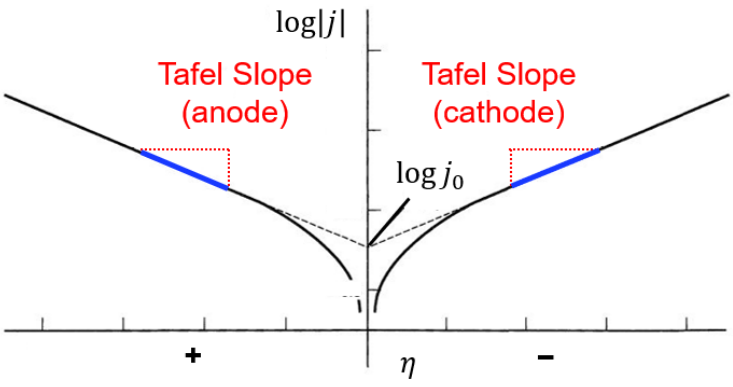

Figure 1.14 The typical Tafel plot. Copyright 1980 John Wiley and Sons.

1.2.3 HER Kinetics Mechanism Determined by Tafel Equation

The Tafel equation can be considered as a fundamental theory to understand the generalized kinetics of reactions with electron transfers. The Tafel slope can be derived from (1.19) as,

$$\mathrm{b} = \frac{2.3RT}{\alpha zF} \tag{1.20}$$

Tafel slope b usually used to characterize the catalytic performance of electrochemical catalysts, and also determine the rate-determining step (rds) of electrochemical reactions[96, 97]. From the equation (1.20), the value of Tafel slope b largely depends on the charge transfer coefficient α, which is a quantity that reflects the nature of the electron transfer in elementory reaction[98, 99]. The α value is generally considered as 0.5 or 0 for one-electron transfer or non-electron transfer reaction, respectively. For multi-electron transfer processes, the number of electron transferred in steps before the rds also contributes to the α value.

Next, I will use the HER process as an example to show the rds decided by Tafel slope b.

(1) If the Volmer step ($H^+ + M + e^- \rightarrow M{-}H^*$, **Table 1.2**) is the rds, the $\alpha = 0.5$ and $z = 1$ due to one-electron transfer process. Thus, the b can be calculated as

$$\mathrm{b} = \frac{2.3RT}{\alpha zF} = \frac{2.3\times 8.314\ \mathrm{J\ K^{-1}}\times 298\ \mathrm{K}}{0.5\times 1\times 96485\ \mathrm{J\ V^{-1}}} = 118\ \mathrm{mV} \approx 120\ \mathrm{mV} \tag{1.21}$$

(2) If the Heyrovsky step ($M{-}H^* + H^+ + e^- \rightarrow M + H_2$, **Table 1.2**) is the rds, the α should be corrected as $n + \alpha$ due to the contribution of the transferred electron in the process (i.e., a single Volmer step) before rds. The n is the number of electron transferred before rds. Here, $n = 1$.

$$\mathrm{b} = \frac{2.3RT}{(n+\alpha)zF} = \frac{2.3\times 8.314\ \mathrm{J\ K^{-1}}\times 298\ \mathrm{K}}{(1+0.5)\times 1\times 96485\ \mathrm{J\ V^{-1}}} = 39.4\ \mathrm{mV} \approx 40\ \mathrm{mV} \tag{1.22}$$

(3) If the Tafel step ($2M{-}H^* \rightarrow 2M + H_2$, **Table 1.2**) is the rds, the $n = 2$ due to the two Volmer steps occur before the Tafel step. The $z = 0$ and $\alpha = 0$ because of non-electron transfer. Thus,

$$\mathrm{b} = \frac{2.3RT}{(n+\alpha)zF} = \frac{2.3\times 8.314\ \mathrm{J\ K^{-1}}\times 298\ \mathrm{K}}{(2+0)\times 96485\ \mathrm{J\ V^{-1}}} = 29.5\ \mathrm{mV} \approx 30\ \mathrm{mV} \tag{1.23}$$

From the discussions above, the value of Tafel slope b is a predictive factor of the rds for HER processes. For example, if the Tafel slope b is calculated as 30 mV, which means that the rds is Tafel step for HER processes under the certain overpotential. Note that the measured Tafel slope may not perfectly follow the values in (1.21−1.23), which requires further interpretation of the reaction kinetics combined with other knowledges. Importantly, the Tafel slope also largely depends on the electrode overpotential, the catalyst surface roughness, and the solvent environment. A brief summary of the derivation of the Tafel slope values is exhibited in **Figure 1.15**.

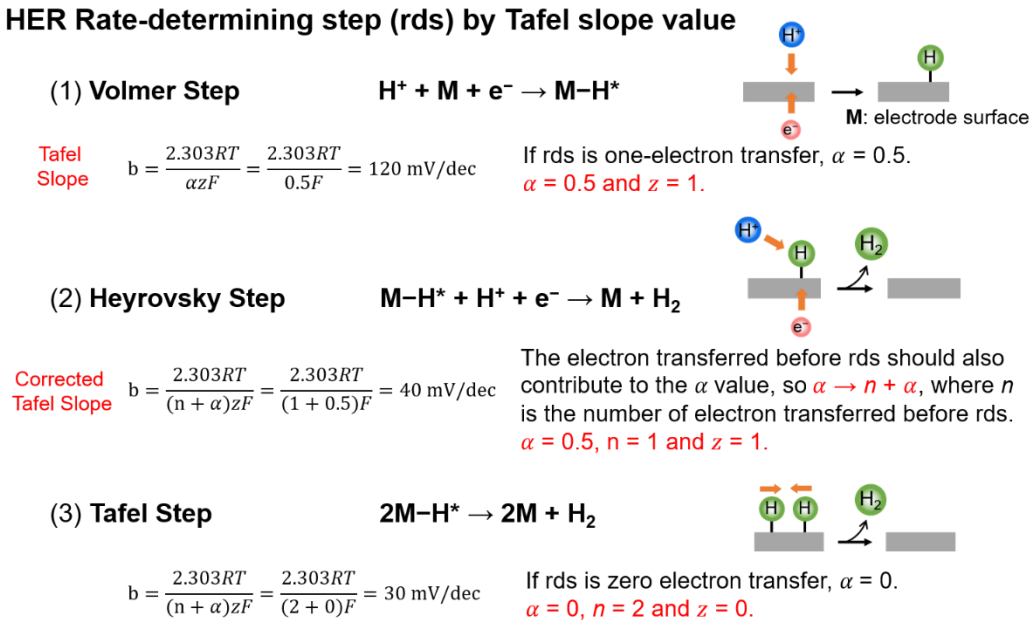

Figure 1.15 HER rate-determining step decided by Tafel slope value.

1.2.4 Three-electrode System & Cyclic Voltammetry

Generally, the three-electrode system is preferable to be used to study the interested reaction occurs in only one electrode, especially the iR_s drop is relatively large[16]. R_s is the electrolyte resistance. The three-electron system comprises working electrode (WE), counter electrode (CE), and reference electrode (RE). The WE act as the electron acceptor or donor to the reactants under a certain electrode potential in the electrolyte. The function of the CE is to provide a circuit with the WE. The materials of CE cannot affect the behaviour of working electrode. The RE, coupled with WE, is a nonpolarizable electrode that no current flows through. The set-up of a typical three-electrode system is illustrated in **Figure 1.16**.

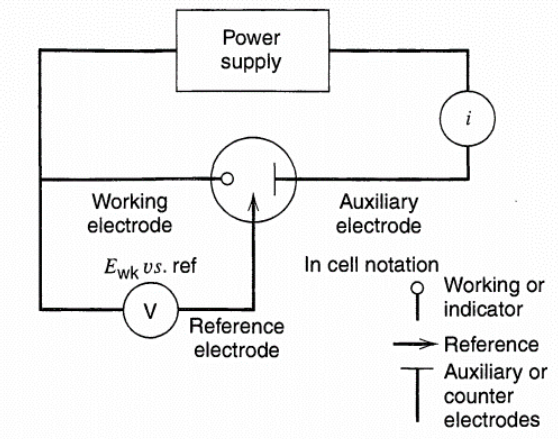

Figure 1.16 The set-up of a three-electrode system. Copyright 1980 John Wiley and Sons.

Cyclic voltammetry (CV) is an analytical technique to study electrochemical systems. The potential difference between the WE and the RE is scanned linearly in time from a start potential to an end potential, and then scan backwards again (**Figure 1.17a**). A forward scan plus a backward scan is called one cycle. The current at the working electrode is recorded and plotted against the electrode potential in a voltammogram. A typical HER polarization curve collected by CV method is shown in **Figure 1.17b**.

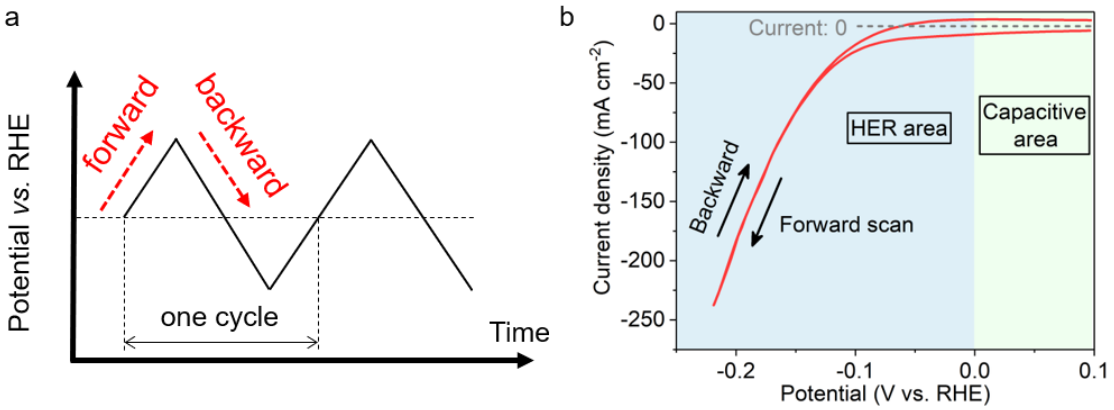

Figure 1.17 (a) Cyclic voltammetry potential waveform. (b) Typical CV curve for HER processes.

1.2.5 Electrochemical Impedance Spectroscopy

Electrochemical impedance is the response of an electrochemical system to an applied potential. The impedance is measured as a function of the frequency of the AC (alternating current) source[16, 100]. Generally, the impedance of an electrochemical system, defined as $Z(\omega)$, is the AC response of the system to an AC signal. The measured electrode impedance plotted against frequency is regarded as the electrochemical impedance spectroscopy (EIS). The $Z(\omega)$ can be presented in Cartesian coordinates as,

$$Z(\omega) = Z_{re} + iZ_{im} \tag{1.24}$$

where Z_{re} (or Z') is the real part of the impedance, while Z_{im} (or Z'') is the imaginary part.

Nyquist plot displays the measured impedance Z values at ranged frequencies ω, where each point represents the real Z_{re} and Z_{im} imaginary parts. **Figure 1.18** shows a typical Nyquist plot and the corresponding equivalent circuit. In the equivalent circuit, R_{s} represents the resistance relevant to electrolyte and two electrodes; R_{ct} represents the charge transfer resistance; C_{DL} represents the double layer capacitance; Z_{w} is the Warburg diffusion element.

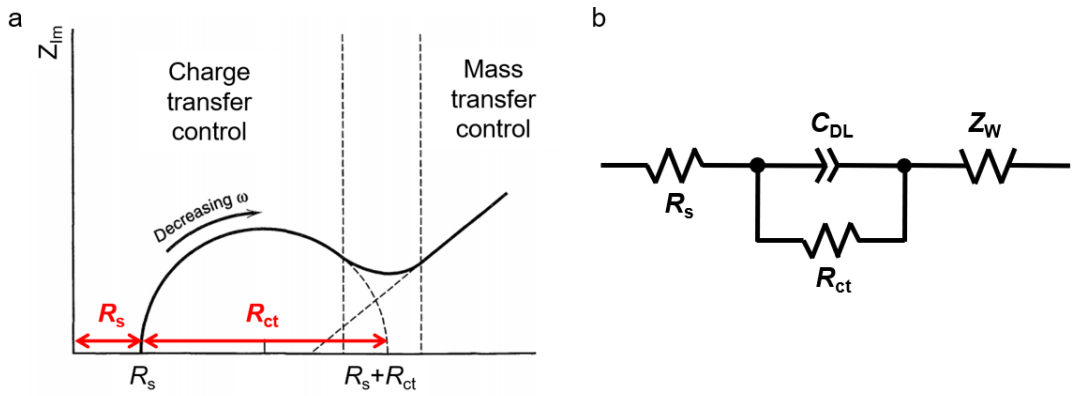

Figure 1.18 (a) Typical Nyquist plot and (b) corresponding equivalent circuit. Copyright 1980 John Wiley and Sons.

1.2.6 Graphene synthesis by chemical vapor deposition

The thermally induced CVD has emerged as a significant method to synthesize large-area and high-quality graphene sheets[101, 102] in comparison to other syntheses routes, including elimination Si from the single crystal SiC[103], mechanical exfoliation of highly ordered pyrolytic graphite[62, 104], wet-chemical approaches[105, 106]. Generally, the principle of CVD graphene growth can be described as following: the hydrocarbon gas precursors, methane, benzene, etc., flow into the high-temperature reaction region, where the precursors decompose into carbon (C) radicals on the metal surface, and subsequently form graphene layers on metals. Herein, the metal surface acts as the catalyst for the decomposition of the hydrocarbon molecules at high temperature. The flexible controlling of the number of graphene layer is another advantage of CVD approach, and the copper (Cu) and nickel (Ni) are the most common used substrate materials for graphene syntheses by CVD. For example, the monolayer is usually grown on the Cu metal surface[107], however, the few-layer graphene growth can be processed on the surface of Ni metals[102]. The mechanism and kinetics of CVD graphene growth on Ni and Cu metal substrates are totally different, which has been systematically studied by Prof. Ruoff's group using the isotopic labeling method[108]. Simply speaking, the graphene growth on Ni obeys a C segregation process, whereas the growth on Cu follows a C surface adsorption process. A brief comparison of these two approaches is exhibited in **Figure 1.19**.

The C segregation is a nonequilibrium process, which strongly depends on the speed of cooling down (**Figure 1.20**)[102]. Firstly, the Ni foils were placed in the chamber under the mixed atmosphere of hydrogen and inert gases. Secondly (C dissolution), the hydrocarbon gases as precursors were introduced into the chamber where the hydrocarbon molecules decompose into C atoms on the Ni surface, and then the C atoms dissolve and diffuse into the body of Ni foils. Note that the C concentration decreases exponentially from the metal surface to the body. Thirdly (C segregation), the C atoms segregate from the bulk metal body to the surface during cooling down. The cooling down speed is the key to the C segregation behaviour. Fast cooling rate (20 ºC/s or faster) leads to a quench effect in which the dissolved C atoms suddenly lose the

mobility. A middle cooling rate results in a finite amount of C atoms diffuse to the metal surface and form graphene layers. The very slow cooling rate gives enough time for the diffusion of the C atoms to the bulk metal again, which means segregated C atoms on surface are not enough to form large-area graphene regions.

Therefore, controlling the cooling rate during CVD processes is an efficient strategy to control the layer number of generated graphene sheets on metal surfaces.

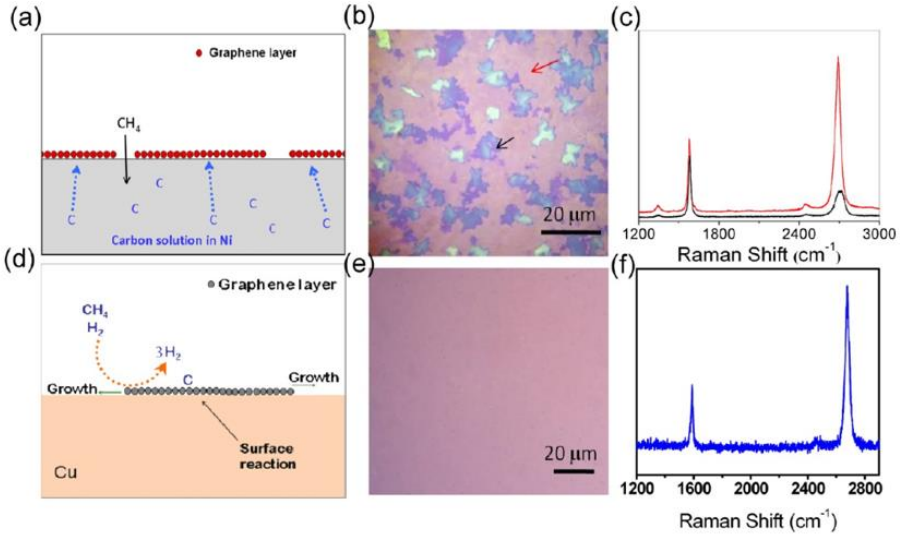

Figure 1.19[101] The schematic mechanism of graphene growth on (a) Ni and (d) Cu. The optical images of transferred graphene on SiO_2 substrates from (b) Ni and (e) Cu surfaces. The collected Raman spectra on (c) Ni and (f) Cu substrates. Copyright 2013 American Chemical Society.

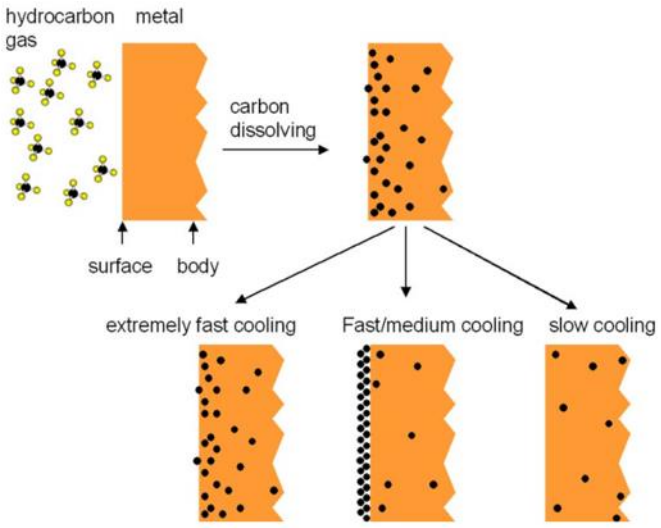

Figure 1.20 Illustration of carbon segregation at Ni metal surface. Copyright 2008 American Institute of Physics.

1.3 Research purposes & strategies

In chapter 2, the purpose is to introduce all experimental methods involved in this dissertation.

In chapter 3, the purpose is to synthesize an earth-abundant-metal HER catalyst through a simple and cost-efficient process. A high HER activity and an excellent stability are two crucial parameters to evaluate the potential catalyst. For this purpose, I chose a two-step method, including hydrothermal process and annealing process, to synthesize a novel 3D NiMo alloy with bicontinuous open porous structure.

In chapter 4, the purpose is to achieve the balance of corrosion resistance and catalytic activity of NiMo alloy under acidic media by graphene encapsulation. To reach this, I grew graphene to encapsulate NiMo alloy nanoparticles by CVD. Through tuning the CVD deposition time and the precursor, the layer number of encapsulating graphene and N-doping on graphene could be controlled. The influences of graphene layer number and chemical doping on HER performances were investigated.

In chapter 5, the purpose is to understand the HER mechanism of graphene-encapsulated NiMo catalyst on the viewpoint of proton penetration. For this purpose, I investigated the proton penetration behaviour through graphene layers by electrochemical experiments and related energy barriers calculated by DFT.

In chapter 6, the purpose is to summarize the important experimental results and conclusions.

Chapter 2 Experimental methods

2.1 Synthesis of 3D porous NiMo alloy and HER measurements

2.1.1 Preparation of $NiMoO_4$ nanofiber

$NiMoO_4$ nanofibers, synthesized by a standard hydrothermal method[109], were used as precursors to obtain 3D porous NiMo alloy through a reductive annealing system. 2.5 mmol $NiCl_2 \cdot 6H_2O$ (98% purity, Wako Pure Chemical Industries, Osaka, Japan) and 2.5 mmol $Na_2MoO_4 \cdot 2H_2O$ (99% purity, Wako Pure Chemical Industries, Osaka, Japan) were dissolved in 30 mL deionized water, and then was transferred into a 50 mL Teflon coated stainless autoclave, which was kept at 150 °C for 12 h. After the autoclave cooling down to room temperature, the as-prepared $NiMoO_4$ nanofibers were washed by deionized water several times with a centrifuge and then kept in deionized water.

2.1.2 Preparation of 3D porous NiMo alloy

The $NiMoO_4$ nanofiber solution was dropped on Cu sheets, and then dried naturally for one day. The dried $NiMoO_4$ (5.0 g) was put into the center of a quartz tube (φ30 × φ27 × 1000 mm) furnace. The $NiMoO_4$ was reduced at various temperatures from 400 to 950 °C for 20 min under the mixed atmosphere of hydrogen (100 sccm) and argon (200 sccm) to reduce oxides for porous structure formation. After the annealing, the resulting reduced samples were removed from the Cu sheets for measurements.

2.1.3 Characterizations

The morphology and microstructure of 3D NiMo alloy were characterized by a scanning electron microscope (SEM, JSM-4300, JEOL, Tokyo, Japan). The X-ray diffraction (XRD) was carried out using a Rigaku SmartLab 9MTP diffractometer (Rigaku, Tokyo, Japan) with a 9.0 kW rotating anode generator (Cu Kα1 radiation; λ = 1.5406 Å). The X-ray photoelectron spectroscopy (XPS, AXIS ultra DLD, Shimazu, Tokyo, Japan) with Al Kα and X-ray monochromator was utilized for surface chemical compositions analysis. The surface area of porous NiMo sample was measured by the Brunauer–Emmett–Teller (BET) methods using a BELSORP-mini II (BEL Inc., Osaka, Japan) at 77.0 K. The sample was heated at 120 °C under vacuum for 48 h before the measurements.

2.1.4 Electrochemical measurements

Electrochemical measurements were conducted using an electrochemical workstation (VSP-300, Bio-Logic Science Instruments, Seyssinet-Pariset, France) equipped with a rotation disk electrode (RDE, 5 mm diameter glassy carbon, Hokuto Denko Corp., Tokyo, Japan). A graphite plate, an Ag/AgCl electrode (Hokuto Denko Corp., Tokyo, Japan) and the porous NiMo samples (5 mg) dispersed on the glassy carbon served as the counter electrode, the reference electrode and the working electrode, respectively. The porous NiMo samples and 10 wt. % Pt/C (Sigma-Ardrich, Tokyo, Japan) were dispersed uniformly on the surface of

the glassy carbon electrode using Nafion (5% DE521 CS type, Wako Pure Chemical Industries, Osaka, Japan) as a binder. The Ag/AgCl electrode was compared with a fresh Ag/AgCl electrode to check the differences of potential before use. All potentials were calculated with respect to reversible hydrogen electrode (RHE) using the equation: E(RHE) = E(Ag/AgCl) + 0.0591 × pH + 0.1976. The CV measurements after several cycles were recorded from −250 mV to +100 mV (vs. RHE) at a sweep rate of 10 mV s^{-1} in 1.0 M KOH electrolyte (pH = 13.9) deaerated with Ar (99.999%) with disk rotation speed of 1600 rpm to remove generated hydrogen bubbles. The obtained CV curves were calculated for an average of the current from the forward and the reverse sweeps to remove the capacitive background. The electrode potential in the hydrodynamic voltammogram was automatically *iR*-compensated with the Ohmic resistance measured at +200 mV (vs. RHE). The EIS measurement was carried out at −200 mV (vs. RHE) with an amplitude of 50 mV. The durability of the electrodes was tested by potential cycling between −250 mV to +100 mV (vs. RHE) at 30 mV s^{-1}. The electrolyte after 2000 CV cycle test was collected and analyzed through ICP−OES (Thermo Fisher Scientific IRIS Advantage DUO, Thermo Fisher Scientific Japan, Yokohama, Japan) to determine the leaching amount from NiMo catalyst.

2.2 Synthesis of graphene-encapsulated NiMo nanoparticles and HER measurements

2.2.1 Preparation of 3D porous N-doped graphene (3DNG) as substrate

The $NiMoO_4$ nanofiber solution was drop-casted on Cu sheets. All the water in the solution was completely evaporated at room temperature for one day. Then, the dried $NiMoO_4$ on Cu sheet was loaded on a corundum boat and inserted into the center of a quartz tube (φ30 × φ27 × 1000 mm) furnace. Through annealing at 950 °C for 1 hour with an atmosphere of H_2 (100 sccm) and Ar (200 sccm), NiMo alloy with porous structure was achieved. After that, the furnace temperature was set as 700 °C to grow N-doped graphene on porous NiMo alloy under a mixed atmosphere of H_2 (100 sccm), Ar (200 sccm) and pyridine (1 mbar, Aldrich, 99.8%, anhydrous) as carbon and nitrogen sources. The furnace was cooled by using a fan to room temperature. The above reduction and graphene growth procedure was considered as first CVD step. The samples were removed from the Cu sheets and etched by 0.5 M HNO_3 at 40 °C to achieve 3D porous N-doped graphene (3DNG).

2.2.2 Preparation of 3DNG supported NiMo nanoparticles (NiMoNPs) encapsulated by N-doped graphene

The as-prepared 3DNG was immersed in 0.15 M $[Ni(NH_3)_6]MoO_4$ solution, synthesized by mixing 5 mL of 0.3 M $NiMoO_4$ solution with 5 mL of $NH_3{\cdot}H_2O$ (wako, 28% in H_2O), for 12 hours, and then washed by 2-proponal several times. The resulting 3DNG with the Ni and Mo oxidized compounds was dried under vacuum at 40 °C for 5 hours to remove NH_3 and the compounds were deposited on 3DNG. Then, the 3DNG deposited with the compounds was similarly proceeded under the conditions of first CVD step to reduce the compounds and sequentially grow N-doped graphene on the compounds. The different CVD deposition times (1 s, 4 s, and 10 s) were used to achieve different numbers of N-doped graphene layers on the surface of reduced compounds (i.e., NiMo alloy nanoparticles, abbreviated as NiMoNPs) (1−2 layers, 3 layers and 6−7 layers).

2.2.3 Preparation of 3D porous non-doped graphene (3DG) supported NiMoNPs encapsulated by non-doped graphene

The 3DG supported NiMo nanoparticles encapsulated by non-doped graphene was similarly synthesized by the CVD conditions with benzene (1 mbar, Aldrich, 99.8%, anhydrous) instead of pyridine to grow non-doped graphene on the reduced compounds (i.e., NiMo alloy nanoparticles).

2.2.4 Characterizations

The morphology and microstructure of samples were characterized by SEM (JEOL JSM−4300), transmission electron microscopy (TEM) (JEOL JEM−2100F and JEM−ARM200F) and equipped EDS analysis (SDD Type, Detection surface area 30 mm^2, Solid angle 0.26 sr). Raman spectra were performed using a Renishaw InVia Reflex 532 with an incident wavelength of 532.5 nm. The laser power was set at 2.0

mW to avoid possible damage by laser irradiation. The samples were placed on a background-free glass slide. XRD was carried out using a RIGAKU SmartLab 9MTP diffractometer with a 9.0 kW rotating anode generator (Cu Kα1 radiation; λ = 1.5406 Å). The chemical bonding states of samples were studied by XPS (AXIS ultra DLD, Shimazu) with Al Ka and X-ray monochromator.

2.2.5 Catalyst leaching measurements

5 mg sample was completely dissolved into 50 mL acidic solution. The solution was analyzed by inductively coupled plasma optical emission spectrometry, abbreviated as ICP−OES, (ICP−8100, Shimazu) to determine the concentration of Ni and Mo in dissolved solution. Acidic electrolytes after 1000 CV cycles were filtered and collected. Then, their volumes were measured. After that, the collected electrolytes were analyzed through ICP−OES to make sure the concentration of Ni and Mo. The leaching ratio was calculated using the equation as below.

$$\text{Leaching ratio} = \frac{\text{Ni/Mo concentration in electrolyte (mg/L)}\times\text{electrolyte volume (L)}}{\text{Ni/Mo concentration in dissolve solution (mg/L)}\times\text{dissolved solution volume (L)}}$$

2.2.6 Electrochemical measurements

Electrochemical measurements were carried out using an electrochemical workstation (Biologic, VSP−300) equipped with a rotation disk electrode (RED, 5 mm diameter glassy carbon, HOKUTO DENKO corp.). All the electrochemical tests were performed in a three electrodes system. A graphite rod, a Ag/AgCl electrode and as-prepared catalysts (5 mg) dispersed on a glassy carbon RED were served as count electrode, reference electrode and working electrode, respectively. All potentials were calculated with respect to RHE using the equation: E(RHE) = E(Ag/AgCl) + 0.0591×pH + 0.197. The pH values (0.5~0.55) were recorded before the test and the Ag/AgCl reference electrode was calibrated before the test. The CV measurements after several cycles were recorded from −200 to +400 mV (vs. RHE) at a sweep rate of 10 mV s^{-1} in 0.5 M H_2SO_4 electrolyte deaerated with Ar (99.999%) with disk rotation speed of 1600 rpm to remove generated hydrogen bubbles. The obtained CV curves were calculated for an average of the current from the forward and the reverse sweeps to remove the capacitive background. The electrode potential in the hydrodynamic voltammogram was automatically *iR*-compensated with the Ohmic resistance measured at +200 mV (vs. RHE). The EIS test was recorded at −200 mV (vs. RHE). CV measurements with different scan rate from 5 to 30 mV s^{-1} at potential region between +100 to +200 mV (vs. RHE) in 0.5 M H_2SO_4 electrolyte were carried out to estimate the C_{dl} values[110]. The durability of the electrodes was tested through CV scans between −200 to 0 mV (vs. RHE) at a sweep rate of 30 mV s^{-1} in 0.5 M H_2SO_4 electrolyte.

2.2.7 Calculation of turnover frequency

The turnover frequency (TOF) values were calculated depend on the equation shown below[111, 112].

$$\text{TOF } per \text{ site} = \frac{\#\text{Total Hydrogen Turn Overs/geometric area (cm}^2\text{)}}{\#\text{Surface Sites (Catalyst)/geometric area (cm}^2\text{)}}$$

The total number of hydrogen turn overs was calculated from the current density according to the following equation.

$$\#\mathrm{H_2} = \left(j\,\frac{\mathrm{mA}}{\mathrm{cm^2}}\right)\left(\frac{1\ \mathrm{A}}{1000\ \mathrm{mA}}\right)\left(\frac{1\ \mathrm{C\ s^{-1}}}{1\ \mathrm{A}}\right)\left(\frac{1\ \mathrm{mol}\ e^-}{96485\ \mathrm{C}}\right)\left(\frac{1\ \mathrm{mol\ H_2}}{2\ \mathrm{mol}\ e^-}\right)\left(\frac{6.02214\times10^{23}\ \mathrm{molecules\ H_2}}{1\ \mathrm{mol\ H_2}}\right)$$

$$= \left(3.12\times10^{15}\,\frac{\mathrm{H_2\ s^{-1}}}{\mathrm{cm^2}}\,per\,\frac{\mathrm{mA}}{\mathrm{cm^2}}\right)$$

The surface sites of catalyst are calculated as following:

$$\frac{\#\text{Surface Sites (Catalyst)}}{\text{geometric area (cm}^2\text{)}} = \frac{\#\text{Surface Sites (Flat Standard)}}{\text{geometric area (cm}^2\text{)}} \times \text{Roughness Factor}$$

The property of active sites on catalyst surface was still not well understood, and the accurate number of HER active sites for H desorption is also unknown. Therefore, we assume that the total surface sites as the active sites, including both Ni and Mo atoms. Due to the predominant presence of NiMo alloy on the surface, NiMo is taken as an example to show the calculation of active sites per surface area as below,

$$\frac{\#\text{Surface Sites (Catalyst)}}{\text{geometric area (cm}^2\text{)}} = \left(\frac{56\ \text{atoms}\ per\ \text{unit cell}}{(734.32\times\text{Å})^3\ per\ \text{unit cell}}\right)^{\frac{2}{3}} = 1.8\times10^{15}\,\frac{\text{atoms}}{\text{cm}^2\ \text{surface area}}$$

The electrochemical active surface area (ECSA) can be converted using the specific capacitance values. The specific capacitance value of graphene-encapsulated NiMo nanoparticles is measured as 16800 μF cm^{-2}. The specific capacitance for a flat surface is generally found to be in the range of 20-60 μF cm^{-2}.[111, 113] The ECSA value can be calculated as following,

$$A_{\mathrm{ECSA}} = \frac{16800\ \mu\mathrm{F\ cm^{-2}}}{40\ \mu\mathrm{F\ cm^{-2}\ per\ cm^2_{ECSA}}} = 420\ \mathrm{cm^2_{ECSA}}$$

Finally, the TOF value are calculated as following,

$$\mathrm{TOF} = \frac{3.12\times10^{15}\frac{\mathrm{H_2\ s^{-1}}}{\mathrm{cm^2}}\,per\,\frac{\mathrm{mA}}{\mathrm{cm^2}}\times j\frac{\mathrm{mA}}{\mathrm{cm^2}}}{1.8\times10^{15}\frac{\text{atoms}}{\text{cm}^2\ \text{surface area}}\times420\ \mathrm{cm^2_{ECSA}}} = 0.004\times j\ \mathrm{H_2\ s^{-1}}$$

2.2.8 DFT calculations

The first-principles calculations were performed with the VASP code[114]. We used the projected augmented wave (PAW) method[115]. For the exchange and correlation functional, we used the Perdew-Burke-Ernzerhof (PBE) functional[116]. The plane wave energy cutoff was set to 400 Ry. The dispersion correction was included by the Grimme's D3 (BJ) method[117, 118].

Since the structure of the 1:1 NiMo could not be well characterized in the experiment, we assumed that the NiMo system forms the δ-phase NiMo: $Ni_{24}(Ni_4Mo_{16})Mo_{12}$,[116, 117] and its (100) face forms the surface of the NiMo system. The lattice constant of the NiMo(100) surface is known to be 8.852 Å × 9.108 Å[119, 120], while the lattice constant of the orthorhombic 2×4 cell of graphene, 8.52 Å × 9.838 Å. To compensate such a

lattice mismatch of the graphene layer and the NiMo(100) surface, we used the surface lattice constant of 8.852 Å × 9.563 Å. Note that this does not change the structures of both the NiMo(100) surface and the graphene layer. With this lattice constant, we put N-doped graphene layers on the NiMo(100) surface. 20 Å vacuum was inserted to avoid the artificial interaction between slabs. The Brillouin zone was sampled with the Monkhorst-Pack 4 × 4 × 1 k-grid. Each graphene sheet includes one graphitic N atom and one pyridinic N atom[121] per unit cell.

We adsorbed hydrogen atoms and calculated the adsorption energy. The hydrogen adsorption energy (ΔE_{H}) was calculated as

$$\Delta E_{\mathrm{H}} = \frac{1}{\mathrm{n}}(E_{\mathrm{tot}} - E_{\mathrm{sub}}) - \frac{1}{2}E_{\mathrm{H_2}}$$

where E_{tot} is the total energy of the substrate with n hydrogen atom adsorbed on the surface, E_{sub} is the total energy of the substrate, and E_{H2} is the energy of a hydrogen molecule in the gas phase (about −6.7 eV was employed in this work). The Gibbs free energy for the hydrogen absorption was corrected as

$$\Delta G_{\mathrm{H}} = \Delta E_{\mathrm{H}} + \Delta E_{\mathrm{ZPE}} - T\Delta S_{\mathrm{H}}$$

where ΔE_{ZPE} is the difference in zero-point energy between the adsorbed hydrogen and hydrogen in the gas phase and ΔS_{H} is the entropy difference between the adsorbed state and the gas phase. As the contribution from the vibrational entropy of H in the adsorbed state is negligibly small, the entropy of hydrogen adsorption is $\Delta S_{\mathrm{H}} \approx -1/2 S_{\mathrm{H}}$, where S_{H} is the entropy of H_2 in the gas phase. Then the Gibbs free energy with the overall corrections can be calculated as $\Delta G_{\mathrm{H}} = \Delta E_{\mathrm{H}} + 0.24$ eV.

We tested several positions of the N-doped graphene sheet with respect to the sheet below. Using the 2 layer sheets on NiMo(100), we added one H atom on one of the C atoms in the topmost layer and calculated ΔG_{H}. The ΔG_{H} value depends on the structure, while the difference was less than 0.05 eV. We adopted the position that has the lowest ΔG_{H} value. To calculate ΔG_{H} of the whole system, we added H atoms around the dopants.

2.3 Proton penetration through graphene layers

2.3.1 Fabrication of the Si_3N_4 chip supported Nafion/graphene/Nafion membrane

As shown in **Figure 2.1**, the monolayer graphene was grown on both sides of Cu foil after annealing at 1000 °C for 30 minutes using CH_4 as the carbon precursor (Step 2). O_2 plasma treatment was operated to remove the graphene on one side of Cu foil (Step 3), and then Nafion sheet was coated on the side with graphene through a spin coater (Step 4). The Cu foil was dissolved in 0.25 M $Fe(NO_3)_3$ solution at room temperature for 12 hours (Step 5). Before transfer, the ultrapure water (resistivity: 18.2 MΩ) was used to replace the $Fe(NO_3)_3$ solution for possible ions cleaning several times (Step 6). After transferring to a Si_3N_4 chip with an attached Nafion sheet in window area, the Nafion/graphene/Nafion membrane on Cu foil was achieved (Step 9). Finally, the chip was heated at 130 °C for 4 hours before using.

For a bilayer graphene membrane, one additional step is needed: transfer a Nafion protective monolayer graphene onto a Cu foil with monolayer graphene on one side (step 6). For another number of graphene layer membranes, such as trilayer or tetralayer, the steps from 5 to 7 are repeated.

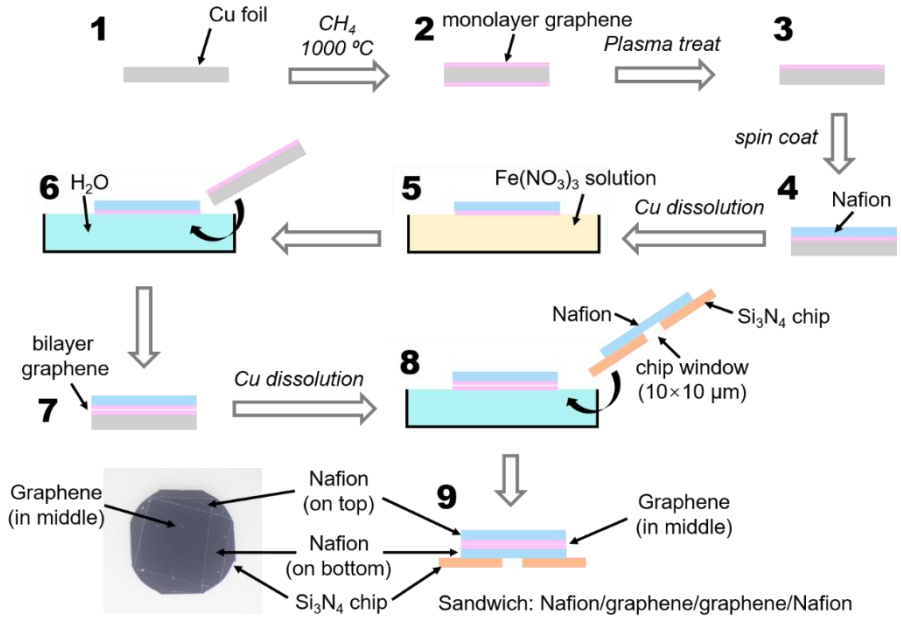

Figure 2.1 Fabrication of a Si_3N_4 chip supported Nafion/bilayer graphene/Nafion as separating membranes on the window area in Si_3N_4 chip.

2.3.2 The pH calculation by Nernst equation for the operation check of the cell.

The configuration of the cell and experimental setting are shown in **Figure 5.9**. Generally, if there are H^+ ions involved in the cell reaction, the cell potential will depend on the pH values.

For the half reaction, $2H^+ + 2e^- \rightarrow H_2$, $E^o = 0$

$$2\mathrm{H}^+ + 2e^- \rightarrow \mathrm{H}_2,\ E^\mathrm{o} = 0$$

According to the Nernst equation,

$$E_{\mathrm{H}^+/\mathrm{H}_2} = E^\mathrm{o} - \frac{RT}{nF}\ln\left(\frac{P_{\mathrm{H}_2}}{[\mathrm{H}^+]^2}\right)$$

where E is the cell potential, E^o is the standard cell potential, R is the universal gas constant, T is the temperature in kelvins, n is the number of transferred electrons in the half reaction, F is the Faraday constant, P_{H_2} is the H_2 pressure, and $[\mathrm{H}^+]$ is the concentration of H^+ ions.

If P_{H_2} = 1 atm, and T = 298 K,

$$E_{\mathrm{H}^+/\mathrm{H}_2} = 0 - \frac{8.314\ \mathrm{J\ K^{-1}} \times 298\ \mathrm{K}}{2 \times 96485\ \mathrm{J\ V^{-1}}}\ln\left(\frac{1}{[\mathrm{H}^+]^2}\right) = 0.059 \times \log[\mathrm{H}^+]$$

Combined with $\mathrm{pH} = -\log[\mathrm{H}^+]$,

$$E_{\mathrm{H}^+/\mathrm{H}_2} = (-0.059 \times \mathrm{pH})\ \mathrm{V}$$

Based on the experimentally measured pH values of two chambers (1.74 and 0.5) in **Figure 5.9**, the potential difference should be,

$$E = |-0.059 \times (1.74 - 0.5)| = 0.073\ \mathrm{V} = 73\ \mathrm{mV}$$

2.3.3 DFT calculations

In addition to the DFT calculations with CP2K described in the main text, we also performed DFT calculations with the VASP[114] code to estimate the energy barrier for hopping of proton from graphene to the NiMo surface. We used the projected augmented wave (PAW) method[115] and the Perdew-Burke-Ernzerhof (PBE) functional[116]. The plane wave energy cutoff was set to 400 Ry. The dispersion correction was included by the Grimme's D3 (BJ) method[117, 118].

The NiMo surface covered by a graphene with SV-3N defect was prepared based on our previous paper[79]. Since the structure of the 1:1 NiMo could not be well characterized in the experiment, we assumed that the NiMo system forms the δ-phase NiMo: $Ni_{24}(Ni_4Mo_{16})Mo_{12}$,[122, 123] and its (100) face forms the surface of the NiMo system. The lattice constant of the NiMo(100) surface is known to be 8.852 Å × 9.108 Å, while the lattice constant of the orthorhombic 2×4 cell of graphene, 8.52 Å × 9.838 Å. To compensate such a lattice mismatch of the graphene layer and the NiMo(100) surface, we used the surface lattice constant of 8.852 Å × 9.563 Å. Note that this does not change the structures of both the NiMo(100) surface and the graphene layer. With this lattice constant, we put N-doped graphene layers on the NiMo(100) surface. 20 Å vacuum was inserted to avoid the artificial interaction between slabs. The Brillouin zone was sampled with the Monkhorst-Pack 4×4×1 k-grid.

Chapter 3 3D porous NiMo alloy: an efficient HER catalyst

Due to the high HER activity of NiMo alloy and the various advantages of porous materials as electrochemical catalysts mentioned in section 1.1.4, the NiMo alloy with 3D porous structure could be an alternative to the high-cost Pt metal as an efficient HER catalyst. In this chapter, the 3D porous NiMo alloy was synthesized through a simple two-step method (hydrothermal process−annealing process). The effect of annealing temperature on the formation of porous structure was systematically investigated by SEM. The catalyst composition and surface chemical state were investigated by XRD and XPS measurements. Moreover, the electrochemical performances of resulting porous NiMo alloy samples were tested in 1.0 M KOH electrolyte in comparison to the commercial Pt catalyst. The durability test in 1.0 M KOH electrolyte was further carried out by CV and chronoamperometry (CA) measurements.

3.1 Synthesis of 3D porous NiMo alloy

The fabrication process of 3D porous NiMo alloy, illustrated in **Figure 3.1**, was divided into two main procedures. Firstly, the $NiMoO_4$ nanofibers, the precursor of porous NiMo, were synthesized through a standard hydrothermal method at 150 °C for 12 h. Secondly, the resulting $NiMoO_4$ nanofibers dropped on Cu sheets and inserted into a quartz tube furnace were annealed at 400~950 °C for 20 min under the mixed gases of hydrogen and argon to reduce the oxidized precursor. After the furnace cooling down to room temperature, the annealed $NiMoO_4$ samples were peeled off from the Cu sheets for characterizations and measurements. Moreover, the sheet area easily reached to 2.0 cm^2 (**Figure 3.1**) when the area of Cu sheet was tuned.

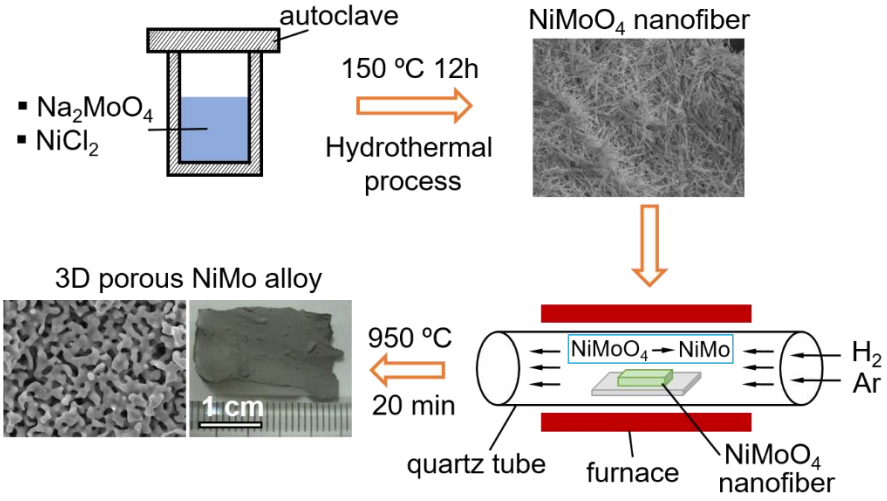

Figure 3.1 Schematic illustration of the synthesis process of 3D porous NiMo alloy.

3.2 Effect of the annealing temperature on porous structure formation

The morphologies of annealed $NiMoO_4$ samples were investigated to reveal the formation process of porous structures with scanning electron microscope (SEM) measurements. The nanofiber structure of the pristine $NiMoO_4$ was kept at low temperatures ranged from 0 to 500 °C (**Figures 3.2a–c**), and some nanoparticles were generated on the surface of nanofibers at 500 °C due to the reduction of $NiMoO_4$ nanofibers (inset of **Figure 3.2c**). When the temperature reached 600 °C, the generated nanoparticles started to fuse and reconstruct each other to be energetically stable due to the high geometric potential at the nanoparticle state (**Figure 3.2d**). The pristine nanofiber structures totally disappeared at 700 °C and the ligaments in the porous structures were gradually formed with pore size less than 100 nm (**Figure 3.2e**). The 3D open porous structures were developed and the porous structures became bicontinuous and interconnected above 800 °C (**Figure 3.2f**). The porous structures were well developed, and the pore size increased from tens of nanometers to a few hundred nanometers with the temperature ranging from 800 to 950 °C (**Figures 3.2g** and **3.2h**). The view of the cross-section of sample annealed at 950 °C showed the open and bicontinuous structures were well preserved in the inside of the sample sheets (**Figure 3.2i**).

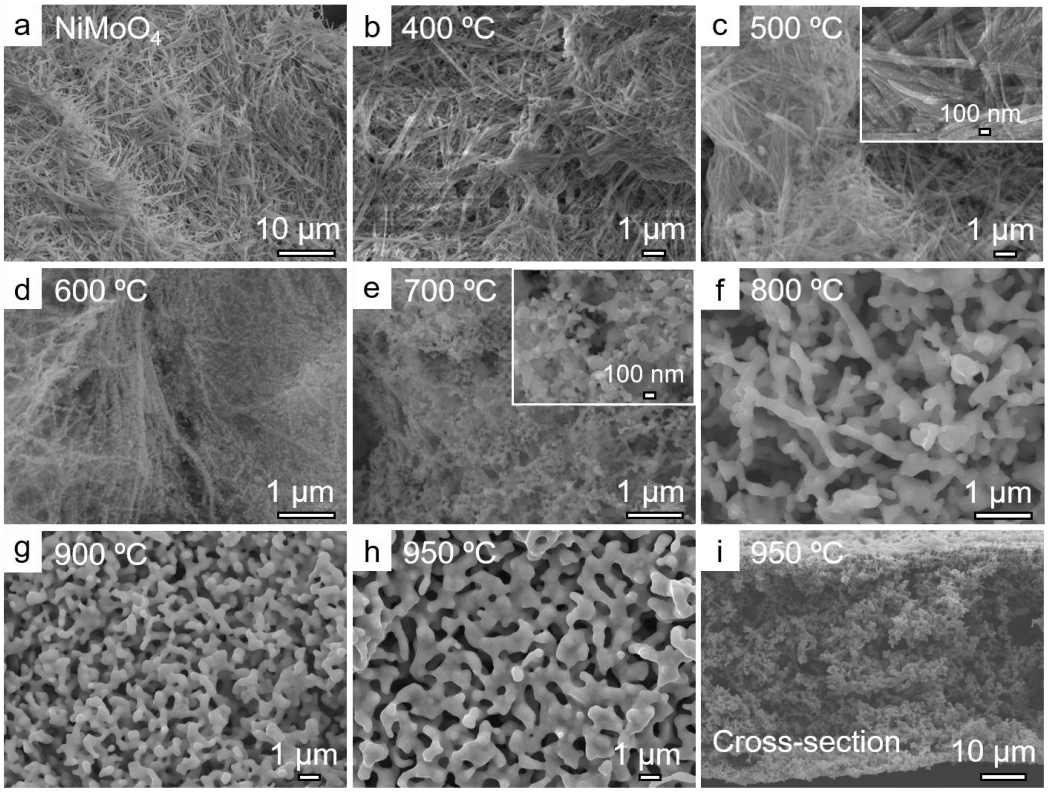

Figure 3.2 Morphologies of $NiMoO_4$ samples annealed at various temperatures. SEM images of (a) pristine $NiMoO_4$ nanofiber; (b–i) temperature effect on 3D porous structure formation of samples annealed at 400~950 °C. The insets in (c and e) show high resolution SEM images.

3.3 Effect of the annealing temperature on chemical composition

The crystal structures of annealed $NiMoO_4$ samples were studied by X-ray diffraction (XRD) measurements. The pristine $NiMoO_4$ nanofibers and sample annealed at 400 °C matched well with the $NiMoO_4 \cdot xH_2O$ (JCPDS #13−0128) (**Figure 3.3a**). When the annealing temperature ranges between 500 and 600 °C, the obtained peaks were well assigned to $NiMoO_4$ (JCPDS #33−0948) (**Figures 3.3a** and **3.3b**). This can be explained with the complete removal of crystal water at 500~600 °C. At 700 °C, some $NiMoO_4$ were reduced and decomposed under the reducing atmosphere, partly forming NiO (JCPDS #71−1179) and MoO_2 (JCPDS #65−5787) (**Figure 3.3b**). Above 800 °C, the composition of NiMo (JCPDS #48−1745) and Ni_4Mo (JCPDS #65−5480) were gradually generated and oxidized species of NiO and MoO_2 were gradually reduced (**Figure 3.4**). It is worth noting that the reduction of $NiMoO_4$ requires 800 °C and reduction of MoO_2 requires 950 °C. Thus, the sample annealed at 950 °C obtained NiMo phase with a certain amount of Ni_4Mo phase. The specific surface area of the porous NiMo annealed at 950 °C was measured by the nitrogen adsorption and desorption method. The surface area was estimated as 2.81 m^2/g (**Figure 3.5**).

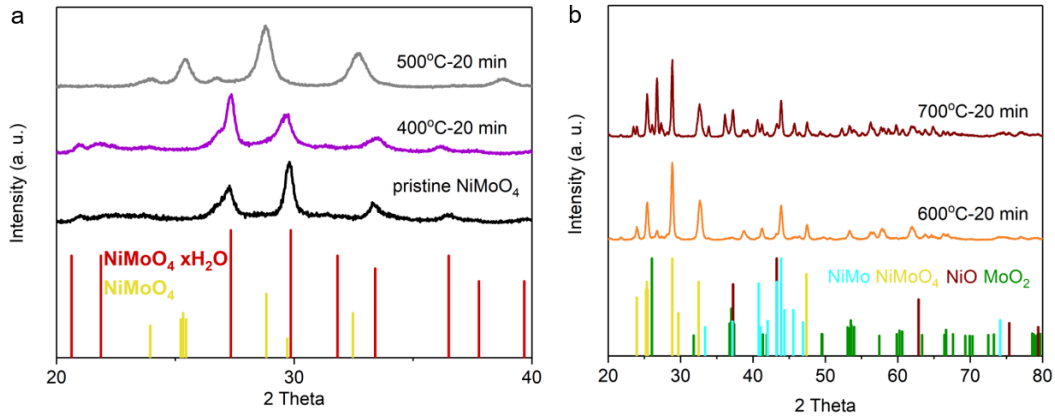

Figure 3.3 The XRD patterns of pristine $NiMoO_4$ sample and samples annealed at various temperatures for 20 minutes.

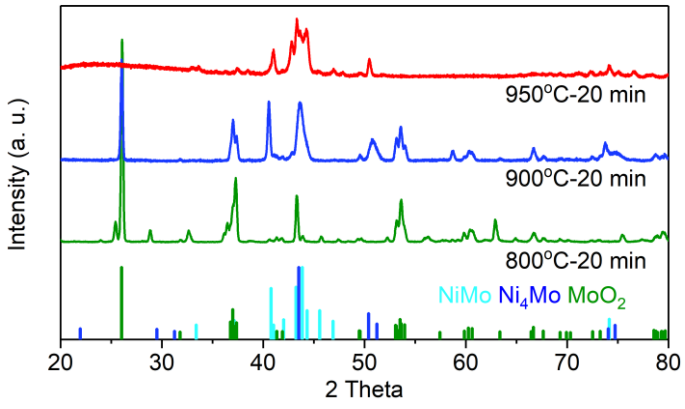

Figure 3.4 The XRD patterns of samples annealed at 800, 900, and 950 °C for 20 minutes.

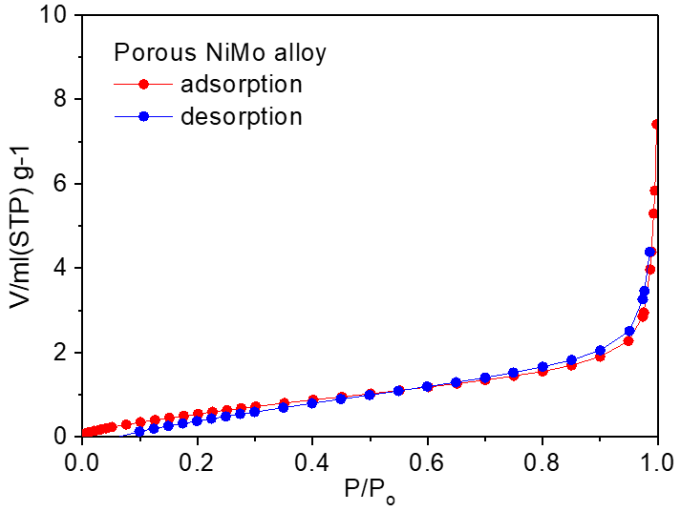

Figure 3.5 Nitrogen absorption and desorption measurements of porous NiMo alloy annealed at 950 °C for 20 min.

The surface chemical compositions of porous NiMo and Ni_4Mo alloy samples annealed at 900 and 950 °C were tested by X-ray photoelectron spectroscope (XPS) measurements. The high-resolution Ni 2p spectrum of the sample annealed at 900 °C revealed that the main peaks are assigned to Ni (852.6 eV, 869.6 eV) and NiO (855.9 eV, 873.6 eV) (**Figure 3.6a**), while the NiO peaks are negligibly small in the sample annealed at 950 °C (**Figure 3.6c**)[124, 125, 126]. These results further indicate that Ni oxides were completely reduced at 950 °C. The high-resolution Mo 3d spectrum of samples annealed at 900 °C were deconvoluted into six distinct peaks at 227.4 eV, 230.6 eV, 228.5 eV, 231.6 eV, 232.1 eV and 235.2 eV, assigning to NiMo, Ni_4Mo and Mo oxide, showing alloy and oxidized surface state (**Figure 3.6b**)[127, 128, 129]. The sample annealed at 950 °C presents major NiMo (94.4 at %) with negligible Ni_4Mo (1.5 at %) and Mo oxide on the surface, further confirming the almost complete reduction of Mo oxide (4.1 at %, probably oxidized during the transfer to XPS equipment) at 950 °C (**Figure 3.6d**). These XPS results are in good agreement with the XRD results. Considering XRD and XPS results during the reduction process, the following sequential transformations are proposed: (1) the reduction of pristine $NiMoO_4$ to partly-reduced $NiMoO_4$ nanoparticles; (2) the reconstruction and fusion of the further-reduced $NiMoO_4$ nanoparticles to decrease the surface energy; and (3) the complete reduction of $NiMoO_4$ nanoparticles for the formation of ligaments into porous NiMo structures, developing 3D porous NiMo alloy.

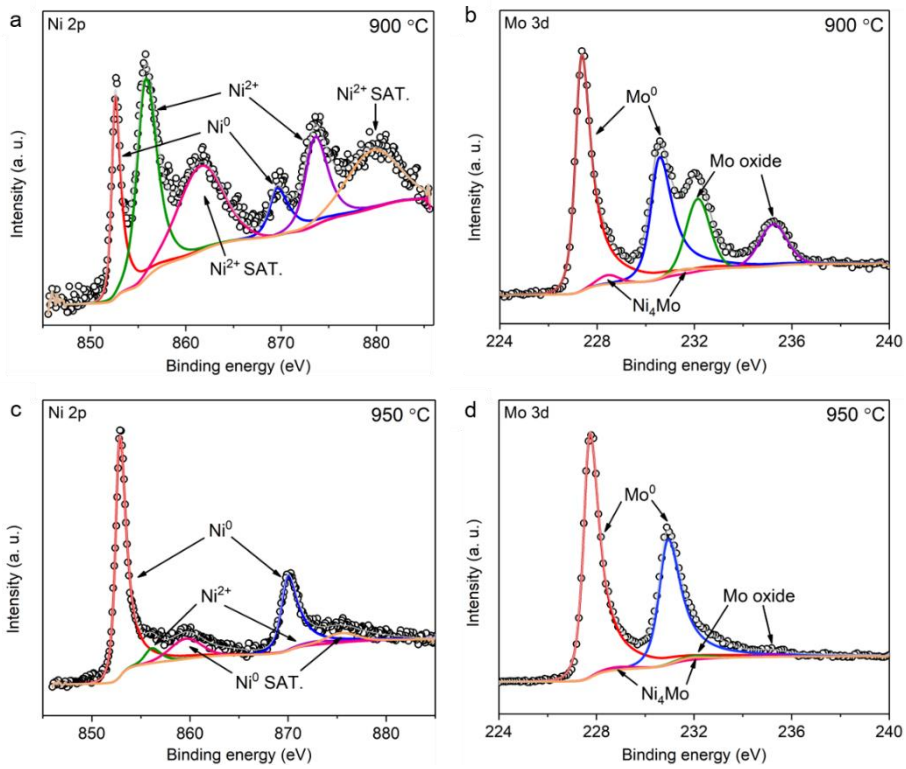

Figure 3.6 High-resolution XPS spectra of nickel 2p and molybdenum 3d spectra on porous NiMo samples annealed at (a, b) 900 °C for 20 min and (c, d) 950 °C for 20 min.

3.4 Electrochemical measurements

The samples with different annealing temperatures of 800 °C, 900 °C and 950 °C (abbreviated as NiMo−800 °C, NiMo−900 °C and NiMo−950 °C) with the comparison of commercial 10 wt. % Pt/C and the pristine $NiMoO_4$ nanofibers were tested in 1.0 M KOH solution to investigate the catalytic HER activities (**Figure 3.7a**). The polarization curve of NiMo−950 °C exhibits a Pt-like HER activity, reaching a current density of 10 mA cm^{-2} at an overpotential of 18 mV, which is only 2 mV larger than the value achieved by 10 wt. % Pt/C. Turnover frequency (TOF) normalized by the BET surface area at an electrode potential of −100 mV (vs. RHE) was roughly estimated and the value was 0.84 H_2 s^{-1} for NiMo−950 °C sample and the TOF value was relatively higher reported NiMo electrode (**Table 3.1**). This means that the intrinsic catalyst activity of the NiMo−950 °C sample was enhanced by the bi-continuous porous structures. The NiMo−900 °C and NiMo−800 °C reveal a gradual declining trend of HER catalytic activity, which achieves 10 mA cm^{-2} at an overpotential of 66 mV and 182 mV. This decline indicates that the existence of Mo oxide and Ni oxide dramatically interferes with HER processes, and the HER activity can be greatly enhanced only with the complete reduction of the oxides at 950 °C. Indeed, the fully oxidized $NiMoO_4$ nanofiber exhibits no HER catalytic activity. The Tafel plots estimated from the polarization curves (**Figure 3.7b**) show that the NiMo−950 °C achieves a Tafel slope of 36 mV/decade and 10 wt. % Pt/C (loading amount: 1 mg) exhibits 30 mV/decade. Therefore, the Heyrovsky desorption process ($H_2O + e^- + H^* \rightarrow H_2 + OH^-$), where H*

represents adsorbed H atom on catalytic site *) could be the rate determining step for the NiMo−950 °C in 1.0 M KOH electrolyte[130]. The Tafel slopes of NiMo−900 °C and NiMo−800 °C are 72 mV/decade and 147 mV/decade, indicating the mixed Volmer-Heyrovsky process ($H_2O + e^- + H^* \rightarrow H_2 + OH^-$ and $H_2O + e^- \rightarrow H^* + OH^-$) are the corresponding rate determining steps[38, 131]. The EIS measurements were further carried out to measure the charge-transfer resistances (R_{ct}) of the porous NiMo alloys at an overpotential of 200 mV vs. RHE (**Figure 3.7c**). The internal resistances of NiMo−800 °C, NiMo−900 °C and NiMo−950 °C are almost the same value of 5 Ω. The NiMo−950 °C exhibits quite low R_{ct} value of 7.9 Ω, which far lower than the 19.8 Ω for NiMo−900 °C and the 26.5 Ω for NiMo−800 °C, confirming more efficient reaction kinetics of the NiMo−950 °C sample. All electrochemical properties are listed in **Table 3.1**.

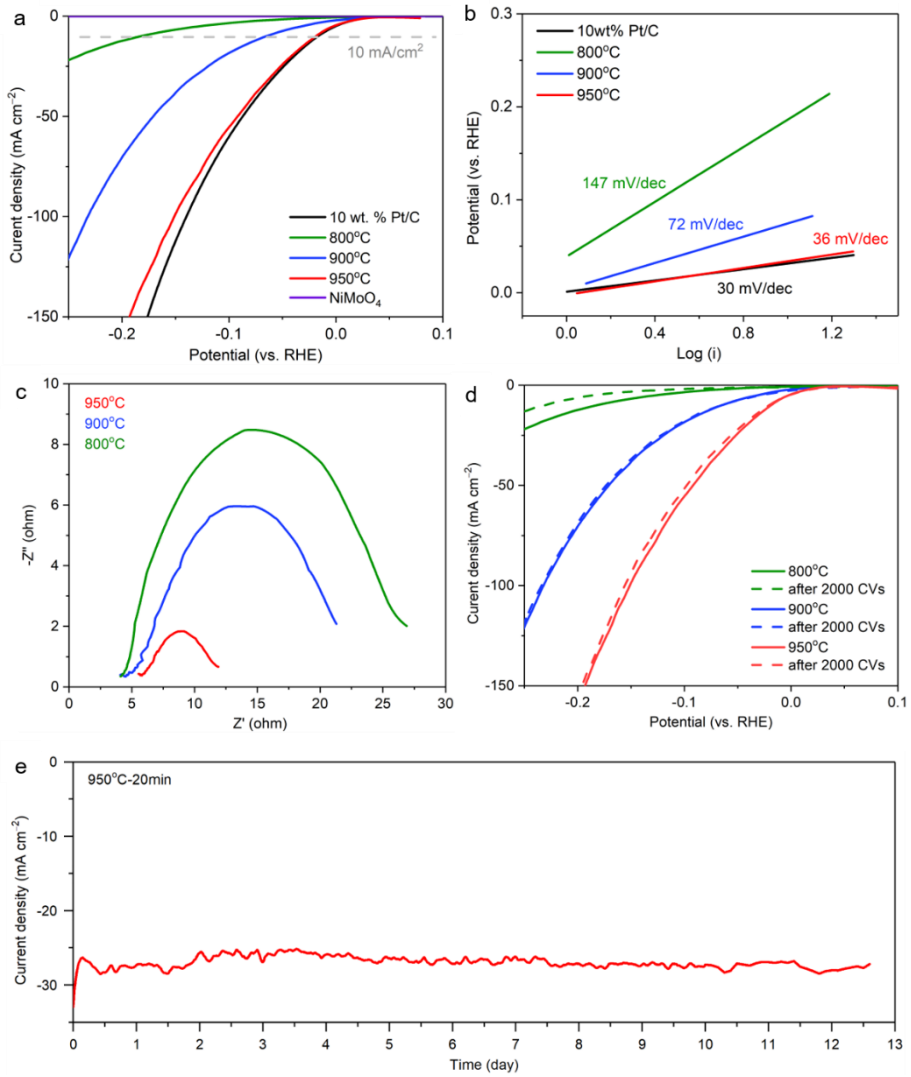

Figure 3.7 Electrochemical measurements. (a) The HER polarization curves of porous NiMo samples annealed at 800, 900, and 950 °C, pristine $NiMoO_4$ nanofibers and 10 wt. % Pt/C. (b) Corresponding Tafel plots from (a). (c) Electrochemical impedance spectra of porous NiMo samples annealed at 800, 900, and 950 °C at an overpotential of 200 mV vs. RHE. (d) Polarization curves of porous NiMo samples annealed at 800, 900, and 950 °C before and after 2000 CV cycles.

Long-term durability is an important criterion for HER cathodes. The CV and CA measurements were utilized to investigate the stability of porous NiMo alloy at an electrode potential of −200 mV (vs. RHE) in 1.0 M KOH electrolyte. The polarization curves of NiMo−900 °C and NiMo−950 °C after 2000 CV cycles exhibit extremely high durability (**Figure 3.7d**). The overpotential of NiMo−950 °C at 100 mA cm^{-2} only increases by 5 mV (150 to 155 mV) after the 2000 CV cycles. During the CA measurement (**Figure 3.7e**), the NiMo−950 °C (loading amount: 1.0 mg) keeps original performances of 27 mA cm^{-2} for 12.5 days at an overpotential of 200 mV. A rotating disk electrode was not used for the CA test, resulting in some bubbles blocking the surface and a slight decrease of the current density. To understand the superb HER performances and chemical stability, the SEM images of the NiMo-950 °C after 2000 CV cycles were investigated. The bicontinuous porous structure was well preserved in 1.0 M KOH electrolyte (**Figure 3.8**). In addition, the ICP−OES was used to investigate the leaching amount of the NiMo electrode after 2000 cycle test. The results reveal that the dissolution amount of Ni and Mo is less than 0.6 at % and 0.3 at % (under the detection limit), which further confirms the prominent stability. Thus, chemically stable and well-crystalized porous NiMo−950 °C alloy electrode plays an important role in outstanding HER performances.

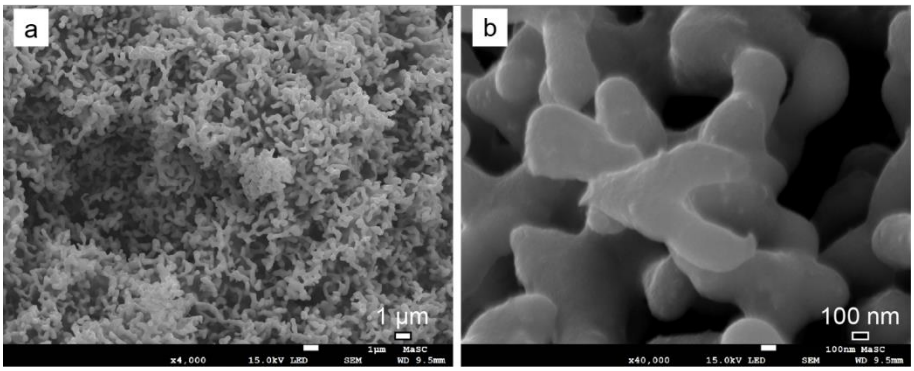

Figure 3.8 Morphologies of porous NiMo samples annealed at 950 °C after 2000 CV cycles. (a) Overview and (b) zoom-in images.

3.5 Conclusions

In this chapter, the syntheses, characterizations, and electrochemical properties of 3D porous NiMo alloy were investigated. The formation of porous structures requires 800 °C annealing temperature, and the complete reduction of Mo oxide species needs the temperature beyond 950 °C. The bi-continuous and conductive porous structure with larger surface area enhance the intrinsic catalyst activity of NiMo alloy, which can be employed as cathodes for electrochemical water splitting devices without losing their catalytic abilities in 1.0 M KOH electrolyte for 12.5 days. Noticeably, the cost of synthesized precursor is as low as 37 JPY per gram, which shows a prospect for large-scale productions. Such non-noble, cost-efficient, and 3D porous alloys could be good replacements to noble metal catalysts such as Pt, which has been one of the undue barriers to sustaining worldwide use due to high price and low world supply. Therefore, the

development and study of non-noble porous metals as low-cost, earth-abundant HER catalysts offer hopeful alternatives to Pt-based catalysts for the achievement of hydrogen societies.

Table 3.1 The HER performances of porous NiMo alloy and other reported catalysts.

Catalyst	Onset potential (mV)	Overpotential (mV) at 10 mA cm^{-2}	Tafel slope (mV/decade)	TOF (H_2 s^{-1})	Electrolyte	Reference
3D porous NiMo	2	18	36	0.89 at −100 mV	1.0 M KOH	This work
NiMoN	32	109	95	-	1.0 M KOH	Adv. Energy Mater. 2016, 6, 1600221
CoP	-	54	51	-	1.0 M KOH	Adv. Funct. Mater. 2015, 25, 7337
$NiMoN_X/C$	78	300	36	-	0.1 M $HClO_4$	Angew. Chem. Int. Ed. 2012, 51, 6131
NiCoP	-	167	71	0.056 at −100 mV	1.0 M KOH	Chem. Commun. 2016, 52, 1633
Mo_2C	37	112	55	-	0.1 M KOH	Angew. Chem. Int. Ed. 2015, 54, 15395
NiMo nanopowders	20	126	-	-	1.0 M KOH	ACS Catal. 2013, 3, 166
WC/CNTs	45	150	106	-	0.1 M KOH	ACS Nano 2015, 9, 5125
$CoSe_2$	80	200	85	-	1.0 M KOH	Adv. Mater. 2016, 28, 7527
ZnCoS	40	100	48	-	0.1 M KOH	J. Am. Chem. Soc. 2016, 138, 1359
Co/Co_3O_4	30	95	44	-	1.0 M KOH	Nano Lett. 2015, 15, 6015
CoMoP@C	-	81	55	-	1.0 M KOH	Energy Environ. Sci. 2017, 10, 788
Ni_3S_2@NPC	30	61	68	-	1.0 M KOH	Nano Energy, 2017, 36, 85
Ni_4Mo	0	15	30	0.4 at −50 mV	1.0 M KOH	Nat. Commun. 2017, 8, 15437
NiCN	10	31	40	8.52 at −200 mV	1.0 M KOH	J. Am. Chem. Soc. 2016, 138, 14546
$Ru@C_2N$	9.5	20	30	-	1.0 M KOH	Nat. Nanotechnol. 2017, 12, 441
Ni_5P_4	-	49	98	0.79 at −100 mV	1.0 M KOH	Energy Environ. Sci. 2015, 8, 1027

Chapter 4 Graphene-encapsulated NiMo alloys as an acid-stable HER catalyst

In this chapter, the graphene-encapsulated NiMo alloy nanoparticles were synthesized by CVD method. The number of encapsulating graphene layers was precisely controlled by tuning the CVD deposition time. In this case, the effect of graphene layer number on the HER performance can be investigated. SEM, TEM, XRD, and XPS measurements were used to study the structural characterizations. The electrochemical characteristics were studied by CV and CA. ICP−OES checked the element leaching of catalysts during stability tests. Finally, the DFT calculations were utilized to analyze the Gibbs free energy of H adsorption and charge distributions.

4.1 Synthesis of 3DNG supported graphene-encapsulated NiMo nanoparticles

The fabrication of 3DNG-supported NiMo nanoparticles encapsulated by N-doped graphene is illustrated in **Figure 4.1**. Initially, $NiMoO_4$ nanofibers were reduced at 950 °C in a H_2/Ar atmosphere[132], followed by growth of N-doped graphene layers (NGLs) on the as-obtained 3D porous NiMo at 700 °C for 15 s in a mixed H_2, Ar, and pyridine atmosphere using a standard CVD method. Subsequently, the 3D porous NiMo was fully covered by NGLs and then etched using HNO_3 to isolate 3DNG as the substrate for NiMoNPs deposition; this step was performed using $[Ni(NH_3)_6]MoO_4$ precursor solution[56]. With the loss of ammonia under vacuum, Ni/Mo oxide compounds were generated on the 3DNG surface. Finally, the graphene-encapsulated NiMo catalysts were obtained via reduction of the as-deposited oxide at 950 °C and subsequent NGL growth at 700 °C for variable deposition times (1, 4, and 10 s for 1−2, 3, and 6−7 NGLs, respectively). The NiMoNPs encapsulated by 1−2, 3, and 6−7 NGLs abbreviate as 1−2NGL, 3NGL, and 6−7NGL, respectively. In addition, the benzene was used to replace the pyridine as the precursor to grow non-doped graphene layers on NiMoNPs with the same synthesis processes. The NiMoNPs encapsulated by 1−2 layers non-doped graphene abbreviates as 1−2GL.

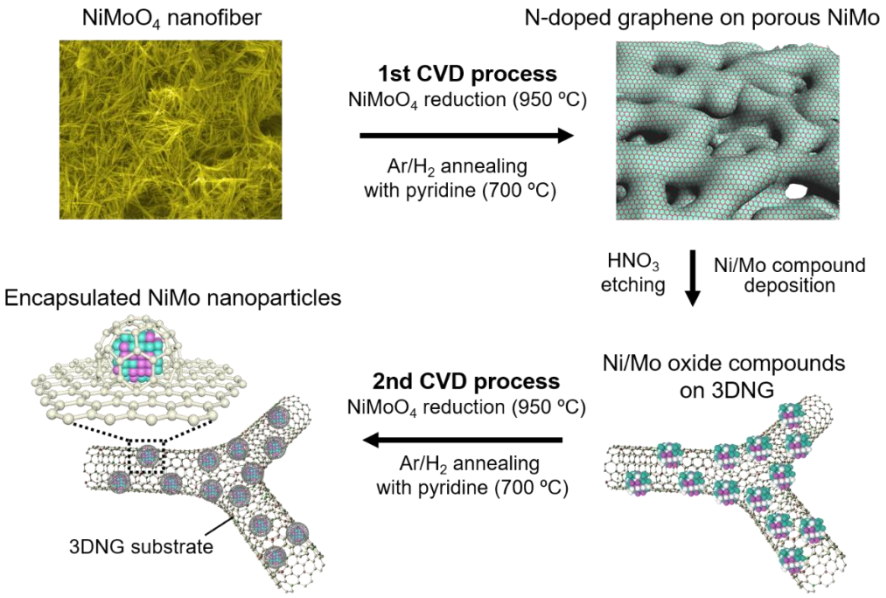

Figure 4.1 Syntheses processes of N-doped graphene-encapsulated NiMoNPs on 3DNG substrate.

4.2 Structural characterizations of graphene-encapsulated NiMo nanoparticles

SEM and TEM images showed that the graphene-encapsulated NiMo catalysts had a bicontinuous and open porous structure (pore radius=300−500 nm; **Figure 4.2a**) containing interconnected graphene sheets (**Figure 4.3a**), whereas dark-field scanning TEM (DF-STEM) imaging (**Figure 4.2b**) demonstrated uniformly distributed reduced NPs with an average diameter of 11.3 nm on the 3DNG surface (**Figure 4.3b**). Selected area electron diffraction (SAED) patterns showed sharp diffraction spots, confirming the high crystallinity of multilayer graphene (inset of **Figure 4.2b**). High-resolution TEM (HRTEM) imaging revealed lattice fringes with distances of 2.2 and 3.4 Å, corresponding to the (041) facet of NiMo and the (002) facet of graphene (**Figure 4.2c**), respectively. Energy-dispersive X-ray spectroscopy (EDS) confirmed that Ni and Mo atoms were homogeneously distributed on the NPs (**Figure 4.2d**), with a mismatch between the C and Mo/Ni distributions. The frequency distribution histogram confirms that the 1−2NGL catalyst with an average graphene layer number of 1.8 (**Figure 4.3c**). Structural characterizations of 3NGL and 6−7NGL catalysts were also observed (**Figures 4.4a, b, d**, and **e**). The histograms indicate that the average layer numbers of encapsulating graphene are 3.0 and 6.5 for 3NGL and 6−7NGL catalysts, respectively (**Figures 4.4c** and **f**).

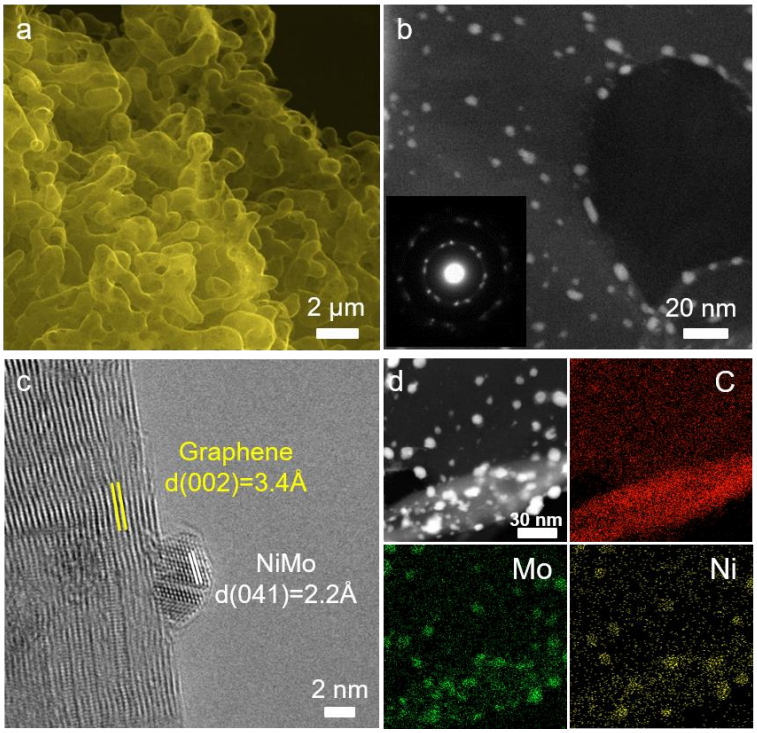

Figure 4.2 Structural characterizations of graphene-encapsulated NiMo nanoparticles. (a) Cross-sectional SEM image of graphene-encapsulated NiMo catalysts. (b) DF-STEM image of uniformly dispersed NPs on 3DNG and corresponding SAED pattern (inset). (c) Typical HRTEM image of the NiMo NP encapsulated by a monolayer graphene sheet on 3DNG. (d) DF-STEM image and corresponding EDS elemental mappings of graphene-encapsulated NiMo catalysts. Copyright 2018 American Chemical Society.

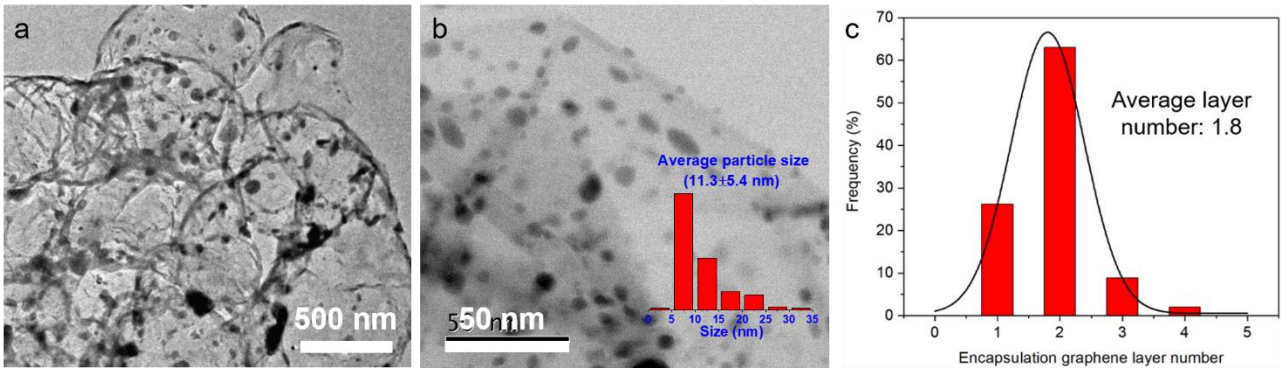

Figure 4.3 TEM images of graphene-encapsulated NiMo nanoparticles. Typical low-resolution (a) TEM and (b) BF-STEM images of graphene-encapsulated NiMo catalysts. The size distribution of nanoparticles on 3DNG substrate (inset of b). The data is randomly collected from 100 nanoparticles. (c) The frequency distribution histogram of the number of encapsulating graphene layers in 1−2NGL catalyst. The data were collected from 25 HRTEM images that included ~60 encapsulated nanoparticles. Copyright 2018 American Chemical Society.

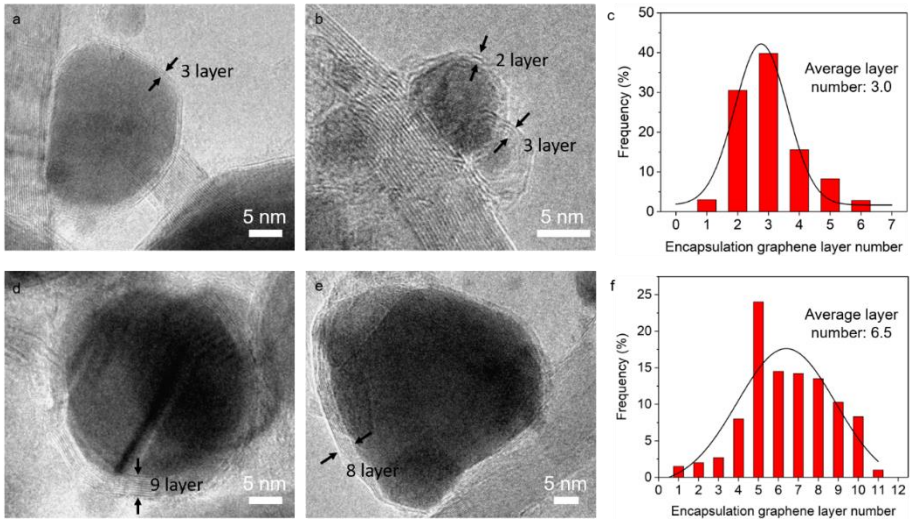

Figure 4.4 Structural characterizations of NiMo nanoparticles encapsulated by 3 and 6−7 NGLs (3NGL and 6−7NGL catalysts). HRTEM images of (a, b) the 3NGL catalyst and (d, e) the 6−7NGL catalyst. (c, f) The frequency distribution histogram of the number of encapsulating graphene layers in 3NGL and 6−7NGL catalysts.

Structural characterization was performed using X-ray diffraction (XRD) and Raman spectroscopy. As illustrated in the XRD pattern (**Figure 4.5a**), the graphene-encapsulated NiMo catalysts mainly comprised different NiMo alloy phases such as NiMo (JCPDS No. 48−1745) and $MoNi_4$ (JCPDS No. 65−5480). The Raman spectrum of 1−2NGL catalyst showed the value of D to G band intensity ratio (I_D/I_G) was 0.55 (**Figure 4.5b**), which indicates that the rich numbers of defects in graphene lattices caused by N doping. In contrast, the I_D/I_G value was 0.07 for 1−2GL catalyst, which is contributed to the topological defects in the encapsulating graphene−graphene substrate junction regions or curved regions of 3DNG substrate[133]. The presented values of 2D to G band intensity ratio (I_{2D}/I_G) confirms the characteristics of multilayer graphene.

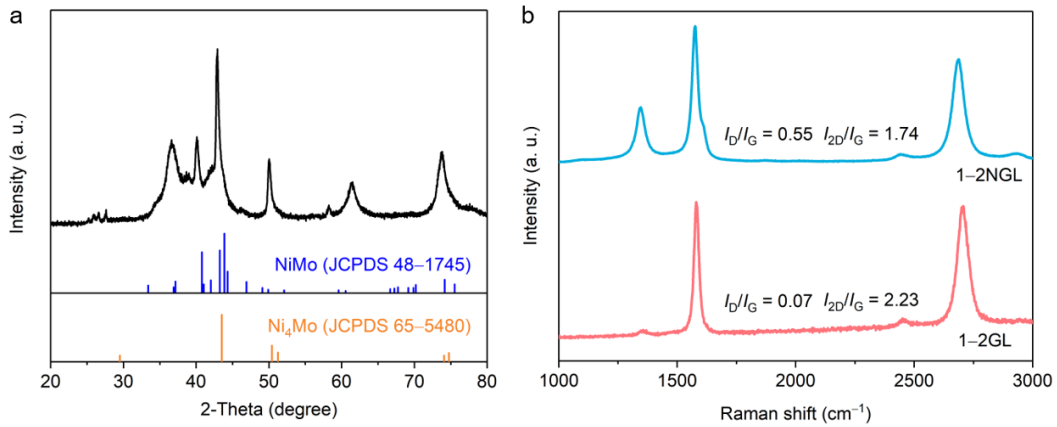

Figure 4.5 XRD and Raman characterizations of graphene-encapsulated NiMo catalysts. (a) XRD pattern. (b) Raman spectra of 1−2NGL and 1−2GL catalysts.

The surface chemical states of graphene-encapsulated NiMo catalysts were probed by XPS. The Ni 2p spectrum showed signals of Ni^0 (852.9 eV) and Ni^{2+} (856.0 eV)[134] (**Figure 4.6a**). The Mo 3d spectrum could be deconvoluted into dominant Mo^0 (228.1 and 231.2 eV)[135] and $MoNi_4$ (229.2 and 231.6 eV)[46] peaks with small contributions of Mo oxide (232.4 and 235.3 eV)[46] (**Figure 4.6b**). The XPS Ni 2p and Mo 3d spectra confirm the metallic state of Ni and Mo is dominated on catalyst surface. The C 1s spectrum showed the characteristic of high-quality graphene[136] (**Figure 4.6c**). The N 1s spectrum exhibited the N dopants in graphene lattices are in form of pyridinic N, graphitic N, and oxidized N[121, 137] (**Figure 4.6d**).

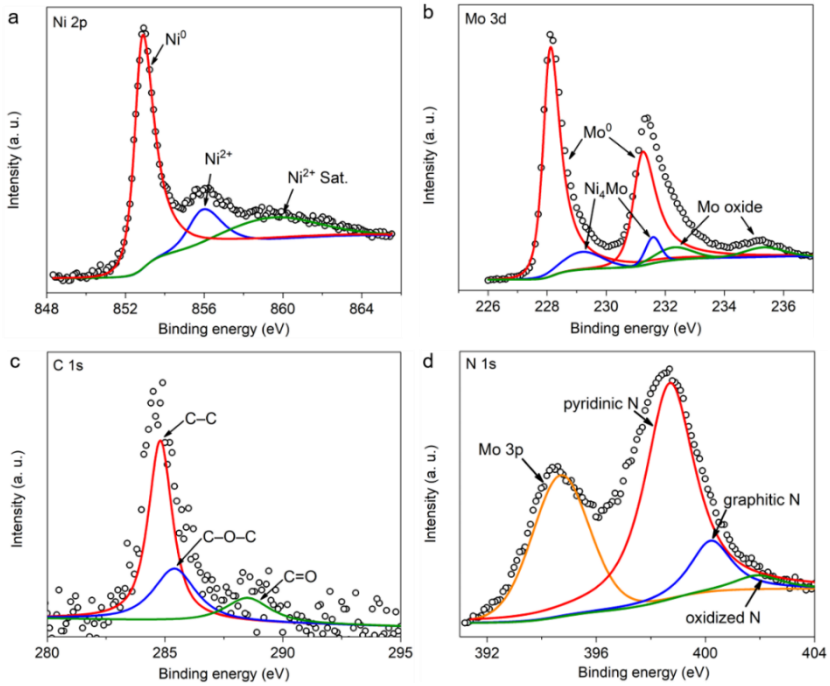

Figure 4.6 High-resolution XPS spectra of graphene-encapsulated NiMo catalysts. (a) Ni 2p, (b) Mo 3d, (c) C 1s, and (d) N 1s spectra. Copyright 2018 American Chemical Society.

4.3 Electrochemical measurements

The HER performances of the graphene-encapsulated NiMo catalysts were investigated in 0.5 M H_2SO_4 electrolyte in a three-electrode system. The polarization curves of graphene-encapsulated NiMo catalysts were compared to those of commercial 10 wt.% Pt/C, bare NiMo alloy without graphene encapsulation, and 3DNG substrate (**Figure 4.7a**). Notably, 3DNG showed the lowest HER performance with a negligible current density in comparison to other graphene-encapsulated NiMo catalysts, which indicates the HER activity mainly originates from the encapsulated NiMoNPs instead of the 3DNG substrate. The 10 wt.% Pt/C, bare porous NiMo alloy, 1−2NGL, 1−2GL, 3NGL, and 6−7NGL exhibited an electrode potential (η_{10}) of 70, 27, 66, 84, 80, and 109 mV (vs. RHE), respectively, to reach the current density of 10 mA cm^{-2} (**Figure 4.7b**). Additionally, the turnover frequencies (TOF) values are shown in **Figure 4.7c**. The TOF values were estimated as 0.63, 0.26, 0.21, and 0.10 H_2 s^{-1} for the bare porous NiMo alloy, 1−2NGL, 3NGL, and 6−7NGL, respectively. The experimental results indicate that the HER performance decreases with increasing the number of encapsulating graphene layers, which could be attributed to the blocking of catalytic sites on NiMo surface.

For graphene-encapsulated NiMo catalysts, the HER mechanism was determined from the Tafel plots of the polarization curves (**Figure 4.7d**). The Tafel slope value was 34, 35, 57, 61, 60, 64, and 160 mV per decade observed for the 10 wt.% Pt/C, bare porous NiMo alloy, 1−2NGL, 1−2GL, 3NGL, 6−7NGL, and 3DNG substrate, respectively. These values demonstrate the occurrence of the Volmer−Heyrovsky process[138, 139] for graphene-encapsulated NiMo catalysts in 0.5 M H_2SO_4 electrolyte.

The Electrochemical impedance spectroscopy was used to measure the charge transfer kinetics. The Nyquist plots and corresponding equivalent circuit model are exhibited in **Figures 4.8a** and **4.8b**. The Nyquist plots exhibited a semi-circular arc in the frequency ranged from 100 kHz to 0.1 Hz, and the equivalent circuit model comprises R_s, R_{ct}, and constant phase element (CPE). The intercept of the horizontal axis in the high-frequency region is considered as the equivalent series resistance, R_s, which represents the electrolyte resistance and the intrinsic resistance of two electrodes. The R_s values were around 3 **Ω**, indicating a good contact in this electrochemical system. The diameter of the semi-circular arc represents the charge transfer resistance, R_{ct}, which is related to the ion transfer between the electrolyte and the electrodes. The R_{ct} value was 5.8, 8.1, and 10.2 **Ω** for the 1−2NGL, 3NGL, and 6−7NGL, respectively. The low R_{ct} value reveals a fast ion transfer speed, which is beneficial to accelerate the HER kinetics. The CPE is related to the capacitance in the interface between the electrolyte and the electrodes.

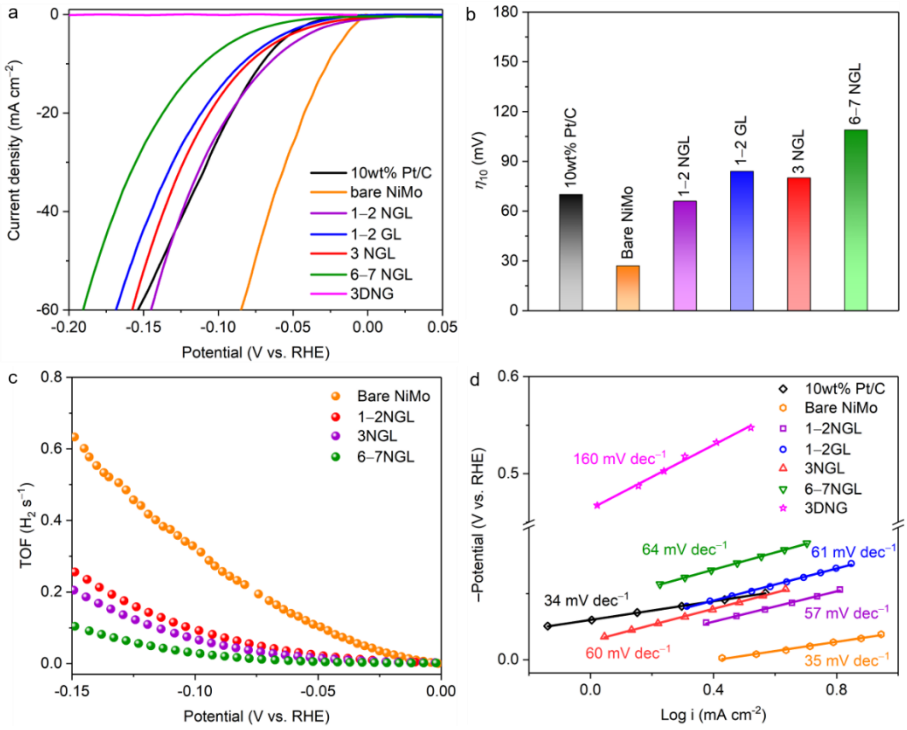

Figure 4.7 Electrochemical measurements. (a) HER polarization curves and (d) Tafel plots of 1−2GL, 1−2NGL, 3NGL, 6−7NGL, bare porous NiMo (without graphene encapsulation), and commercial 10 wt% Pt/C catalysts. (b) The η_{10} values for various catalysts. (c) Calculated TOF values for bara porous NiMo, 1−2NGL, 3NGL, and 6−7NGL catalysts.

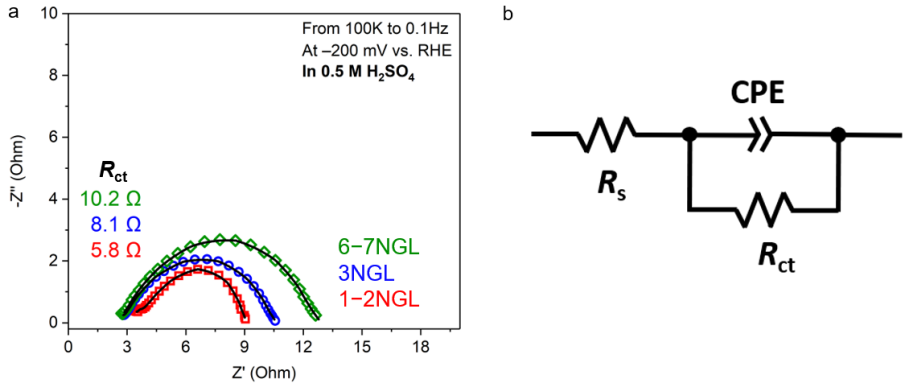

Figure 4.8 Electrochemical impedance spectroscopy. (a) Nyquist plots and (b) equivalent circuit model of 1−2NGL, 3NGL, and 6−7NGL catalysts at the electrode potential of –200 mV vs. RHE in 0.5 M H_2SO_4 in a three-electrode system.

The long-term retention of electrocatalytic activity was further examined. Although the bare porous NiMo (without graphene encapsulation) exhibited the outstanding initial HER performance (**Figure 4.9a**), the corresponding current density became very small after 1000 CV cycles testing due to the severe catalyst dissolution in 0.5 M H_2SO_4 electrolyte. In contrast, the η_{10} values of bare porous NiMo, 1–2GL, 1–2NGL, 3NGL, and 6–7NGL catalysts after 1000 CV cycles test increased by 830%, 20%, 70%, 13%, and 1%,

respectively (**Figure 4.9b**). Thus, with increasing NGL number, the acid resistance of catalysts drastically improved, but the initial HER performances reduced.

Furthermore, the chemical leaching of catalysts after the cycling tests were measured by ICP–OES. A severe metal dissolution was observed for 1–2NGL catalyst after 1000 CV cycles testing, i.e., 48 atomic percentage (at. %) for Ni and 17 at. % for Mo (**Figures 4.9c** and **4.9d**), while the 3NGL and 6–7NGL catalysts showed low dissolution rates of 4/1.5 at. % and 2/0.3 at. % for Ni and Mo. In addition, the NiMo catalysts with thin graphene layers exhibited high catalytic activities, whereas thick encapsulating graphene layers resulted in low dissolution rates (i.e., high corrosion resistance). The 3NGL catalyst exhibited an ideal balance between corrosion resistance and HER activity (**Figure 4.9c**).

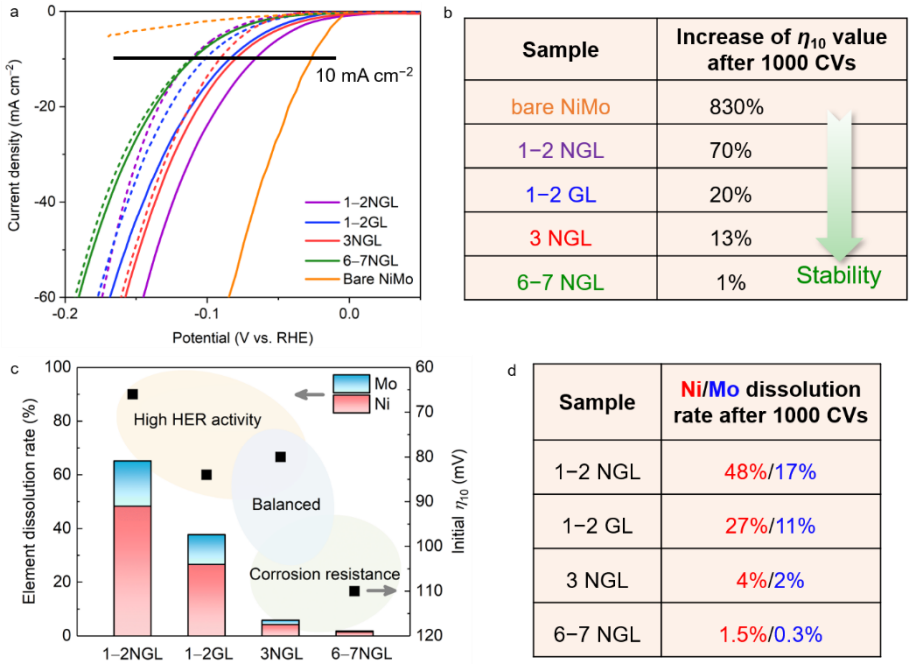

Figure 4.9 Stability tests. (a) The HER polarization curves of 1–2GL, 1–2NGL, 3NGL, 6–7NGL, and bare porous NiMo (without graphene encapsulation) in 0.5 M H_2SO_4 electrolyte. The solid and dashed curves represent HER performances before and after 1000 CV cycles testing. (b) The increase of η_{10} values after 1000 CV cycles testing. (c) Ni and Mo dissolution rates in encapsulated NiMo catalysts after 1000 CV cycles testing. The dissolution rates are average values of three individual experiments. The η_{10} values were obtained from the initial polarization curves. (d) Ni and Mo dissolution rates.

Long-term catalyst durability was examined by CA at −150 mV vs. RHE for 25 h in 0.5 M H_2SO_4 (**Figure 4.10**). The 1–2NGL catalyst retained only 51.1% of its initial current density, whereas the current of the 6–7NGL catalyst maintained >99% of its initial value. The 3NGL catalyst displayed a current density of ~44 mA cm^{-2} (92.5% of initial), which continued for 25 h with a low rate of leaching. CA testing further confirms that the number of graphene layers is important to determine the balance between corrosion

resistance and catalytic activity.

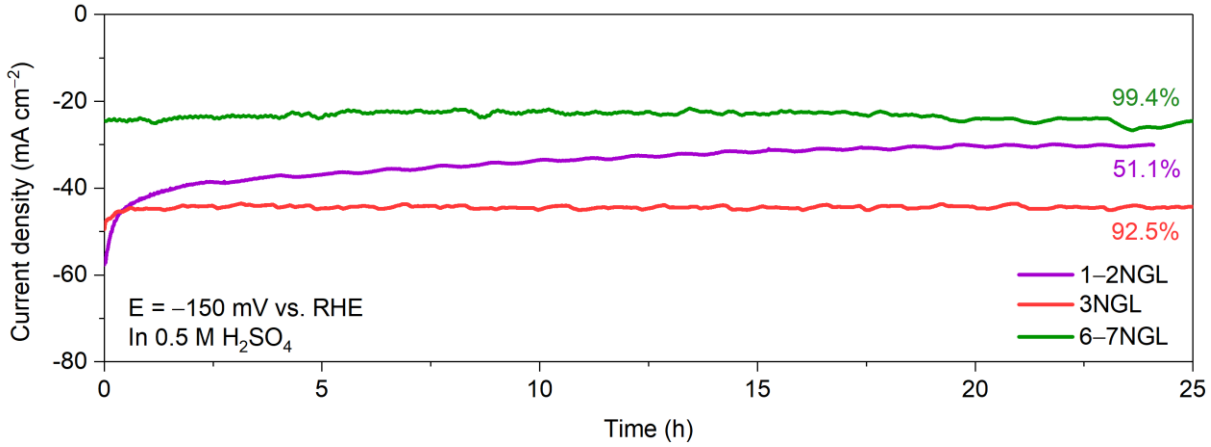

Figure 4.10 Long-term catalyst durability. CA measurements were carried out at −150 mV vs. RHE for 25 h in 0.5 M H_2SO_4 in a three-electrode system.

To understand the HER activity−catalyst structure relationship, we elucidated the origin of the protective effect of the encapsulating graphene layers. Raman spectra, XRD patterns, and XPS spectra of the graphene-encapsulated NiMo catalysts after 1000 CV cycles testing confirmed that the initial characteristics of graphene layers, catalyst composition, and surface chemical states were mainly retained (**Figures 4.11** and **4.12**). However, N-doped graphene layers were slightly oxidized due to surface redox processes during the HER test. Importantly, the encapsulating graphene layers prevented Ni and Mo oxidation, and the graphene characteristics of graphene-encapsulated NiMo catalysts (I_D/I_G = 0.55−0.60) were well preserved, in line with the XPS results.

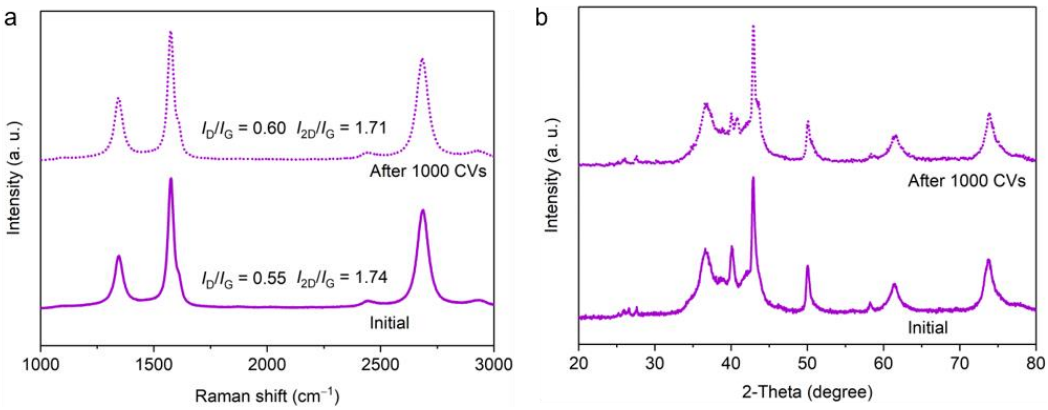

Figure 4.11 Raman and XRD characterizations before (solid curves) and after (dashed curves) 1000 CV cycles testing. (a) Raman spectra and (b) XRD patterns.

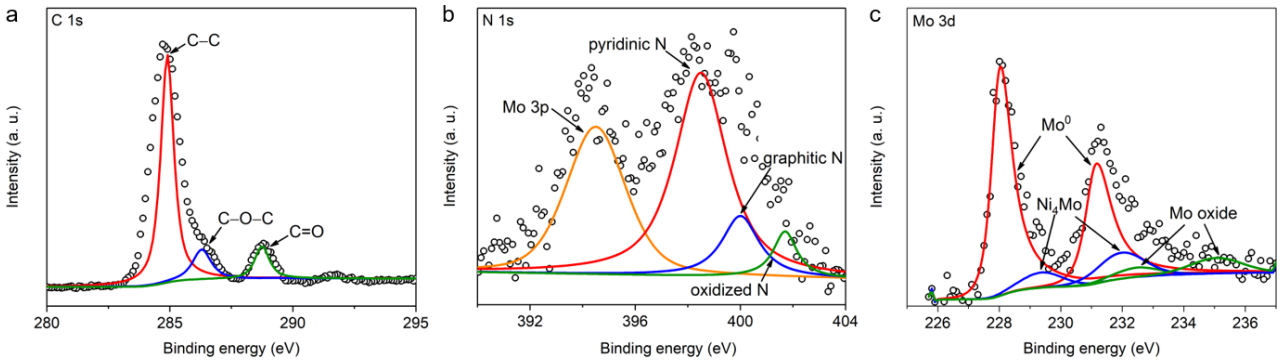

Figure 4.12 High-resolution XPS spectra of graphene-encapsulated NiMo catalysts after 1000 CV cycles testing. (a) C 1s, (b) N 1s, and (c) Mo 3d spectra. XPS Ni spectra cannot be detected due to the overlap of F KLL from Nafion. Copyright 2018 American Chemical Society.

4.4 DFT calculations

The influence of the NGL number on the catalytic activity was further investigated by DFT calculations using the PBE+D3(BJ) theory[116, 117, 118] under periodic boundary conditions, with initial coordinates of bare NiMo(100) and NiMo(100) encapsulated by 1, 3, and 5 NGLs (NiMo/1NGL, NiMo/3NGL, and NiMo/5NGL). The overall HER mechanism in acidic media was thought to involve an initial stage ($H^+ + e^- \rightarrow H^*$), an intermediate stage (H* adsorption), and a final stage (generation of 0.5 H_2)[28, 140]. Herein, HER activity was evaluated based on the Gibbs free energies for H* adsorption, $|\Delta G_{H^*}|$,[22] which are summarized in **Figure 4.13a** (further computational details are given in Experimental Section). The models of bare NiMo(100), NiMo/1NGL, NiMo/3NGL, and NiMo/5NGL for DFT calculations are illustrated in **Figure 4.13b**. Positive ΔG_{H^*} values were observed for a free-standing non-doped pure graphene, pyridinic nitrogen (pN)-doped graphene, and NiMo(100) encapsulated by a monolayer non-doped graphene (NiMo/1GL). In contrast, a large negative ΔG_{H^*} value was observed for graphitic nitrogen (gN)-doped graphene. The $|\Delta G_{H^*}|$ value for NiMo(100) (0.11 eV) was similar to that of a highly efficient Pt catalyst (0.08 eV), indicating that NiMo(100) showed the best HER performance among the studied materials, in agreement with our experimental results and reported data[45]. Moreover, models of N-doped graphene with 1, 3, and 5 layers distributed over the NiMo(100) surface exhibited $|\Delta G_{H^*}|$ values of 0.16, 0.37, and 0.38 eV, respectively, which were comparable to state-of-the-art MoS_2 catalysts (−0.36 to +0.39 eV)[141]. Importantly, as the NGL number increased, the $|\Delta G_{H^*}|$ value and its deviation from the above-mentioned Pt value (0.08 eV) increased, in agreement with the experimentally determined order of HER activities (**Figure 4.7a**). In addition, the $|\Delta G_{H^*}|$ value of the 3DNG substrate including pN- and gN-doped graphene was much higher (0.68 and 0.54 eV, respectively) than that of the graphene-encapsulated NiMo catalysts, indicating the poor HER activity.

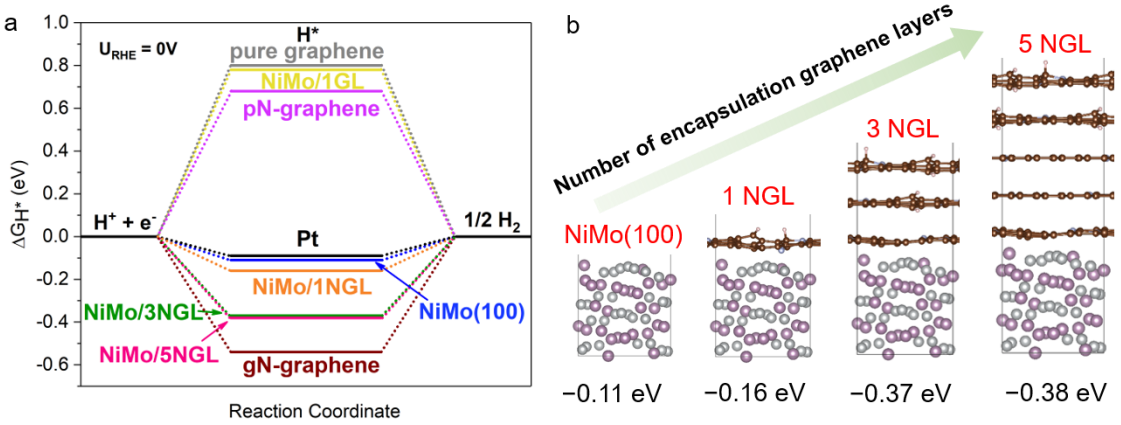

Figure 4.13 Gibbs free energies of H adsorption. (a) ΔG_{H^*} values for NiMo/1NGL, NiMo/3NGL, NiMo/5NGL, NiMo/1GL, bare NiMo(100), a non-doped pure graphene sheet, and N-doped graphene sheets (graphitic N doping, gN; pyridinic N doping, pN). (b) The models employed for DFT calculations. The numbers under those models are the corresponding values of Gibbs free energies of H adsorption. The white, violet, brown, light blue, and pink spheres represent Ni, Mo, C, N, and H atom, respectively. Copyright 2018 American Chemical Society.

Establishing the agreement between DFT calculations and experimental data, we investigated the charge distribution of NGLs on the NiMo(100) surface (**Figure 4.14**). The data indicated that an NGL shows strong contrast with positively/negatively charged parts (at most −1.2 e and +0.9 e on N and C atoms, respectively; **Figures 4.14** and **4.15** and **Table 4.1**). The partial imparity in the positive and negative charge distribution on the NGLs boosted the HER process[142]. The presence of N dopants on each NGL improved ΔG_{H^*} and simultaneously promoted charge density redistribution around the NGL to form electron accumulation areas, thus facilitating H* adsorption/desorption during electrochemical hydrogen production. The NiMo substrate influenced the total layer-by-layer overall charge balance on the NGLs: the 1st, 3rd, and 5th NGLs exhibited values of −1.48 e, +0.033 e, and +0.014 e, respectively, and electron/hole doping on the NGLs could enhance electrical conductivity/mobility, contributing to HER performance[38]. This DFT prediction was confirmed by XPS experimental results (**Table 4.2**). The Ni^0 and Mo^0 peaks of 1−2NGL and 3NGL catalysts experienced a positive shift in comparison to the bare NiMo alloy (without graphene encapsulation). These peak shifts indicate that the electron transfer from the NiMo alloy substrate to encapsulating graphene layers, resulting in electron accumulations (negatively charging) on NGLs. Indeed, the C 1s sp^2 peak of the 1−2NGL catalyst tended to show a slight negative shift in comparison to that of the 3NGL catalyst. These XPS experimental results are in line with our DFT calculations of the 1st graphene layer near NiMo substrate being negatively charged. As such, NiMo substrates affected both the ΔG_{H^*} value and the charge balance of the encapsulating graphene layers.

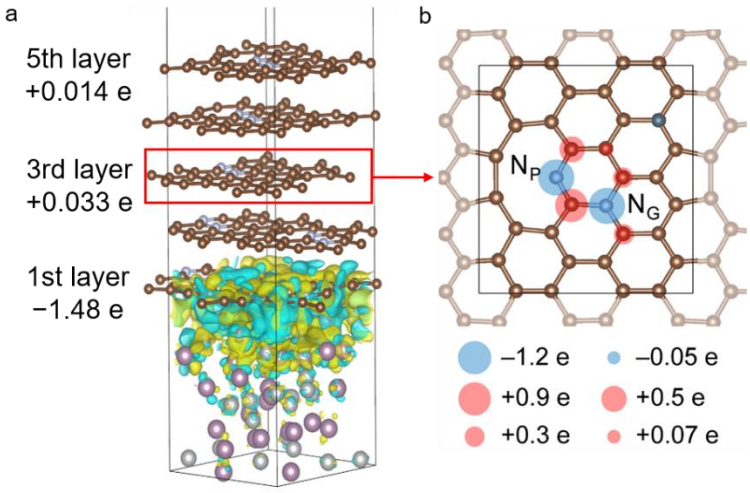

Figure 4.14 DFT-calculated charge distribution. (a) Charge density difference for NiMo(100) encapsulated by five NGLs, with total charges of the 1st, 3rd, and 5th NGLs on NiMo(100). Yellow and cyan areas represent electron accumulation and depletion. (b) Partial charges of the 3rd NGL in the NiMo/5NGL model. The box represents the unit cell boundary. Copyright 2018 American Chemical Society.

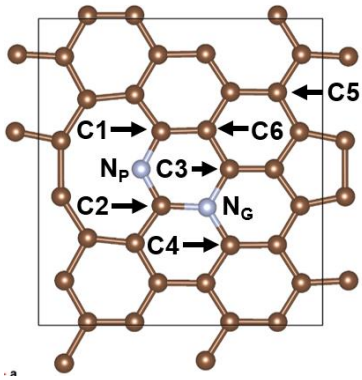

Figure 4.15 Top view of a N-doped graphene sheet with named different types of N and C atoms. Charge populations on each atom in various encapsulation situation were summarized in **Table 4.1**. Copyright 2018 American Chemical Society.

Table 4.1 Typical charge distributions on different types of N and C atoms in a free-standing NGL and N-doped graphene layers on NiMo(100) surface.

	N_P	N_G	C1	C2	C3	C4	C5	C6
1 free-standing NGL	−1.24	−1.15	+0.47	+0.90	+0.29	+0.25	−0.05	+0.07
1st NGL on NiMo (100)	−1.22	−1.14	+0.52	+0.96	+0.28	+0.38	−0.13	+0.15
3rd NGL on NiMo (100)	−1.23	−1.15	+0.44	+0.90	+0.28	+0.27	−0.03	+0.08
5th NGL on NiMo (100)	−1.24	−1.16	+0.44	+0.89	+0.29	+0.25	−0.05	+0.07

Note: The unit is e. The N-doped graphene layer model is shown in **Figure 4.15**.

Table 4.2 XPS peak positions of 1−2NGL, 3NGL, and bare NiMo alloy catalysts.

Catalyst	Mo^0 (eV)	Ni^0 (eV)	Sp^2 peak (C 1s) (eV)
1−2NGL	228.05; 231.18	852.82	284.73
3NGL	228.14; 231.26	852.86	284.79
Bare NiMo alloy (without graphene encapsulation)	227.80; 230.94	852.70	–

The HER performance and chemical stability of the graphene-encapsulated NiMo alloy catalysts strongly depends on the the number of encapsulating graphene layers and the NiMo substrate. DFT calculations suggested that the N-doped graphene/NiMo system showed an improved Gibbs free energy for H* adsorption compared to that for free-standing N-doped graphene sheets (**Figure 4.13a**) due to the strong influence of the NiMo substrate on the encapsulating graphene layers, in agreement with the experimental results. This influence became weaker with increase of the number of graphene layers and was not obviously observed after the third layer. The disruption of the total charge balance on the encapsulating graphene layers induced by the NiMo substrate and the bicontinuous porous conductive graphene networks with open pore channels enhance the electron transport.

4.5 Conclusions

In summary, the graphene-encapsulated NiMo alloy nanoparticles on 3D porous graphene substrate was successfully synthesized. The number of encapsulating graphene layers was precisely controlled by tuning the CVD deposition time. The influence of the number of graphene layers on HER activity and chemical stability in an acidic electrolyte was experimentally investigated for graphene-encapsulated NiMo catalysts. Experimental results and DFT calculations suggested that the number of encapsulating graphene layer plays a significant role in HER performance, chemical durability of encapsulated catalysts, and charge distribution on graphene. The results showed that NiMo nanoparticles encapsulated by 3 layers N-doped graphene afforded the excellent balance between corrosion resistance and catalytic activity. For instance, the 3NGL catalyst exhibited a low potential of 80 mV to reach a current density of 10 mV cm^{-2} and a small Tafel slope value of 60 mV dec^{-1}; in addition, more than 92% of initial current density was retained for 25 h in 0.5 M H_2SO_4, which confirms the remarkable acidic resistance. The described graphene encapsulation technique provides a new direction for exploiting low-cost, non-noble-metal catalysts in acidic electrolytes for efficient hydrogen production.

Chapter 5 Proton penetration through graphene layers

In order to reveal the HER mechanism of graphene-encapsulated NiMo catalysts in acidic electrolytes, the proton penetration behaviour through non-doped and N-doped graphene with various layer numbers were systematically investigated. The current−voltage ($I-V$) characteristics and CA tests were measured to study the resistance of proton penetration as a function of the number of graphene layers. The energy barrier of proton penetration was calculated by DFT. Base on the experimental results and DFT calculations, the HER mechanism of graphene-encapsulated non-noble-metal catalysts has been proposed to achieve a thorough understanding of distinct HER processes determined by the encapsulating graphene layers.

5.1 Fabrication of the experimental device

The non-doped graphene and N-doped graphene layers were employed as separating membranes in the device (**Figure 5.1a**). The glass separator with a window-attached Si_3N_4 chip (window size: 10 μm × 10 μm) fixed in the center was employed to obtain two individual anode and cathode chambers which were filled with 0.5 M H_2SO_4 electrolyte. The distance between the electrode and the separator is 1.0 cm. Monolayer non-doped or N-doped graphene was stacked layer-by-layer with protective Nafion sheets (proton conductivity: ~90 mS cm^{-1} at room temperature)[143] on both outmost sides[144] (**Figure 5.1b**). Nafion acts as a protective sheet for graphene layers with high proton conductivity, chemical/electrochemical stability, and extremely low electron conductivity[145]. All the connection places and gaps were sealed by acid-stable and ion-impenetrable gasket to ensure that protons can only pass across the graphene membrane. The Nafion/graphene layers/Nafion sandwich membrane was set on the window area of the Si_3N_4 chip (**Figures 5.1c** and **5.2**).

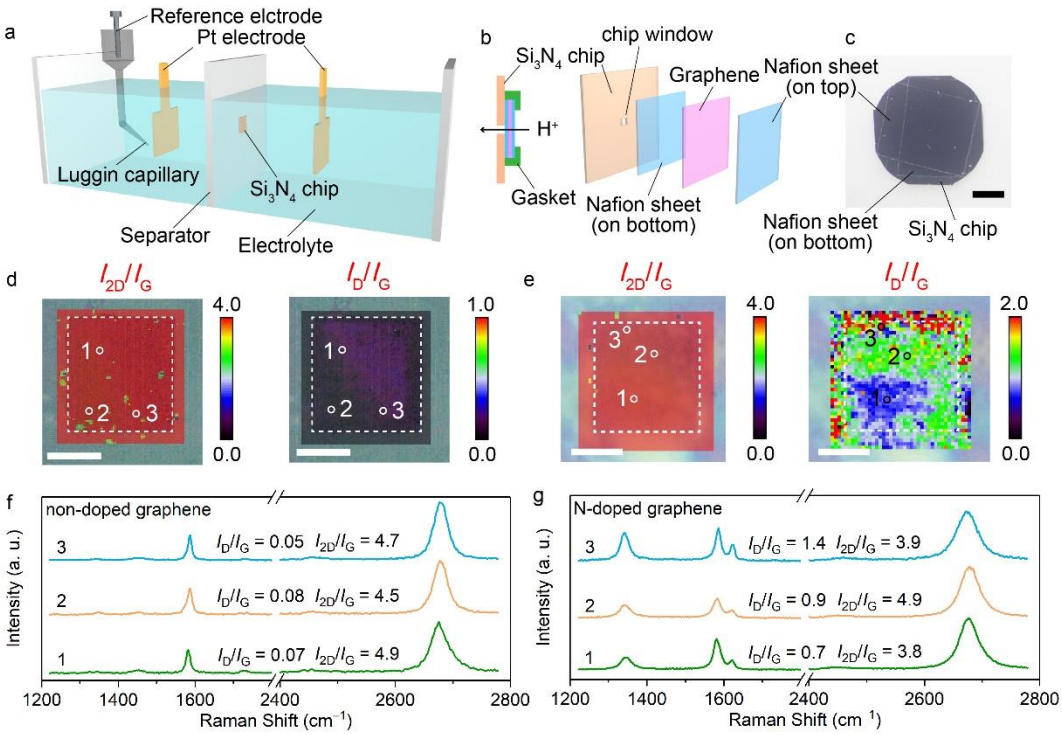

Figure 5.1 Device fabrications and characterization of graphene membranes. (a) The schematic of the experimental device. (b) The membrane with sandwich stacking of Nafion/Graphene layers/Nafion is set on the window area of a Si_3N_4 chip. (c) The optical photo of the Si_3N_4 chip with attached Nafion/Graphene layers/Nafion membrane. The Raman maps of monolayer (d) non-doped and (e) N-doped graphene in the chip window area. The dot square represents the window area. (f, g) The corresponding collected Raman spectra from the pointed positions in the maps. Scale bar: (c) 1 mm; (d, e) 5 μm.

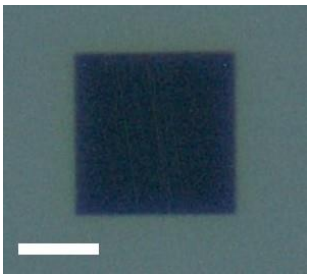

Figure 5.2 The optical photo of the window area in a pristine Si_3N_4 chip. Scale bar: 5 μm.

5.2 Structural characterizations of graphene membranes

The graphene membranes were characterized by Raman spectroscopy, which allows us to quantitatively identify the features of graphene sheets, such as the layer number and the defect density. The Raman maps of the monolayer non-doped and N-doped graphene in the window area of Si_3N_4 chip (**Figures 5.1d**–**5.1g**, **5.3** and **Table 5.1**) demonstrated high intensity ratios of 2D band and G band (I_{2D}/I_G: 3.8–4.9), which is indicative of high quality monolayer graphene[146, 147] (**Figures 5.1f** and **5.1g**). From the calculated rate of the number of graphene layer shown in **Table 5.1**, the monolayer graphene area ("Red" area in I_{2D}/I_G Raman map) is more than 98%. Moreover, the defect degree in graphene layers at micro-scale levels was quantified by measuring the D band to G band intensity ratios (I_D/I_G)[148]. The Raman map of the non-doped graphene membrane showed low I_D/I_G values (0.05–0.08), which is ascribed to the intrinsic defects in graphene lattices. The relatively high intensity ratios (I_D/I_G: 0.7–1.4) were exhibited in the Raman map of N-doped graphene membrane. This indicates that the large number of topological defects induced by the N dopants in the sp^2 carbon matrixes. Importantly, characteristics of pinholes or breaks in Nafion-protected graphene membrane were not observed during both fabrication processes of separating membranes and Raman measurements (**Figure 5.4**). The characterizations of bilayer and trilayer non-doped and N-doped graphene membranes in the chip window areas were similarly investigated (**Figures 5.5** and **5.6**).

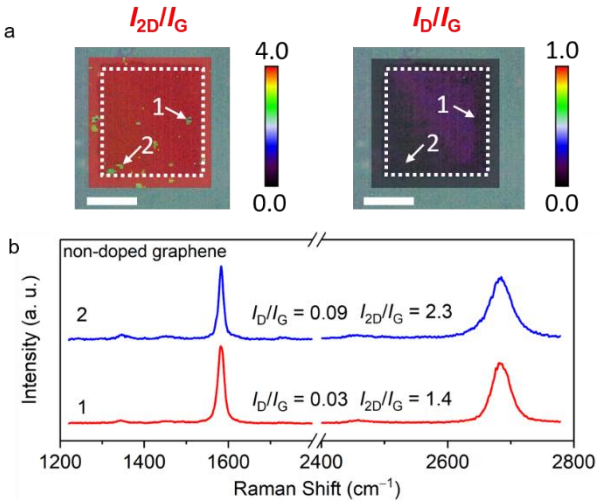

Figure 5.3 Raman characterization of monolayer non-doped graphene. (a) Raman map of monolayer non-doped graphene on the window area of Si_3N_4 chip. The dot square indicates the window area. Scale bar: 5 μm. (b) The corresponding Raman spectra in spot 1 (blue area in I_{2D}/I_G image) and spot 2 (yellow area in I_{2D}/I_G image) were collected in the map image. The I_{2D}/I_G values confirm that 2–3 layers graphene are mainly grown in "yellow" and "blue" areas. The rates of different color areas are summarized in supplementary **Table 5.1**. The monolayer graphene area ("red" area in I_{2D}/I_G image) exceeds 98% in the chip window region.

Table 5.1 The rates of “red”, “yellow” (spot 2), and “blue” (spot 1) areas in I_{2D}/I_G Raman map (**Figure 5.1d**) of monolayer non-doped graphene membrane.

Area （in I_{2D}/I_G image）	**Layer Number**	**Rate (%)**
Red	Monolayer	98.1
Yellow (spot 2) and Blue (spot 1)	Bi- or tri-layer	1.9

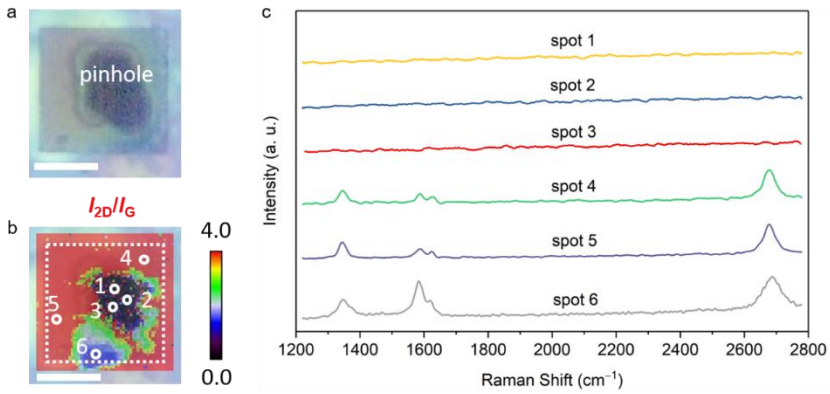

Figure 5.4 Raman characterization of N-doped graphene membrane with a pinhole. (a) The optical photo of a graphene membrane with a pinhole in the center. The pinhole was made by using high energy laser. (b) The corresponding Raman map. Scale bar: (a, b) 5 μm. (c) Raman spectra collected from pointed six spots on the graphene membrane. The Raman spectra from the pinhole area (spots 1−3) show no graphene characteristic, while we can see specific Raman spectra of N-doped graphene from other spots.

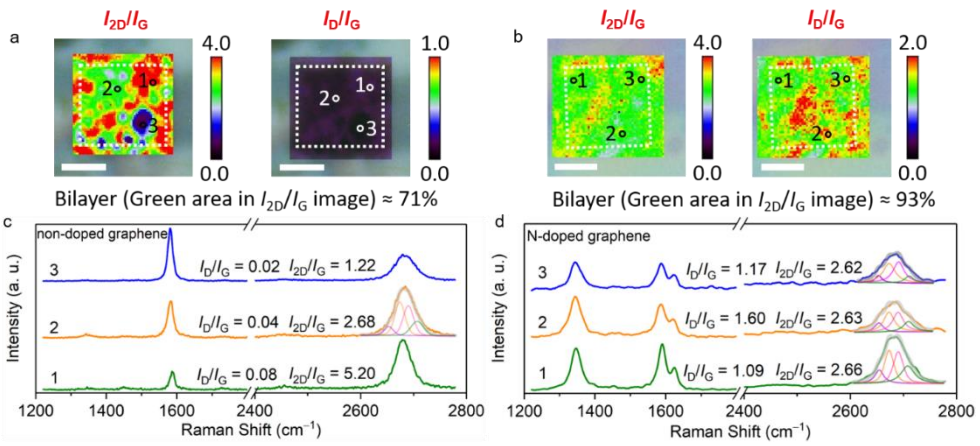

Figure 5.5 Raman characterization of bilayer graphene membrane. Raman maps of bilayer (a) non-doped and (b) N-doped graphene on the window area in Si_3N_4 chip. Scale bar: (a, b) 5 μm. (c, d) The corresponding collected Raman spectra of the pointed positions in the maps. Lorentzian fitting analyses of the 2D bands indicates four deconvoluted spectrum for bilayer graphene characteristics. The "red" (spot 1 in I_{2D}/I_G image), "green" (spot 2 in I_{2D}/I_G image), and "blue" (spot 3 in I_{2D}/I_G image) area represent mono-, bi-, and tri-layer graphene, respectively. The calculated rates of bilayer area (green area in I_{2D}/I_G image) were 71% and 93% for non- and N-doped graphene membranes on the chip window region, respectively.

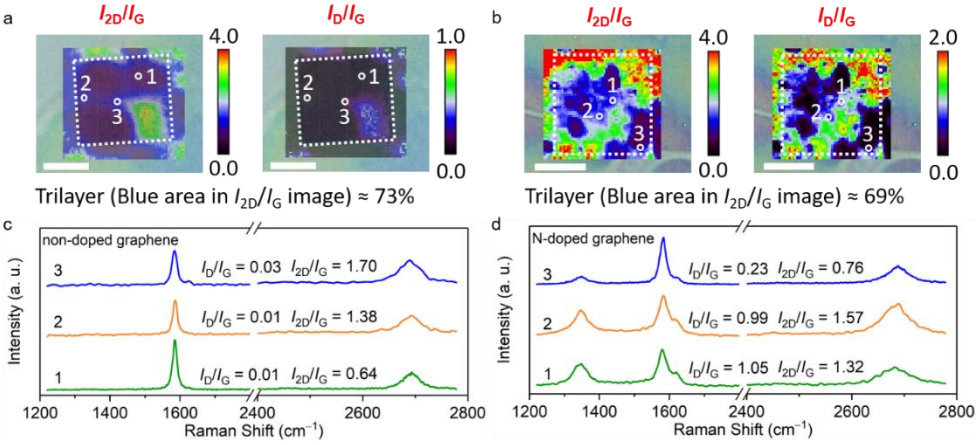

Figure 5.6 Raman characterization of trilayer graphene membrane. Raman maps of trilayer (a) non-doped and (b) N-doped graphene on the window area in Si_3N_4 chip. Scale bar: (a, b) 5 μm. (c, d) The corresponding collected Raman spectra of the pointed positions in the maps. The calculated rate of trilayer area is 73% and 69% for non-doped and N-doped graphene, respectively.

The atomic structure of non-doped and N-doped graphene with various layer numbers were observed by high-resolution transmission electron microscopy (HRTEM). The HRTEM image of monolayer non-doped graphene (**Figure 5.7a**) showed a honeycomb structure consists of six carbon atoms with six-fold symmetry spots belonging to monolayer graphene. The bi- and tri-layer non-doped graphene presented misorientated six-fold symmetry spots, i.e., 12 spots for bilayer and 18 spots for trilayer (insets of **Figures**

5.7b and **5.7c**)[149, 150]. Note that the HRTEM images of N-doped graphene showed various types of topological defects induced by N doping (**Figures 5.7d** and **5.7e**), which were also observed in other report[151]. Furthermore, the chemical binding state of graphene sheets were investigated by XPS (**Figure 5.7f**). The C 1s XPS spectra of non-doped and N-doped graphene exhibited the high quality of graphene without obvious oxidations. The N 1s XPS spectrum of N-doped graphene revealed that the N dopants are in the forms of pyridinic (0.18 at.%), graphitic (0.76 at.%), and oxidic structures (0.36 at.%)[121, 137]. Very tiny amounts of residual Cu metal (⩽0.01 at.%) on graphene sheets were observed (**Figure 5.8**).

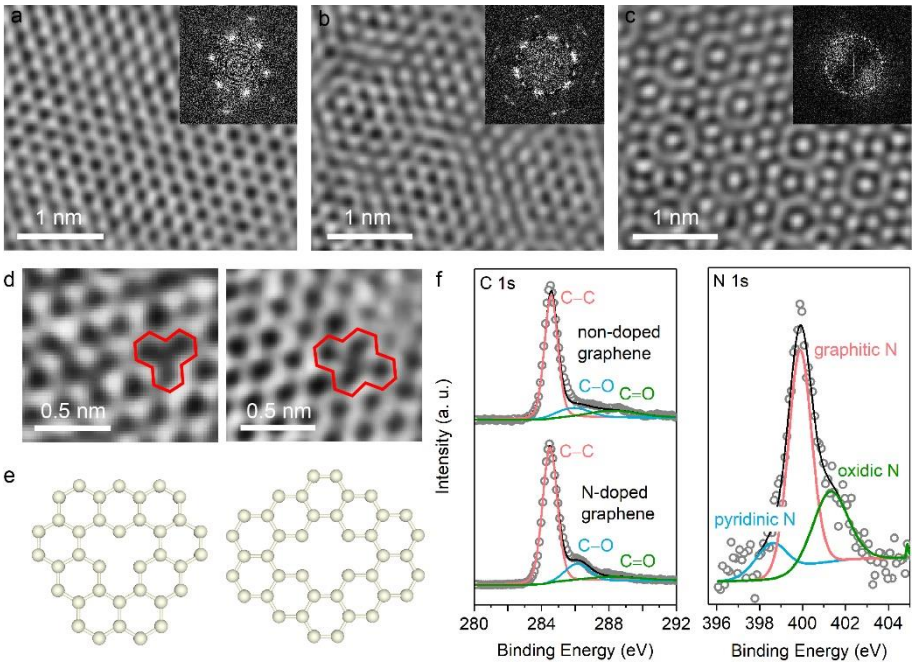

Figure 5.7 Atomic graphene-layer characterization. (a–c) HRTEM images of monolayer, bilayer, and trilayer non-doped graphene and the corresponding Fast Fourier Transform (FFT) images. (d) Two types of defect (single and double vacancies) observed in N-doped graphene lattices and (e) the corresponding atomic models. (f) High-resolution XPS C 1s spectra of non-doped and N-doped graphene; XPS N 1s spectrum of N-doped graphene.

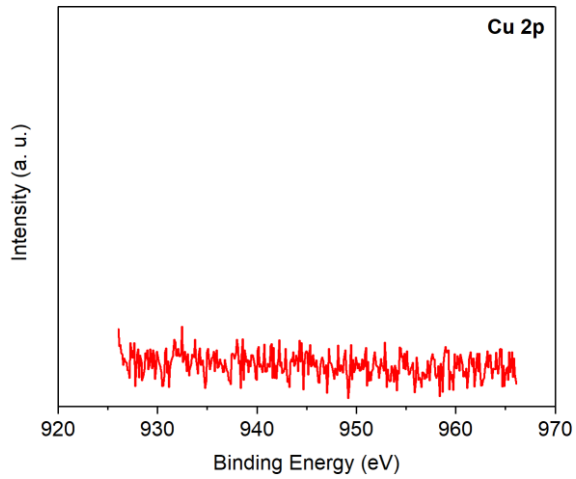

Figure 5.8 High-resolution XPS Cu 2p spectrum of graphene sample. The residual Cu concentration on graphene is less than 0.01 at.%.

5.3 Operational check for the H-type cell

We used the fabricated H-type cell to examine proton penetration pathway through graphene layers by measuring the open circuit potential (E_{OC}) between the two physically separated chambers in the H-type cell (**Figure 5.9a**). The device using monolayer graphene membrane as a separator can yield a stable open circuit potential (E_{OC}) with keeping at 71 mV for 6 h (**Figure 5.9b**), when one side of the membrane was exposed to electrolyte in pH 1.74 (0.05 M H_2SO_4 + 0.45 M Na_2SO_4) and another side to one in pH 0.50 (0.5 M H_2SO_4), respectively. This measured value is consistent with the theoretical potential (73 mV, calculation details in experimental section 2.3.2) as calculated from the Nernst equation, which verifies that a proton penetration pathway exists and that the electrolyte does not leak.

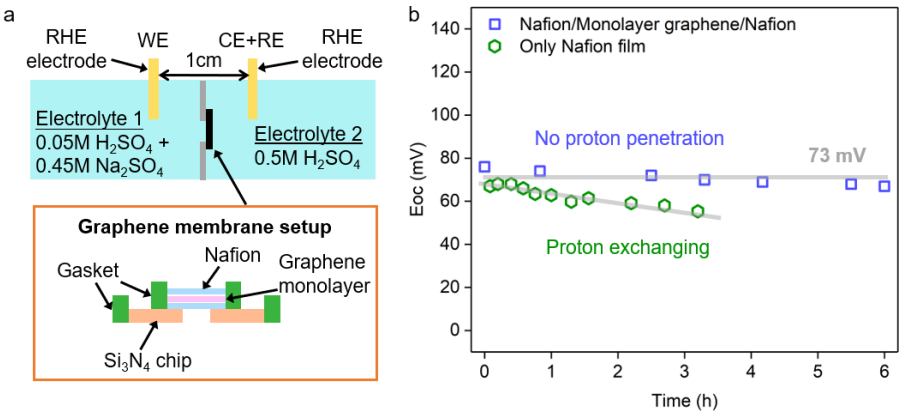

Figure 5.9 Operational check for the H-type cell. (a) Configuration of experimental setting. The monolayer graphene membrane was used to separate two electrolytes with different pH values. Two reversible hydrogen electrodes (RHE) were used as cathode and anode in this two-electrode system. The measured pH values of electrolyte in cathode side and anode side were 1.74 and 0.50, respectively. (b) Measurement of open circuit potential (E_{oc}). In the monolayer graphene membrane case, the E_{oc} value between the separated chambers ranged from 76 mV to 67 mV (average value: 71 mV) in 6 h, which is very close to the value of 73 mV calculated by the Nernst equation (Calculation details are in Supplementary Methods). In only Nafion membrane (sheet thickness: 170 μm) case, the E_{oc} values showed a declining trend, indicating that the protons penetrate through the Nafion sheet under the proton concentration difference.

5.4 Electrochemical proton-penetration experiments

The proton penetration through non-doped and N-doped graphene with varied layer numbers, i.e., mono-, bi-, tri-, and tetra-layers, was investigated by measuring the current–voltage (*I–V*) characteristics. With the bias voltage, ranging from +200 mV to –200 mV, applied between two Pt plate (1.0 cm × 1.0 cm) electrodes in a two-electrode system, the detected proton current varied linearly (**Figures 5.10a** and **5.11**). The declining proton current was observed with the increasing number of graphene layers. Additionally, the N-doped graphene resulted in relatively larger proton current in comparison to non-doped graphene under the same layer number, which may derive from the rich defects in N-doped graphene lattices.

The areal proton conductivity was calculated through equation $\sigma=S/A$, where S is conductivity and A is the area of the window in Si_3N_4 chip. The conductivity $S=I/V$, where the proton current I and bias voltage V were collected from the $I-V$ characteristics (**Figure 5.10a**). The areal proton conductivity was estimated as 0.27 mS cm^{-2} for monolayer non-doped graphene and 0.44 mS cm^{-2} for monolayer N-doped graphene (**Figure 5.10b**). The proton conductivity exhibits a declining trend with the increasing of the number of graphene layers, which confirms that the number of graphene layers significantly affects the resistance for proton penetration. The S value was 43 mS cm^{-2} when only the Nafion sheet as the separating membrane, which is much larger than the values in the cases of graphene layers as the separating membrane. This result confirms that the resistance of proton penetration mainly originates from the graphene layers instead of the Nafion sheet.

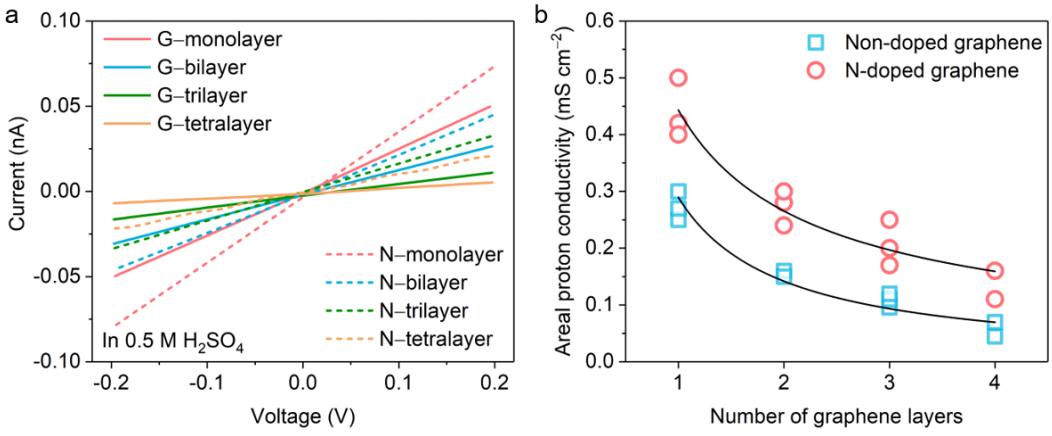

Figure 5.10 *I–V* characteristics and proton conductivity. (a) *I–V* characteristics of proton penetration through non-doped and N-doped graphene with various layer numbers. The top insets are the schematic illustration of proton penetration through graphene layers and non-doped graphene lattice. The bottom inset is the N-doped graphene lattice. The solid and dash curve represents the proton current observed through non-doped and N-doped graphene membranes, respectively. (b) Layer number dependences of proton conductivity for non-doped and N-doped graphene layers. Each square or circle represents the data from one single test.

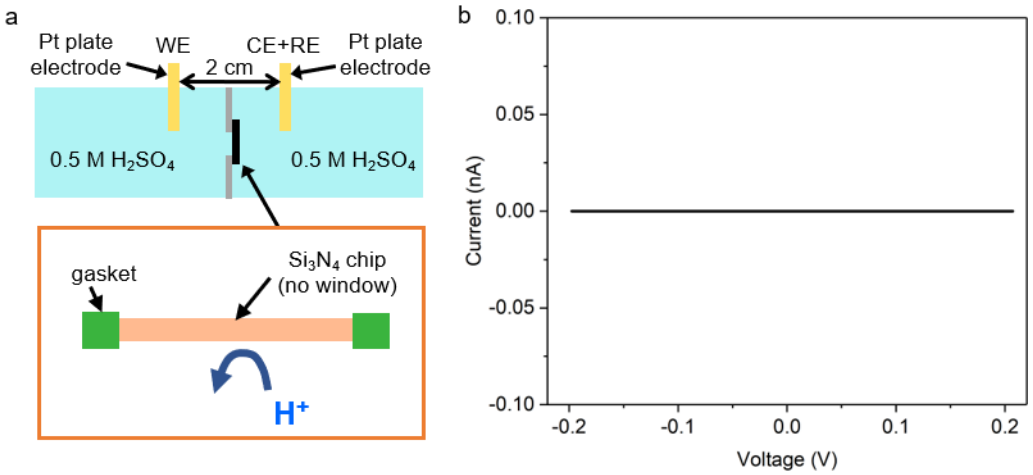

Figure 5.11 *I*–*V* characteristics when a Si_3N_4 chip without the central window set as the separating membrane. (a) The configuration of the experimental device and the separating membrane. (b) The *I*–*V* characteristics. This result confirms that there is no apparent current when no proton penetrates.

The Nyquist plot of graphene membranes exhibited a semiarc in the frequency ranged from 10^6 to 10^4 Hz, which was attributed to proton transfer into the graphene layers (**Figures 5.12a** and **5.12b**). Additionally, a clear spike appears in the frequency region of lower than 2000 Hz, indicating that the positively-charged protons accumulation/depletion near the ion-blocking Pt electrodes in response to applied field. On the other hand, the Nyquist plot of Nafion membrane exhibited only a semiarc without a spike in the lower frequency region (**Figures 5.12c** and **5.12d**). This feature implies that the accumulation/depletion of positive charges at electrode/electrolyte interfaces is rather weak because counter anions can also penetrate through the Nafion membrane. The corresponding equivalent circuit models are shown in the insets of **Figures 5.12b** and **5.12d**, respectively. For the equivalent circuit from the graphene membrane device (inset of **Figure 5.12b**), R_s represents the resistance relevant to electrolyte and two electrodes; R_1 and CPE_1 are attributed to the resistance and capacitance, respectively, associated with the proton penetration through the graphene separating membranes; the CPE_2 represents the capacitance at the interfaces comprising electrolyte and ion-blocking Pt electrodes. For the Nafion membrane device (inset of **Figure 5.12d**), R_s, R_1 and CPE_1 represent the similar components as those of graphene device, however the capacitance components corresponding to polarization at Pt/electrolyte interfaces is absent due to the spectral features (i.e., semiarc). The R_1 values increased with increasing number of graphene layers, confirming the proton transport resistance enlarged with thickness of graphene layers (**Table 5.2**). With using a Nafion sheet as the separating membrane, the R_1 value is 20 times lower than that graphene layers as separating membrane. These features provide clear evidences that the proton penetration rate significantly limited by the resistance from graphene layers.

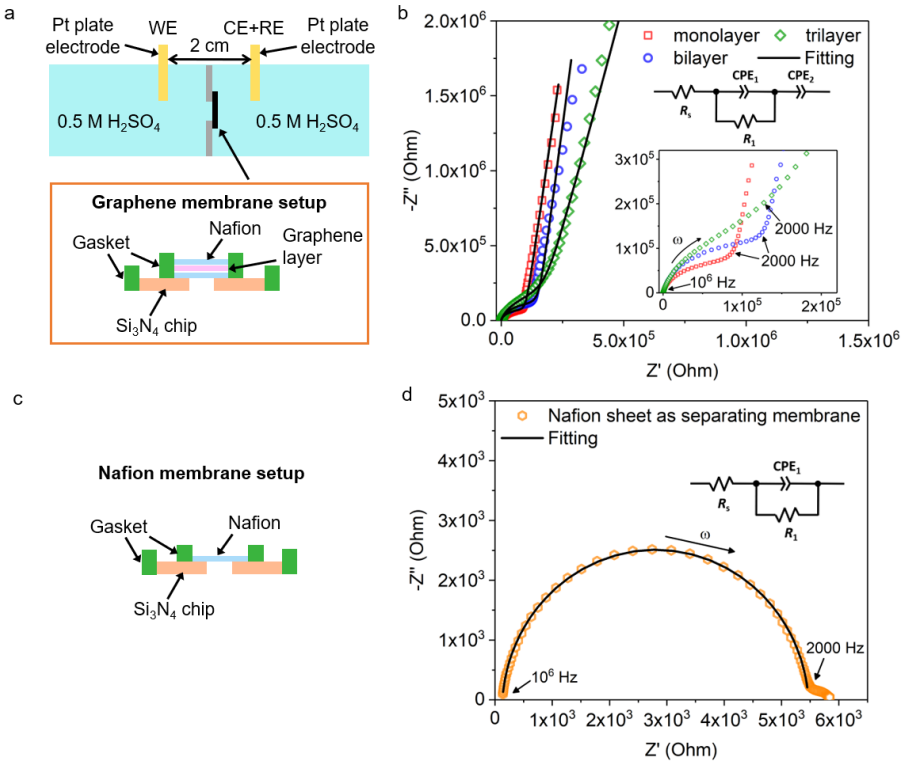

Figure 5.12 Electrochemical impedance spectroscopy. The device configurations of (a) the graphene membrane and (c) the Nafion membrane for electrochemical impedance measurements at a cell voltage of 1.6 V in a two Pt electrodes system. The Nyquist plots of membrane devices comprising (b) mono-, bi-, tri-layer graphene, and (c) Nafion sheet as the separating membranes. Insets in (b) and (d): equivalent circuits.

Table 5.2 The electrical resistances related to the proton penetration through graphene with various layer numbers.

Separating membrane	**Impedance R_1 value (Ω)**
Monolayer graphene	95338
Bilayer graphene	147294
Trilayer graphene	158092
Nafion sheet	5345

The time-dependence of proton penetration at a constant voltage in a three-electrode system was investigated by CA. The proton currents through N-doped graphene layers were observed to be ~1.5-times greater than those through non-doped graphene layers (**Figures 5.13a** and **5.13b**). It further confirms that the defects in N-doped graphene lattice enhance the proton penetration. Increasing the number of graphene layers reduces the proton currents, indicating an increased resistance to proton penetration. In particular, almost zero proton was observed for 10-layer non-doped and N-doped graphene membranes. Note that the proton currents through the graphene membranes (~80 nA) are much lower than that through only Nafion

sheet (15 μA) as the separating membrane (**Figure 5.15**), which reveals that the resistance of proton penetration mainly originates from the graphene layers rather than the protective Nafion sheets.

The speed of proton penetration through graphene layers was calculated (**Figure 5.13c**). The calculation is shown below,

$$\mathrm{n} = \frac{Q}{e} = \frac{I \times t}{e}$$

where n is the proton penetration speed; Q is the quantity of electric charge; I is the average current collected from eight-hours CA measurements; t is the penetration time; e is the elementary charge (1.6×10^{-19} C). The calculated proton penetration speed showed a decreased trend with increasing number of graphene layers, which could be ascribed to the raised resistance for proton penetration.

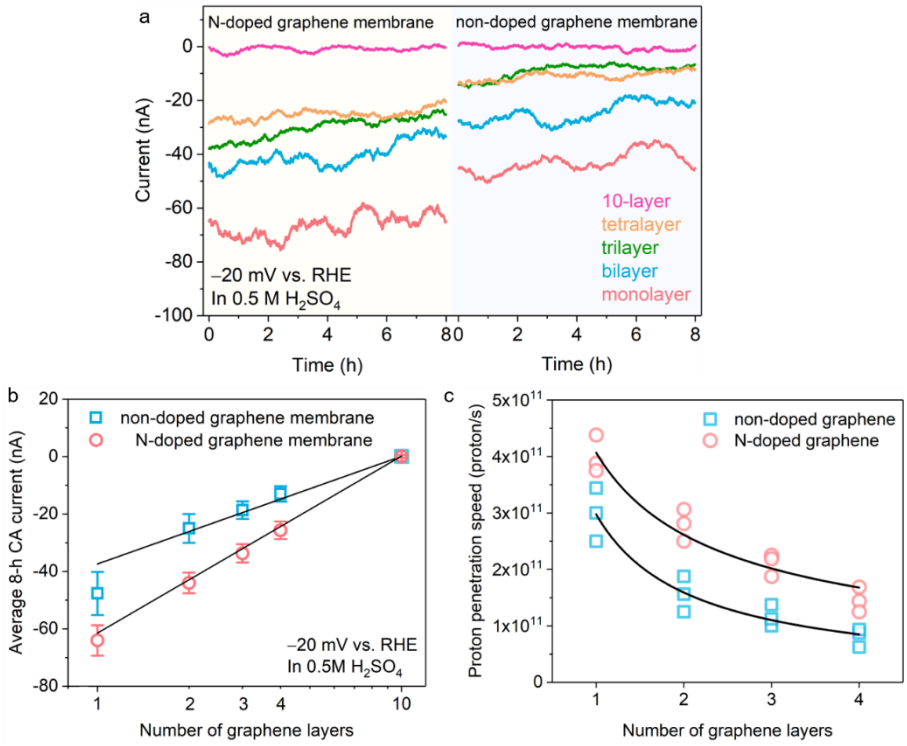

Figure 5.13 CA data for proton penetration through graphene layers. (a) Proton currents collected by CA at a cathode potential of −20 mV vs. RHE through non- and N-doped graphene membranes. (b) Average proton currents collected during eight hours of CA testing. (c) The calculated proton penetration speed through graphene with various layer numbers. Each single square or circle represents the average current from one single test. The black curves are the fit to the data.

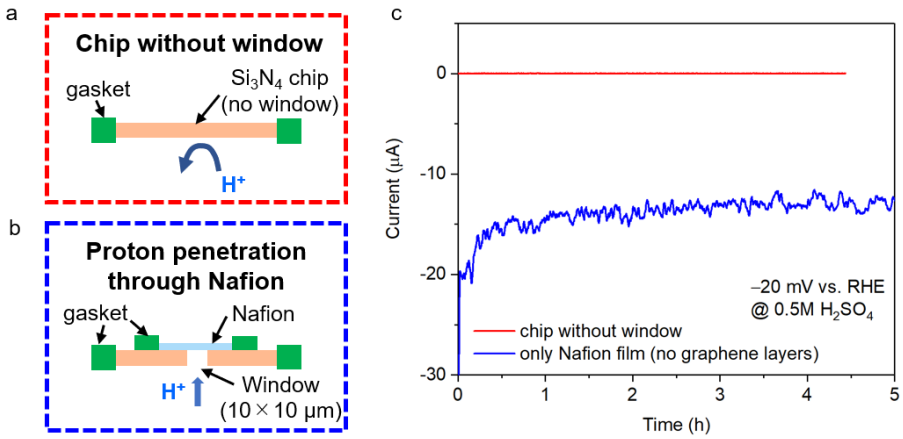

Figure 5.14 CA data when a Si_3N_4 chip without the central window or only Nafion sheet set as the separating membrane. (a) A configuration of the Si_3N_4 chip without the central window and (b) a Si_3N_4 chip with only Nafion sheet on the window area were used as separating membranes at a working electrode potential of –20 mV vs. RHE in a three-electrode system. (c) The corresponding CA results. The former device yielded no apparent current, indicating that the ion-impenetrable gasket can successfully block drift/diffusion of proton.

We correlated this proton penetration with the activities of the graphene-encapsulated NiMo catalysts. To do so, we plotted the average proton current (**Figure 5.13a**) as a function of the η_{10} overpotential (**Figure 4.7a**), the results of which are displayed in **Figure 5.15**. Surprisingly, excellent correlation between catalytic activity and proton penetration through the graphene layers was observed, which means that the catalytic activity of the NiMo nanoparticles encapsulated by graphene is governed by proton penetration through the graphene layers.

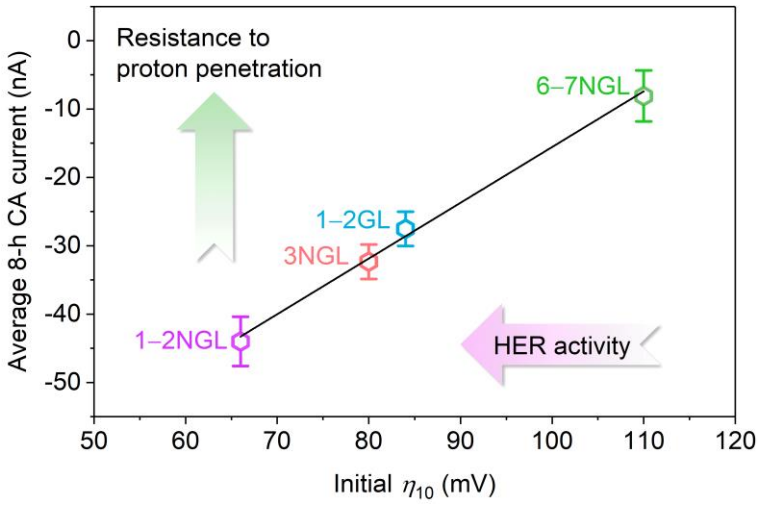

Figure 5.15 Correlation between catalytic activity and proton penetration through the graphene layers.

5.5 Unveiling proton-penetration pathways using density functional theory

Questions that arise here include: how does N-doped graphene enhance proton penetration compared to non-doped graphene and how does a proton penetrate through multiple graphene layers? To address these questions, we computed the energy barriers for proton penetration through a defect-free graphene lattice, a graphene lattice with a 5–7 defects, and several types of N-doped graphene lattices (**Figure 5.16**) using the nudged elastic band (NEB) method with a 2.6 nm × 2.5 nm unit cell[152].

An energy barrier is needed to be overcome for a proton penetration through graphene lattices. The values of the energy barriers for the proton penetration through various types of graphene lattices are exhibited in **Figure 5.16b**. A positive or negative value indicates that the shape of the potential energy surface involves a peak or a trough. As illustrated in **Figure 5.16a**, the whole process that a proton penetrates through graphene lattices can be divided into two steps: (1) the proton adsorbed on the graphene lattice; (2) the desorption of the proton from the graphene lattice. The necessary energy that needs to be overcome for proton penetration is called as "energy barrier". The negative energy value for "SV-3N" lattice means that the proton energetically prefers to adsorb on the lattice rather than penetration, therefore an energy of 3.30 eV is needed for desorption. As shown in the energy diagram, the energy barriers for "defect-free lattice" and "SV-3N lattice" are 3.16 eV and 3.30 eV, respectively.

To penetrate through the defect-free graphene lattice, the proton needs to overcome an energy barrier of 3.16 eV (**Figure 5.16b** and **Table 5.3**). In contrast, the existing of 5–7 defect in graphene lattice largely decreased the energy barrier to 2.30 eV. The barrier reduction arises from the fact that the a proton can more easily penetrate through the seven-membered carbon rings in the defect than the six-membered carbon rings in the defect-free graphene[32, 153].

Pyridinic N-dopants also contribute to the lower energy barrier for proton penetration. The pyridinic N-doped graphene lattice requires an energy barrier of 2.35 eV for proton penetration through its six-membered carbon rings, which is 0.81 eV lower than that of the defect-free lattice (**Figure 5.16b**) and is ascribable to the electronegativity of the N-dopant (**Figure 5.17**). Proton penetration through N-doped graphene lattices containing a single vacancy (SV) and three N-dopants (SV-3N) requires more energy than penetration through a defect-free lattice, due to stronger proton/N binding (i.e., protons tend to be trapped by N-dopants). However, the adsorption of H atoms at the N-dopants reduces the barrier to proton penetration by contributing to proton repulsion. For example, the SV-3N lattice with one adsorbed H atom (SV-3N-1H) exhibits a smaller energy barrier (2.65 eV) compared to that (3.30 eV) for the SV-3N lattice. Our results suggest that 5–7 topological defects and pyridinic N-dopants contribute to reducing the proton-penetration energy barriers.

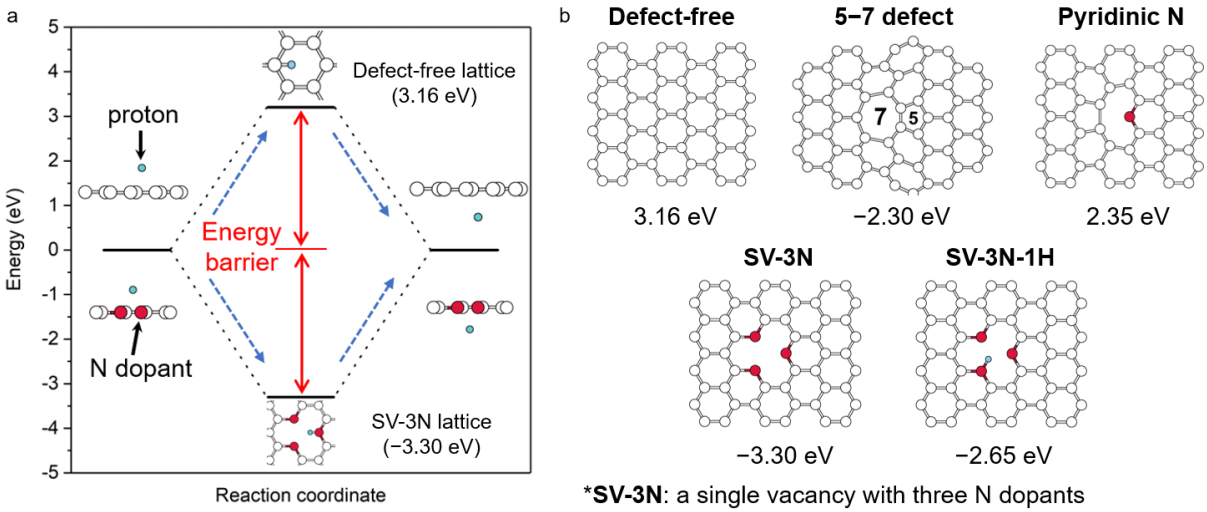

Figure 5.16 Energy barriers of proton penetration through graphene lattices. (a) Energy diagram of proton penetration through graphene lattices via the defect-free lattice and the SV-3N lattice. Color code: Carbon (white), Nitrogen (red), and Proton (blue). (b) Atomic models of various types of graphene lattice. The numbers under the graphene lattices are the calculated energy barriers for proton penetration through the lattices.

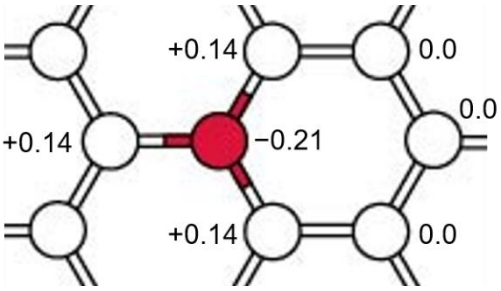

Figure 5.17 Charge density distribution of N-doped graphene lattice. The numbers are the electric charges on C and N atoms. Color code: Carbon (white) and Nitrogen (red). The charges are in the unit of *e*.

Table 5.3 The value of the energy barrier for proton penetration through non-doped graphene layers in published literatures.

Graphene layer number	Energy barrier (eV)	Reference
Monolayer (no defect)	3.16	This work
Monolayer (no defect)	2.8	Nanoscale, 10, 5350 (2018)
Monolayer (no defect)	3.9	Nat Commun, 6, 6539 (2015)
Monolayer (no defect)	1.56	2D Mater., 3, 025004 (2016)
Monolayer (no defect)	1.25−1.40	Nature, 516, 227 (2014)
Monolayer (no defect)	1.17	New J. Phys. 12, 125012 (2010)
Monolayer (no defect)	1.41	Phys. Chem. Chem. Phys. 15, 16132–16137 (2013)

To determine how a proton can penetrate through multiple graphene layers, we calculated the energy barriers for proton hopping between bilayer SV-3N graphene lattices (**Figure 5.18a**). As discussed above, a proton can be trapped by a pyridinic N-dopant. Such a trapped/adsorbed proton can hop to another pyridinic N-dopant in another graphene layer. The energy barrier for proton hopping depends highly on the relative positions of the pyridinic N-dopants in the two layers (1.56–4.10 eV). The energy barrier can be as low as 1.56 eV when the two N-dopants are close to each other; this barrier is smaller than that for pyridinic N-doped monolayer graphene (**Figure 5.16b**). Our results show that a proton can penetrate through multiple graphene layers by hopping between N-dopants.

The pathway for proton movement through multiple graphene layers to the NiMo surface is summarized in **Figure 5.18b**. A proton is first adsorbed at an N-dopant in the upper lattice (step 1). After desorption, the proton intercalates into the bilayer lattice (step 2). A similar adsorption of a proton in the lower lattice occurs (step 3). The proton finally exits the lower lattice and is adsorbed on the encapsulated NiMo substrate (steps 4 and 5) where it undergoes molecular hydrogen (H_2) evolution on the surface. According to this sequence of events, adsorption on the NiMo substrate is energetically preferable to complete desorption following penetration (i.e., returning to the initial state requires an energy barrier of 4.63 eV).

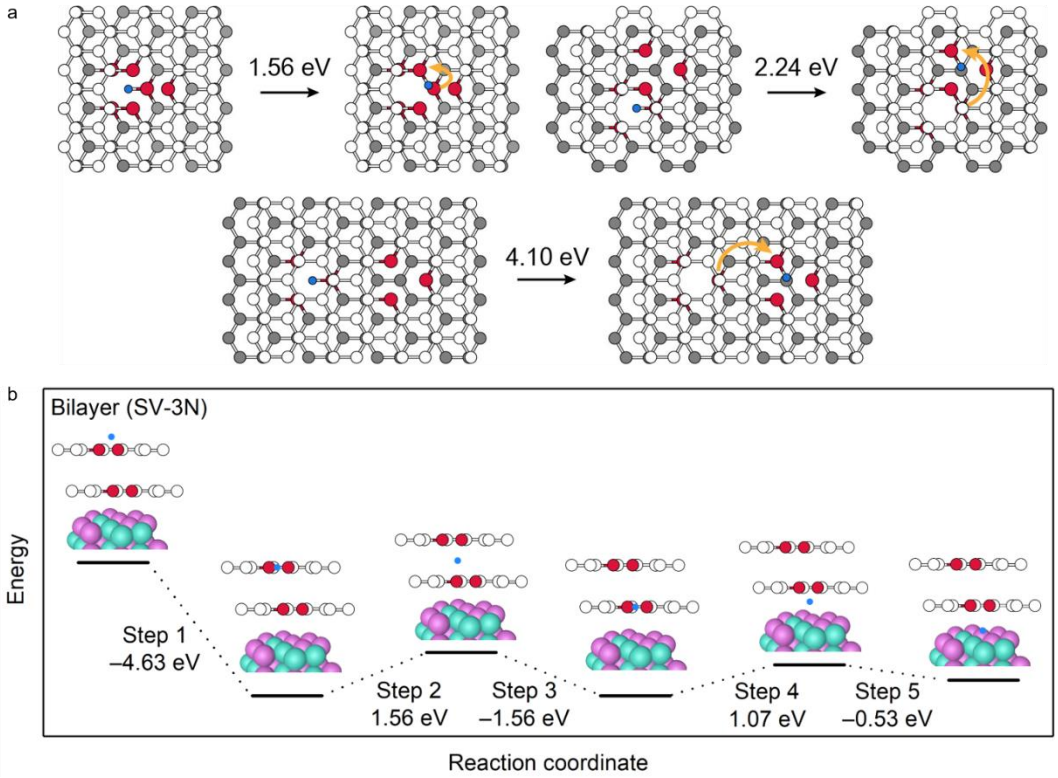

Figure 5.18 Proton penetration through bilayer graphene lattice. (a) Energy barriers for proton hopping between bilayer SV-3N graphene lattices (1st layer: white and 2nd layer: grey). Orange arrows indicate the hopping direction. Color code: Carbon (white and grey), Nitrogen (red), and Proton (blue). (c) Energy diagram for proton penetration through a bilayer SV-3N graphene lattice. The proton is adsorbed on a NiMo nanoparticle after penetrating through the encapsulating graphene bilayer.

The release of generated H_2 through graphene lattices was similarly investigated (**Figures 5.19**, **5.20**, and **Table 5.4**). According to our investigations and reported litereatures[66, 86, 87], the H_2 is impermeable to a defect-free graphene lattice, whereas defects and nanopores in graphene lattices are permeable to H_2. Although a H_2 required an energy barrier of 4.6–5.4 eV to pass through graphene with a topological defect (e.g. 5−7 or 5−8−5 defect), the energy barrier reduced to less than 1.00 eV through graphene nanopores (diameter: 2.5–7.4 Å) (**Figure 5.19**). To penetrate through a SV-3N lattice (**Figure 5.20**), the H_2 firstly decomposed into two H atoms, adsorbed on the N-dopant sites, penetrated through the defects one by one, and recombined after penetration. This two-step sequence of decomposition and recombination significantly reduced the overall energy barrier of H_2 penetration to 1.15 eV. Thus, the nanopores and defects induced by N-doping facilitate the release of generated H_2.

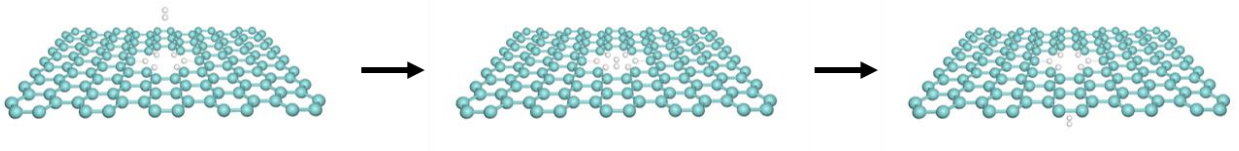

Figure 5.19 H_2 penetration through the monolayer non-doped graphene lattice with a nanopore. Six hydrogen atoms adsorbed on the carbon atoms along the edge of the nanopore, in which the penetration energy barrier can be further reduced to 0.68 eV. The cyan and white balls represent the C and H atoms.

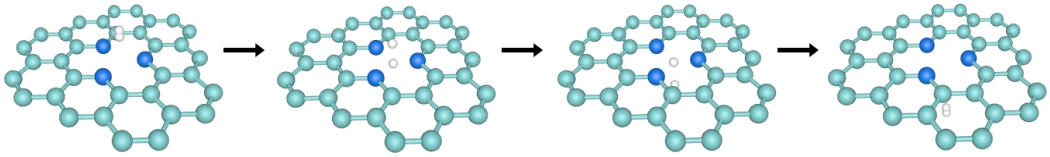

Figure 5.20 H_2 penetration through the SV-3N graphene lattice by a decomposition−recombination process. This two-step sequence of decomposition and recombination largely reduced the overall energy barrier of H_2 penetration to 1.15 eV. The cyan, blue, and white balls represent the C, N, and H atoms, respectively.

Table 5.4 The values of the energy barriers for a H_2 penetration through monolayer graphene in published literatures.

Graphene layer number	Energy barrier (eV)	Penetration mode	Reference
Non-doped graphene (5−7 defect)	5.4	Direct penetration	This work
Non-doped graphene (5−8−5 defect)	4.6	Direct penetration	This work
Non-doped graphene (no defect)	4.8	H_2 decomposition−H atom penetration−recombination	This work
Non-doped graphene (SV-3N defect)	1.15	H_2 decomposition−H atom penetration−recombination	This work
Non-doped graphene (with a pore diameter of 3.5 Å)	0.68	Direct penetration	This work
Non-doped graphene (with a pore diameter of 2.5−3.0 Å)	0.025−0.22	Direct penetration	Nano Lett., 9, 4019, 2009
Non-doped graphene (with an angstrom-sized pore)	1.12	Direct penetration	Nature Nanotech, 10, 785 (2015)
Non-doped graphene (with a pore diameter of 7.4 Å)	0.54	Direct penetration	Carbon, 54, 359 (2013)
Non-doped graphene (with a pore diameter of 3.5 Å)	0.30−0.41	Direct penetration	J. Phys. Chem. C, 118, 19172 (2014)
Non-doped graphene (with a pore diameter of 5.8 Å)	0.09−0.25	Direct penetration	J. Phys. Chem. C, 118, 19172 (2014)
Non-doped graphene (with a pore diameter of 3.6 Å)	0.12	Direct penetration	Surface Science, 607, 153 (2013)
Non-doped graphene (with a pore diameter of 3.7 Å)	0.28−0.58	Direct penetration	Phys. Chem. Chem. Phys., 14, 13292 (2012)
N-doped graphene (with a pore diameter of 3.7 Å)	0.17−1.66	Direct penetration	Phys. Chem. Chem. Phys., 14, 13292 (2012)

5.6 HER mechanisms for graphene-encapsulated NiMo catalysts

We explored the impact of proton penetration on catalytic activity by combining HER catalytic-activity experiments for graphene-encapsulated NiMo catalysts, graphene-membrane proton-penetration characterization data, and DFT-calculated energy barriers for proton penetration. The linear relationship between the required overpotential in the NiMo catalyst and the proton current in the graphene membrane (**Figure 5.15**) strongly suggests that catalytic activity is dominated by proton penetration through the graphene layers. DFT calculations reveal that N-doped graphene exhibits enhanced proton penetration compared with non-doped graphene due to graphene-lattice deformation through N-doping as well as the electronegativity of the N-atom dopant (**Figure 5.17**), which is in agreement with the experimental data (**Figure 5.13b**). The overall process is summarized in **Figure 5.21a**.

On the other hand, it has often been reported that the catalytic HER reaction occurs on the outermost graphene layer (**Figure 5.21b**)[154, 155], which begs the question: can this process compete with the proton-penetration process? To address this question, we investigated the HER activities of the NiMo catalyst encapsulated by 6−7NGL as well as the 6−7NGL devoid of the NiMo catalyst. If the catalytic reaction that occurs at the graphene surface can compete with the NiMo catalytic process by proton penetration through the graphene layers, the required overpotentials of the 6−7NGL samples with and without the NiMo substrates should be comparable. However, the CV results indicate that an overpotential of 110 mV is required for the NiMo sample encapsulated by 6−7NGL to deliver 10 mA cm^{-2}, while the NiMo-free 6−7NGL sample is unable to deliver a current density of 10 mA cm^{-2}, even with an overpotential of 600 mV, which reveals that the process depicted in **Figure 5.21b** is a minor contributor, while the process shown in **Figure 5.21a** dominates for graphene-encapsulated NiMo samples.

Graphene encapsulation is also important for ensuring the catalyst lifetimes of non-noble-metal catalysts. The monolayer graphene-encapsulated NiMo catalyst dissolves during 1000 CV cycles (**Figure 5.22**), whereas the catalyst with multilayers of graphene endures 1000 CV cycles and CA testing for one week (**Figures 5.23** and **5.24**). These results confirm that protons reach the NiMo surface and dissolve the NiMo catalyst. Moreover, corrosion resistance (i.e., high energy barriers) gradually increases and the degree of proton penetration decreases with increasing numbers of encapsulating graphene layers; hence, HER activity is sacrificed for improved catalyst lifetime (i.e., to protect NiMo in the acidic medium) (**Figure 5.15**) due to the low quantity of penetrating protons.

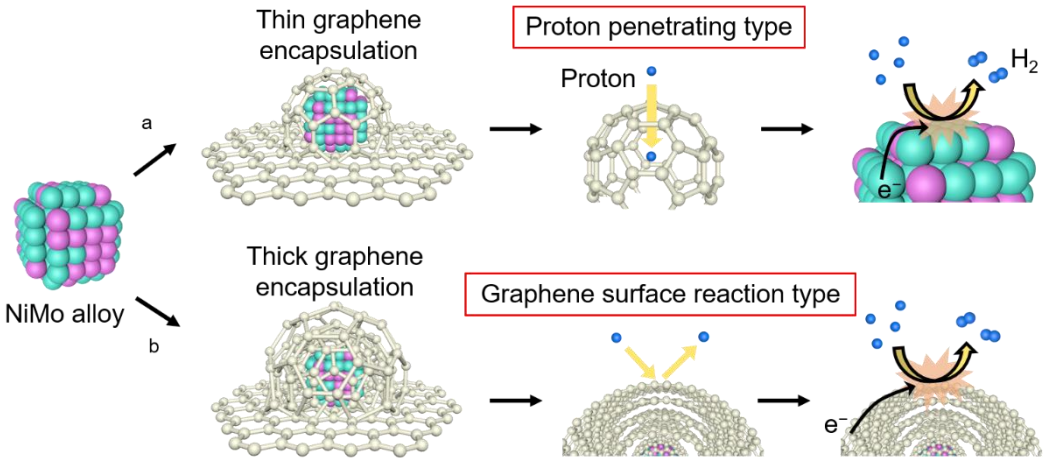

Figure 5.21 Schematic HER mechanisms for graphene-encapsulated NiMo catalysts. (a) Encapsulation by thin graphene layers (proton-penetrating-type mechanism). Protons penetrate through the thin graphene layers and H_2 evolution occurs on the surface of the underlying NiMo nanoparticle. (b) Encapsulation by thick graphene layers (graphene-surface-reaction-type mechanism). The large resistance and energy barrier impede proton penetration. The HER mainly occurs on the most outer graphene lattice.

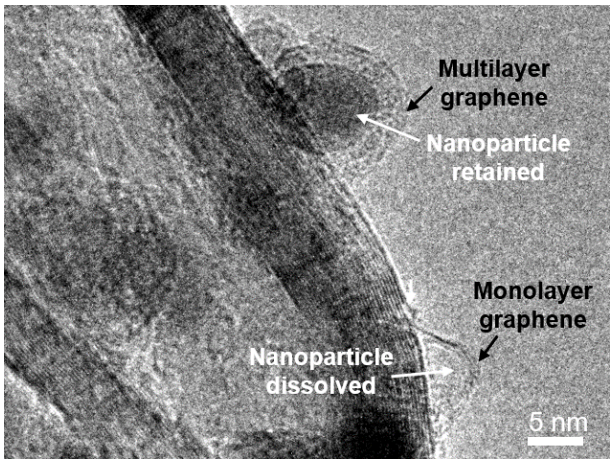

Figure 5.22 HRTEM image of the 1−2NGL catalyst after 1000 CV cycles testing in 0.5 M H_2SO_4 electrolyte.

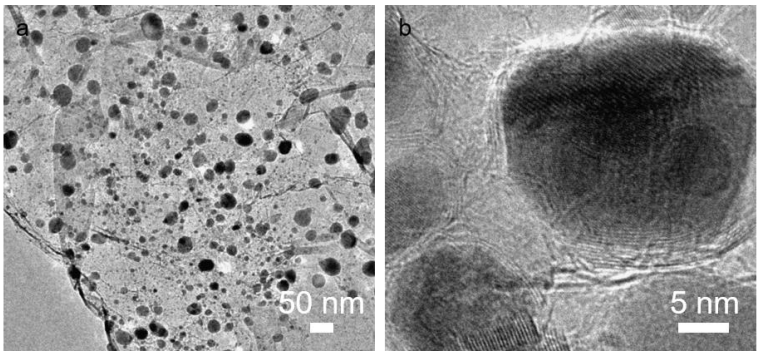

Figure 5.23 TEM image of the 6−7NGL catalyst after 1000 CV testing cycles in 0.5 M H_2SO_4 electrolyte. (a) Overview and (b) Zoom-in images.

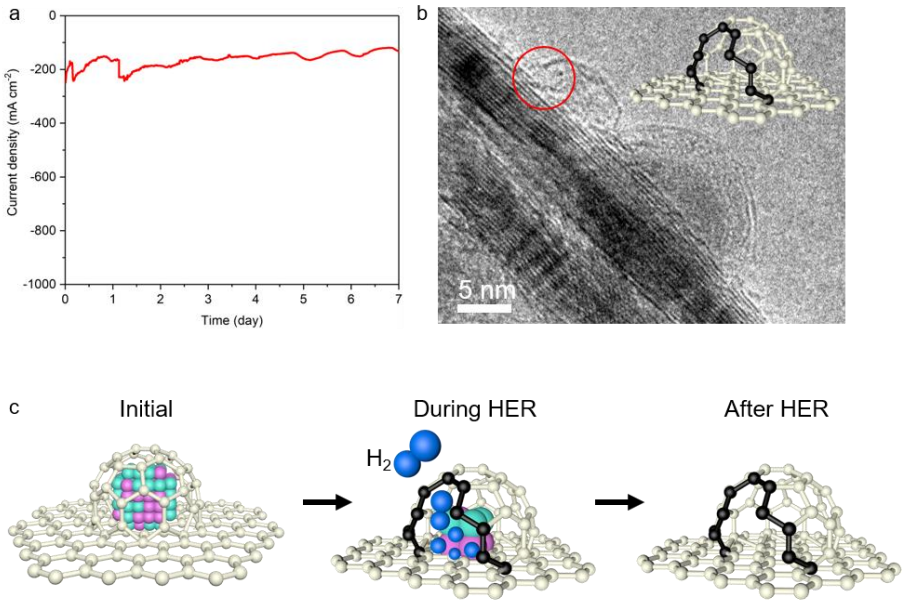

Figure 5.24 HER activity and morphological changes of the 3NGL catalyst after long-term durability test. (a) The current of the 3NGL catalyst at a potential of −250 mV vs. RHE for seven days in 0.5 M H_2SO_4 electrolyte. (b) The corresponding TEM image of catalyst after the CA experiment. A nanopore on the encapsulation graphene layer was observed (highlighted in red circle). Inset: the schematic of a broken encapsulating graphene (the breakage edge is highlighted in black). (c) Schematic of the graphene breakage generation during the HER process. Generated H_2 were released through the nanopore region. The blue sphere represents the H_2. When large amounts of H_2 were generated on NiMo surface, the release of H_2 as well as dissolved Ni and Mo ions through large defects or nanopores resulted in the breakage of encapsulating graphene layers, which is confirmed by the TEM image of catalyst after seven days CA testing.

5.7 Conclusions

In conclusion, the effect of proton penetration behaviour through graphene layers on HER mechanisms of graphene-encapsulated NiMo catalysts were systematically investigated. The HER activity and corrosion of the graphene-encapsulated catalyst was found to be governed by the degree of proton penetration as determined by the number of encapsulating graphene layers. Experimental results demonstrated that layer number, N-doping, and structural defects in the encapsulating graphene governs the degree of proton penetration and, as a consequence, the catalytic HER activity. Hence, engineering the thickness, doping level, and defect density of the graphene can increase the HER activity of an NiMo catalyst, while simultaneously suppressing its corrosion. The increasing number of encapsulating graphene layers resulted in a raised resistance to proton penetration, which could choke off the proton pathways from bulk electrolyte to underlaying catalyst surface. DFT calculations confirmed the possibility of penetration of proton and generated H_2 through graphene lattices; topological and doping-induced defects in graphene lattices contributed to the reduction of energy barriers of proton penetration. Using techniques that optimize the factors, including layer number, chemical doping, and degree of structural defects, in the encapsulating graphene are keys to improving the usability of non-noble-metal catalysts not only for the HER in acidic media, but also for various circumstances that require the corrosion-resistance of non-noble metals.

Chapter 6 Conclusions

Due to the common consensus of the development of a sustainable society, the low-carbon and high-efficiency energy sources are in high demand. Hydrogen, as a flexible and “zero-emission” energy carrier, has been attracted many attentions for the potential applications in the next-generation energy system. The PEM water electrolyzer with power supply derived from renewable energies emerges as a promising and feasible approach to generating cost-efficient hydrogen gases in a large scale. In order to reduce the high cost of the PEM water electrolyzer, it is of importance to develop earth-abundant-metal catalysts to replace currently used Pt metal catalysts under acidic media in PEM electrolyzer.

In this dissertation, I successfully synthesized a novel graphene-encapsulated NiMo nanoparticles as HER catalysts used in acidic electrolytes. The acid-soluble property of NiMo alloy has been addressed due to the protection of chemically stable encapsulating graphene layers. The layer number of encapsulating graphene plays a key role in balancing catalytic activity and corrosion resistance, which has been confirmed by experimental results and theorical calculations. The results reveal that the proton penetration behaviour varied with the number of graphene layers are the underlying reasons for high HER activity and catalyst corrosion. Furthermore, The HER activity and corrosion of the graphene-encapsulated catalyst was found to be governed by the degree of proton penetration as determined by the number of encapsulating graphene layers.

In chapter 1, the research background and important theories involved in this dissertation have been summarized, which includes the role and demand of hydrogen in our society, the concept of hydrogen production from water electrolysis, the advantage of NiMo alloy as a HER catalyst, the base of graphene encapsulation method, the graphene penetration through graphene layers, the graphene synthesis by CVD, and the basic descriptor of HER catalyst in DFT calculations.

In chapter 2, all the experimental methods involved in this dissertation have been introduced, including the syntheses of various types of catalysts, the measurements for structural characterizations, electrochemical measurements, and the DFT calculations.

In chapter 3, the novel 3D bicontinuous porous NiMo alloy has been synthesized by a hydrothermal method and its electrochemical characteristics under alkaline media has been investigated. The formation of porous structures required 800 °C annealing temperature, and the complete reduction of Mo oxide species needed the temperature beyond 950 °C. The 3D NiMo alloy exhibited a Pt-like HER performance in 1.0 M KOH electrolyte and retained the current density around 25 mA cm^{-2} for more than 12 days. Such non-noble porous metal alloys could be good replacements to Pt metal catalysts in alkaline media. This work shows an efficient way to develop inexpensive 3D porous non-noble metal catalysts for hydrogen productions.

In chapter 4, graphene has been successfully employed as the protective layer for NiMo

nanoparticles by CVD. The graphene-encapsulated NiMo nanoparticles showed high HER activities and excellent stabilities under acidic media. Experimental results and DFT calculations suggested that the number of encapsulating graphene layer plays a significant role in HER performance, chemical durability, and charge distribution. The results showed that NiMo nanoparticles encapsulated by 3 layers N-doped graphene afforded the excellent balance between corrosion resistance and catalytic activity. For instance, this catalyst exhibited a low potential of 80 mV to reach a current density of 10 mV cm^{-2} and a small Tafel slope value of 60 mV dec^{-1}; additionally, more than 92% of initial current density was retained for 25 h in 0.5 M H_2SO_4, which confirms the remarkable acid resistance ability. The described graphene encapsulation technique provides a new direction for exploiting low-cost, non-noble metal catalysts in acidic electrolytes for efficient hydrogen production.

In chapter 5, the effect of proton penetration behaviour through graphene layers have been investigated to reveal the HER mechanisms of graphene-encapsulated NiMo catalysts. The increasing number of encapsulating graphene layers resulted in a raised resistance for the proton penetration, which could choke off the proton pathways from bulk electrolyte to underlaying catalyst surface. DFT calculations further confirmed the possibility of proton penetration and generated H_2 release through encapsulating graphene layers. N-doping-induced defects in graphene lattices contributed to the reduction of the energy barrier for proton/H_2 penetration. The corrosion resistance (i.e., high energy barriers) gradually increases and the degree of proton penetration decreases with increasing numbers of encapsulating graphene layers; hence, HER activity is sacrificed for improved catalyst lifetime (i.e., to protect NiMo in the acidic medium) due to the low quantity of penetrating protons. The layer number, N-doping, and structural defects in the encapsulating graphene governs the degree of proton penetration and, as a consequence, the catalytic HER activity. Hence, engineering the thickness, doping level, and defect density of the graphene can increase the HER activity of an NiMo catalyst, while simultaneously suppressing its corrosion.

In summary, this study provides a new fundamental understanding of the HER mechanism of graphene-encapsulated non-noble-metal catalysts in acidic electrolytes. This technology paves the design direction for non-noble-metal catalysts that can achieve the balance between corrosion resistance and catalytic activity, which shows promising to cut cost of HER catalysts used in PEM electrolyzers. The cost-efficient water electrolysis will spread in use of the “zero-emission” energy carrier, hydrogen, as the advantages of flexibility, sustainability, and environmental friendliness. The renewable power supplied hydrogen production contributes to a sustainable, economic, and clean next-generation energy system.

Lists of publications and presentations

Publications (Related to this Ph.D. dissertation)

(1) **K. L. Hu**, S. Jeong, M. Wakisaka, J.-i. Fujita and Y. Ito, Bottom-up Synthesis of Porous NiMo Alloy for Hydrogen Evolution Reaction, Metals, 2018, 8, 83. (Related to chapter 3)

(2) **K. L. Hu**, T. Ohto, L. H. Chen, J. H. Han, M. Wakisaka, Y. Nagata, J.-i. Fujita, and Y. Ito, Graphene Layer Encapsulation of Non-Noble Metal Nanoparticles as Acid-Stable Hydrogen Evolution Catalysts, ACS Energy Letters, 2018, 3, 1539-1544. (Related to chapter 4)

(3) **K. L. Hu**, T. Ohto, Y. Nagata, M. Wakisaka, Y. Aoki, J.-i. Fujita and Y. Ito, Graphene-encapsulated Non-Noble-Metal Catalyst Is Governed by Proton Penetration in Electrochemical Hydrogen Evolution Reaction, submitted. (Related to chapter 5)

Publications (Others)

(4) **K. L. Hu**, M. X. Wu, S. Hinokuma, M. Wakisaka, J.-i. Fujita and Y. Ito, Boosting Electrochemical Water Splitting via Ternary NiMoCo Hybrid Nanowire Arrays, Journal of Materials Chemistry A, 2019, 7, 2156-2164.

(5) H. J. Qiu†, P. Du†, **K. L. Hu**† (equal contribution), J. J. Gao, H. L. Li, P. Liu, T. Ina, K. Ohara, Y. Ito, M. W. Chen, Metal and Nonmetal Codoped 3D Nanoporous Graphene for Efficient Bifunctional Electrocatalysis and Rechargeable Zn–Air Batteries, Advanced Materials, 2019, 31, 1900843.

(6) S. Jeong, **K. L. Hu**, T. Ohto, Y. Nagata, H. Masuda, J.-i. Fujita and Y. Ito, Effect of Graphene Encapsulation of NiMo Alloys on Oxygen Evolution Reaction, ACS Catalysis, 2020, 10, 792-799.

(7) L. H. Chen, J. H. Han, Y. Ito, T. Fujita, G. Huang, **K. L. Hu**, A. Hirata, K. Watanabe and M. W. Chen, Heavily Doped and Highly Conductive Hierarchical Nanoporous Graphene for Electrochemical Hydrogen Production, Angew. Chem. Int. Ed., 2018, 57, 13302-13307.

(8) Y. Ito, T. Ohto, D. Hojo, M. Wakisaka, Y. Nagata, L. H. Chen, **K. L. Hu**, M. Izumi, J.-i. Fujita and T. Adschiri, Cooperation between holey graphene and NiMo alloy for hydrogen evolution in an acidic electrolyte, ACS Catalysis, 2018, 8, 3579-3586.

(9) I. D. Bernardo, G. Avvisati, C. Y. Chen, J. Avila, M. C. Asensio, **K. L. Hu**, Y. Ito, P. Hines, J. L. Duffin, L. Rintoul, N. Motta, C. Mariani, M. G. Betti, Topology and doping effects in three-dimensional nanoporous graphene, Carbon, 2018, 131, 258-265.

(10) A. Kumatani, C. Miura, H. Kuramochi, T. Ohto, M. Wakisaka, Y. Nagata, H. Ida, Y. Takahashi, **K. L. Hu**, S. Jeong, J.-i. Fujita, T. Matue and Y. Ito, Chemical dopants on edge of holey graphene accelerate electrochemical hydrogen evolution reaction, Advanced Science, 2019, 1900119.

(11) Y. Ito, Y. Habata, H. Kuramochi, E. Kusuda, **K. L. Hu**, H. Masuda, J. Fujita, Y. Nagata, M. Watanabe and A. Isdepsky, Damage-Free Solar Dewatering of Micro-Algal Concentrates via Multifunctional Hierarchical Porous Graphene, Advanced Sustainable Systems, 2019, 1900045.

Presentations

(1) **K. L. Hu**, T. Ohto, Y. Nagata, M. Wakisaka and Y. Ito, the 5th International Symposium on Innovative Materials and Processes in Energy Systems, Kanazawa, Japan. 09/2019. (Oral presentation)

(2) **K. L. Hu**, T. Ohto, M. Wakisaka, Y. Nagata, J.-i. Fujita and Y. Ito, the International Functional Nanomaterials and Nanodevice Conference, Vienna, Austria. 09/2018. (Oral presentation)

(3) **K. L. Hu**, J.-i. Fujita and Y. Ito, the 11th Annual meeting of Japan Society for Molecular Science, Sendai, Japan. 09/2017. (Post presentation)

Acknowledgements

Foremost, I would like to express my sincerest gratitude to those who have advised, mentored, and supported me during the three years.

I especially want to acknowledge my advisor, Prof. Yoshikazu Ito, for his guidance, patience, and friendship all the time. He has been teaching and guiding me to all aspects of electrochemical water catalysis and graphene materials; always train me how to work smart and think creatively; give me the opportunity and enough freedom to explore the research path; afford many insightful and fruitful discussions about my researches. Outside of the lab, he also cares about my life in Japan and give the supports as much as he can. For example, he lent me his own car for my apartment moving. I am very grateful for his help for the applications of Sasakawa Scientific Research Grant and Kato Foundation for Promotion of Science Bounty. A special thanks to his kind support and patience for my document work of the visiting scholar to the Ohio State University, which lasts for several months and costs him countless time. It is very lucky for me to work with him, and these three years will be an invaluable treasure for both my academic career and whole life.

I would also like to thank my co-advisor, Prof. Junichi Fujita, for his guidance of my projects and the teaching about CVD and SEM/TEM. Prof. Hideki Masuda always give me helps for the experiments. Mrs. Chiaki Yamaoka, the secretary in the lab, has been helping all the document works from the universities or other institutes, and I also enjoy the chat with her about the Japanese cultures and daily life. Mr. Masahiko Izumi, the engineer in the lab, is a warmhearted gentleman who always give me useful advice on the viewpoint of engineering. In addition, I appreciate the helps from all the members in the lab: Dr. Kemeng Ji, Mr. Samuel Jeong, Mr. Hirotaka Kuramochi, Mr. Yu Kikuchi, Mr. Ryosuke Araki, Mr. Koichiro Nakamura, Mr. Kentaro Watanabe, Mr. Kanade Matsuo, Mr. Zeyu Xi, Mr. Wei Fu, Mr. Yuga Emoto, Mr. Yoshiya Kishibe, Mr. Takafumi Hasegawa, Mr. Yudai Mikami, Mr. Yuto Habata, and Mr. Mingxing Wu.

I would like to express appreciation to the collaborators. Dr. Yuki Nagata (Max Planck Institute for Polymer Research) helped me to analyze the experimental data and modify manuscripts; impress me in discussions for each detail through Skype. Prof. Tatsuhiko Ohto (Osaka University) performed DFT calculations and provided insightful comments from the viewpoint of a theoretical chemist. Prof. Mitsuru Wakisaka (Toyama Prefectural University) and Prof. Yoshitaka Aoki (Hokkaido University) gave me many important suggestions.

Finally, I express my heartfelt gratitude to my parents and my girlfriend. Thank all the understandings, supports, and patience, which motivate me and fill me with the courage and confidence to face the difficult and challenge directly.

My PhD program is financially supported by the Japanese government (MONBUKAGAKUSHO: MEXT) scholarship and the Sasakawa Scientific Research Grant (2019−3001).

References

1. Abbasi R*, et al.* A Roadmap to Low - Cost Hydrogen with Hydroxide Exchange Membrane Electrolyzers. *Advanced Materials*, 1805876 (2019).

2. Brown D. in CryoGas International (Ed: N. Parkinson). *Gasworld Publishing LLC*, 32 (2016).

3. Staffell I*, et al.* The role of hydrogen and fuel cells in the global energy system. *Energy & Environmental Science* **12**, 463-491 (2019).

4. Shih CF, Zhang T, Li J, Bai C. Powering the future with liquid sunshine. *Joule*, (2018).

5. Chi J, Yu H. Water electrolysis based on renewable energy for hydrogen production. *Chinese Journal of Catalysis* **39**, 390-394 (2018).

6. The future of hydrogen. *Report by International Energy Agency for the G20*, (2019).

7. Kélouwani S, Agbossou K, Chahine R. Model for energy conversion in renewable energy system with hydrogen storage. *Journal of Power Sources* **140**, 392-399 (2005).

8. Turner JA. A realizable renewable energy future. *Science* **285**, 687-689 (1999).

9. Barbir F. PEM electrolysis for production of hydrogen from renewable energy sources. *Solar energy* **78**, 661-669 (2005).

10. Ursua A, Gandia LM, Sanchis P. Hydrogen production from water electrolysis: current status and future trends. *Proceedings of the IEEE* **100**, 410-426 (2011).

11. Carmo M, Fritz DL, Mergel J, Stolten D. A comprehensive review on PEM water electrolysis. *International journal of hydrogen energy* **38**, 4901-4934 (2013).

12. Haryanto A, Fernando S, Murali N, Adhikari S. Current status of hydrogen production techniques by steam reforming of ethanol: a review. *Energy & Fuels* **19**, 2098-2106 (2005).

13. Ni M, Leung DY, Leung MK, Sumathy K. An overview of hydrogen production from biomass. *Fuel processing technology* **87**, 461-472 (2006).

14. Pivovar B, Rustagi N, Satyapal S. Hydrogen at scale (H2@ Scale): key to a clean, economic, and sustainable energy system. *The Electrochemical Society Interface* **27**, 47-52 (2018).

15. Isolda R, Shipman MA, Symes MD. Earth-abundant catalysts for electrochemical and photoelectrochemical water splitting. *Nature Reviews Chemistry* **1**, 0003 (2017).

16. Bard AJ, Faulkner LR, Leddy J, Zoski CG. *Electrochemical methods: fundamentals and applications*. wiley New York (1980).

17. Morales-Guio CG, Stern L-A, Hu X. Nanostructured hydrotreating catalysts for electrochemical hydrogen evolution. *Chemical Society Reviews* **43**, 6555-6569 (2014).

18. Russell J, Nuttall L, Fickett A. Hydrogen generation by solid polymer electrolyte water electrolysis (Preprint paper). *Am Chem Soc Div Fuel Chem* **18**, 24-40 (1973).

19. Ayers KE*, et al.* Research advances towards low cost, high efficiency PEM electrolysis. *ECS transactions* **33**, 3-15 (2010).

20. Price E. Durability and Degradation Issues in PEM Electrolysis Cells and its Components. *Johnson Matthey Technology Review* **61**, 47-51 (2017).

21. Langemann M, Fritz DL, Müller M, Stolten D. Validation and characterization of suitable materials for bipolar plates in PEM water electrolysis. *International journal of hydrogen energy* **40**, 11385-11391 (2015).

22. Greeley J, Jaramillo TF, Bonde J, Chorkendorff I, Nørskov JK. Computational high-throughput screening of electrocatalytic materials for hydrogen evolution. *Nature materials* **5**, 909-913 (2006).

23. Lee Y, Suntivich J, May KJ, Perry EE, Shao-Horn Y. Synthesis and activities of rutile IrO2 and RuO2 nanoparticles for oxygen evolution in acid and alkaline solutions. *The journal of physical chemistry letters* **3**, 399-404 (2012).

24. McCrory CC, Jung S, Peters JC, Jaramillo TF. Benchmarking heterogeneous electrocatalysts for the oxygen evolution reaction. *Journal of the American Chemical Society* **135**, 16977-16987 (2013).

25. Tian J, Cheng N, Liu Q, Sun X, He Y, Asiri AM. Self-supported NiMo hollow nanorod array: an efficient 3D bifunctional catalytic electrode for overall water splitting. *Journal of Materials Chemistry A* **3**, 20056-20059 (2015).

26. Sun T*, et al.* Ordered mesoporous NiCo alloys for highly efficient electrocatalytic hydrogen evolution reaction. *international journal of hydrogen energy* **42**, 6637-6645 (2017).

27. Yang Y, Lun Z, Xia G, Zheng F, He M, Chen Q. Non-precious alloy encapsulated in nitrogen-doped graphene layers derived from MOFs as an active and durable hydrogen

evolution reaction catalyst. *Energy & Environmental Science* **8**, 3563-3571 (2015).

28. Jiao Y, Zheng Y, Jaroniec M, Qiao SZ. Design of electrocatalysts for oxygen-and hydrogen-involving energy conversion reactions. *Chemical Society Reviews* **44**, 2060-2086 (2015).

29. Xie J*, et al.* Atomically-thin molybdenum nitride nanosheets with exposed active surface sites for efficient hydrogen evolution. *Chemical science* **5**, 4615-4620 (2014).

30. Kong D, Cha JJ, Wang H, Lee HR, Cui Y. First-row transition metal dichalcogenide catalysts for hydrogen evolution reaction. *Energy & Environmental Science* **6**, 3553-3558 (2013).

31. Zhang Y*, et al.* A hybrid of NiMo-Mo2C/C as non-noble metal electrocatalyst for hydrogen evolution reaction in an acidic solution. *Electrochimica Acta* **222**, 747-754 (2016).

32. Feng L-L*, et al.* High-index faceted Ni_3S_2 nanosheet arrays as highly active and ultrastable electrocatalysts for water splitting. *Journal of the American Chemical Society* **137**, 14023-14026 (2015).

33. Voiry D*, et al.* Enhanced catalytic activity in strained chemically exfoliated WS 2 nanosheets for hydrogen evolution. *Nature materials* **12**, 850 (2013).

34. Fujita T*, et al.* Chemically exfoliated ReS 2 nanosheets. *Nanoscale* **6**, 12458-12462 (2014).

35. Popczun EJ*, et al.* Nanostructured nickel phosphide as an electrocatalyst for the hydrogen evolution reaction. *Journal of the American Chemical Society* **135**, 9267-9270 (2013).

36. Wang X-D*, et al.* Self-supported NiMoP 2 nanowires on carbon cloth as an efficient and durable electrocatalyst for overall water splitting. *Journal of Materials Chemistry A* **5**, 7191-7199 (2017).

37. Tian J, Liu Q, Asiri AM, Sun X. Self-supported nanoporous cobalt phosphide nanowire arrays: an efficient 3D hydrogen-evolving cathode over the wide range of pH 0–14. *Journal of the American Chemical Society* **136**, 7587-7590 (2014).

38. Zheng Y*, et al.* Hydrogen evolution by a metal-free electrocatalyst. *Nature communications* **5**, 3783 (2014).

39. Ito Y, Cong W, Fujita T, Tang Z, Chen M. High Catalytic Activity of Nitrogen and Sulfur Co - Doped Nanoporous Graphene in the Hydrogen Evolution Reaction. *Angewandte Chemie International Edition* **54**, 2131-2136 (2015).

40. Ito Y, *et al.* Correlation between Chemical Dopants and Topological Defects in Catalytically Active Nanoporous Graphene. *Advanced Materials* **28**, 10644-10651 (2016).

41. Duan J, Chen S, Jaroniec M, Qiao SZ. Porous C3N4 nanolayers@ N-graphene films as catalyst electrodes for highly efficient hydrogen evolution. *ACS nano* **9**, 931-940 (2015).

42. Anantharaj S, Ede SR, Sakthikumar K, Karthick K, Mishra S, Kundu S. Recent trends and perspectives in electrochemical water splitting with an emphasis on sulfide, selenide, and phosphide catalysts of Fe, Co, and Ni: a review. *Acs Catalysis* **6**, 8069-8097 (2016).

43. Subbaraman R, *et al.* Trends in activity for the water electrolyser reactions on 3d M (Ni, Co, Fe, Mn) hydr (oxy) oxide catalysts. *Nature materials* **11**, 550 (2012).

44. Stamenkovic VR, *et al.* Trends in electrocatalysis on extended and nanoscale Pt-bimetallic alloy surfaces. *Nature materials* **6**, 241 (2007).

45. McCrory CC, Jung S, Ferrer IM, Chatman SM, Peters JC, Jaramillo TF. Benchmarking hydrogen evolving reaction and oxygen evolving reaction electrocatalysts for solar water splitting devices. *Journal of the American Chemical Society* **137**, 4347-4357 (2015).

46. Zhang J, *et al.* Efficient hydrogen production on $MoNi_4$ electrocatalysts with fast water dissociation kinetics. *Nature communications* **8**, 15437 (2017).

47. Weissmüller J, Newman RC, Jin H-J, Hodge AM, Kysar JW. Nanoporous metals by alloy corrosion: formation and mechanical properties. *Mrs Bulletin* **34**, 577-586 (2009).

48. Ding Y, Chen M. Nanoporous metals for catalytic and optical applications. *MRS bulletin* **34**, 569-576 (2009).

49. Qiu H-J, Kang J, Liu P, Hirata A, Fujita T, Chen M. Fabrication of large-scale nanoporous nickel with a tunable pore size for energy storage. *Journal of Power Sources* **247**, 896-905 (2014).

50. Guo X, Han J, Liu P, Ito Y, Hirata A, Chen M. Graphene@ Nanoporous Nickel Cathode for Li− O2 Batteries. *ChemNanoMat* **2**, 176-181 (2016).

51. Yuan W, Tang Y, Yang X, Wan Z. Porous metal materials for polymer electrolyte membrane fuel cells–a review. *Applied Energy* **94**, 309-329 (2012).

52. Tan Y, *et al.* Versatile nanoporous bimetallic phosphides towards electrochemical water splitting. *Energy & Environmental Science* **9**, 2257-2261 (2016).

53. Hansen TW, DeLaRiva AT, Challa SR, Datye AK. Sintering of catalytic nanoparticles: particle migration or Ostwald ripening? *Accounts of chemical research* **46**, 1720-1730 (2013).

54. Ito Y, Izumi M, Hojo D, Wakisaka M, Aida T, Adschiri T. One-step nanoporous structure formation using NiO nanoparticles: Pore size control and pore size dependence of hydrogen evolution reaction. *Chemistry Letters* **46**, 267-270 (2016).

55. Jin Y, Yue X, Shu C, Huang S, Shen PK. Three-dimensional porous MoNi 4 networks constructed by nanosheets as bifunctional electrocatalysts for overall water splitting. *Journal of Materials Chemistry A* **5**, 2508-2513 (2017).

56. McKone J, Sadtler B, Werlang C, Lewis N, Gray H. Ni–Mo nanopowders for efficient electrochemical hydrogen evolution. *ACS catalysis* **3**, 166-169 (2013).

57. Fang M*, et al.* Hierarchical NiMo-based 3D electrocatalysts for highly-efficient hydrogen evolution in alkaline conditions. *Nano Energy* **27**, 247-254 (2016).

58. Haslam GE, Chin X-Y, Burstein GT. Passivity and electrocatalysis of nanostructured nickel encapsulated in carbon. *Physical Chemistry Chemical Physics* **13**, 12968-12974 (2011).

59. Chen WF*, et al.* Hydrogen - evolution catalysts based on non - noble metal nickel – molybdenum nitride nanosheets. *Angewandte Chemie International Edition* **51**, 6131-6135 (2012).

60. Kuang P, Tong T, Fan K, Yu J. In situ fabrication of Ni–Mo bimetal sulfide hybrid as an efficient electrocatalyst for hydrogen evolution over a wide pH range. *Acs Catalysis* **7**, 6179-6187 (2017).

61. Kirkland N, Schiller T, Medhekar N, Birbilis N. Exploring graphene as a corrosion protection barrier. *Corrosion Science* **56**, 1-4 (2012).

62. Novoselov KS*, et al.* Electric field effect in atomically thin carbon films. *science* **306**, 666-669 (2004).

63. Neto AC, Guinea F, Peres NM, Novoselov KS, Geim AK. The electronic properties of graphene. *Reviews of modern physics* **81**, 109 (2009).

64. Shi L, Xu A, Chen G, Zhao T. Theoretical understanding of mechanisms of proton exchange membranes made of 2D crystals with ultrahigh selectivity. *The journal of physical chemistry letters* **8**, 4354-4361 (2017).

65. Leenaerts O, Partoens B, Peeters F. Graphene: A perfect nanoballoon. *Applied Physics*

Letters **93**, 193107 (2008).

66. Bunch JS*, et al.* Impermeable Atomic Membranes from Graphene Sheets. *Nano Letters* **8**, 2458-2462 (2008).

67. Hu S*, et al.* Proton transport through one-atom-thick crystals. *Nature* **516**, 227-230 (2014).

68. Deng J, Ren P, Deng D, Bao X. Enhanced electron penetration through an ultrathin graphene layer for highly efficient catalysis of the hydrogen evolution reaction. *Angewandte Chemie International Edition* **54**, 2100-2104 (2015).

69. Shen Y, Zhou Y, Wang D, Wu X, Li J, Xi J. Nickel-Copper Alloy Encapsulated in Graphitic Carbon Shells as Electrocatalysts for Hydrogen Evolution Reaction. *Advanced Energy Materials* **8**, 1701759 (2018).

70. Yang X*, et al.* N-Doped graphene-coated molybdenum carbide nanoparticles as highly efficient electrocatalysts for the hydrogen evolution reaction. *Journal of Materials Chemistry A* **4**, 3947-3954 (2016).

71. Jiao D, Pengju R, Dehui D, Liang Y, Fan Y, Xinhe B. Highly active and durable non-precious-metal catalysts encapsulated in carbon nanotubes for hydrogen evolution reaction. *Energy & Environmental Science* **7**, 1919-1923 (2014).

72. Xu Y*, et al.* Nickel Nanoparticles Encapsulated in Few - Layer Nitrogen - Doped Graphene Derived from Metal – Organic Frameworks as Efficient Bifunctional Electrocatalysts for Overall Water Splitting. *Advanced Materials* **29**, 1605957 (2017).

73. JIang T, Bu F, Feng X, SHakir I, Hao G, Xu Y. Porous Fe_2O_3 Nanoframeworks Encapsulated within Three-Dimensional Graphene as High-Performance Flexible Anode for Lithium-Ion Battery. *ACS Nano* **11**, 5140-5147 (2017).

74. Bae S, Kim J, Randriamahazaka H, Moon S, Park J, Oh I. Seamlessly Conductive 3D Nanoarchitecture of Core – Shell Ni - Co Nanowire Network for Highly Efficient Oxygen Evolution. *Advanced Energy Materials* **7**, 1601492 (2017).

75. Pu Z, Amiinu I, Zhang C, Wang M, Kou Z, Mu S. Phytic acid-derivative transition metal phosphides encapsulated in N,P-codoped carbon: an efficient and durable hydrogen evolution electrocatalyst in a wide pH range. *Nanoscale* **9**, 3555-3560 (2017).

76. Zhang H*, et al.* Active Sites Implanted Carbon Cages in Core-Shell Architecture: Highly Active and Durable Electrocatalyst for Hydrogen Evolution Reaction. *ACS nano* **10**, 684-694 (2016).

77. Tabassum H*, et al.* Metal-Organic Frameworks Derived Cobalt Phosphide Architecture

Encapsulated into B/N Co-Doped Graphene Nanotubes for All pH Value Electrochemical Hydrogen Evolution. *Advanced Energy Materials* **7**, 1601671 (2017).

78. Deng J, Deng D, Bao X. Robust catalysis on 2D materials encapsulating metals: concept, application, and perspective. *Advanced Materials* **29**, 1606967 (2017).

79. Hu K*, et al.* Graphene layer encapsulation of non-noble metal nanoparticles as acid-stable hydrogen evolution catalysts. *ACS Energy Letters* **3**, 1539-1544 (2018).

80. Ito Y*, et al.* Cooperation between holey graphene and NiMo alloy for hydrogen evolution in an acidic electrolyte. *ACS Catalysis* **8**, 3579-3586 (2018).

81. Tavakkoli M*, et al.* Single - shell carbon - encapsulated iron nanoparticles: synthesis and high electrocatalytic activity for hydrogen evolution reaction. *Angewandte Chemie International Edition* **54**, 4535-4538 (2015).

82. Wang S*, et al.* Molybdenum-carbide-modified nitrogen-doped carbon vesicle encapsulating nickel nanoparticles: a highly efficient, low-cost catalyst for hydrogen evolution reaction. *Journal of the American Chemical Society* **137**, 15753-15759 (2015).

83. Lozada-Hidalgo M*, et al.* Sieving hydrogen isotopes through two-dimensional crystals. *Science* **351**, 68-70 (2016).

84. Miao M, Nardelli MB, Wang Q, Liu Y. First principles study of the permeability of graphene to hydrogen atoms. *Physical Chemistry Chemical Physics* **15**, 16132-16137 (2013).

85. Wang WL, Kaxiras E. Graphene hydrate: theoretical prediction of a new insulating form of graphene. *New Journal of Physics* **12**, 125012 (2010).

86. Koenig SP, Wang L, Pellegrino J, Bunch JS. Selective molecular sieving through porous graphene. *Nature nanotechnology* **7**, 728-732 (2012).

87. Berry V. Impermeability of graphene and its applications. *Carbon* **62**, 1-10 (2013).

88. Tavakkoli M*, et al.* Single-Shell Carbon-Encapsulated Iron Nanoparticles: Synthesis and High Electrocatalytic Activity for Hydrogen Evolution Reaction. *Angewandte Chemie International Edition* **54**, 4535-4538 (2015).

89. Zhou W*, et al.* N-Doped Carbon-Wrapped Cobalt Nanoparticles on N-Doped Graphene Nanosheets for High-Efficiency Hydrogen Production. *Chemistry of Materials* **27**, 2026-2032 (2015).

90. Wang J, Xu F, Jin H, Chen Y, Wang Y. Non-Noble Metal Based Carbon Composites in

Hydrogen Evolution Reaction: Fundamentals to Applications. *Advanced Materials* **29**, 1605838 (2017).

91. Nørskov JK*, et al.* Trends in the exchange current for hydrogen evolution. *Journal of The Electrochemical Society* **152**, J23-J26 (2005).

92. Medford AJ*, et al.* From the Sabatier principle to a predictive theory of transition-metal heterogeneous catalysis. *Journal of Catalysis* **328**, 36-42 (2015).

93. Durst J, Siebel A, Simon C, Hasche F, Herranz J, Gasteiger H. New insights into the electrochemical hydrogen oxidation and evolution reaction mechanism. *Energy & Environmental Science* **7**, 2255-2260 (2014).

94. Wang J, Xu F, Jin H, Chen Y, Wang Y. Non - Noble Metal - based Carbon Composites in Hydrogen Evolution Reaction: Fundamentals to Applications. *Advanced materials* **29**, 1605838 (2017).

95. Gabe D. The centenary of Tafel's equation. *Transactions of the IMF* **83**, 121-124 (2005).

96. Fang Y-H, Liu Z-P. Tafel kinetics of electrocatalytic reactions: from experiment to first-principles. *ACS Catalysis* **4**, 4364-4376 (2014).

97. Koper MT. Analysis of electrocatalytic reaction schemes: distinction between rate-determining and potential-determining steps. *Journal of Solid State Electrochemistry* **17**, 339-344 (2013).

98. Grimminger J, Schmickler W. Dynamics of combined electron-and proton transfer at metal electrodes. *Chemical physics* **334**, 8-17 (2007).

99. Mohr J-H, Schmickler W. Exactly solvable quantum model for electrochemical electron-transfer reactions. *Physical review letters* **84**, 1051 (2000).

100. Yuan X-ZR, Song C, Wang H, Zhang J. *Electrochemical impedance spectroscopy in PEM fuel cells: fundamentals and applications*. Springer Science & Business Media (2009).

101. Zhang Y, Zhang L, Zhou C. Review of chemical vapor deposition of graphene and related applications. *Accounts of chemical research* **46**, 2329-2339 (2013).

102. Yu Q, Lian J, Siriponglert S, Li H, Chen YP, Pei S-S. Graphene segregated on Ni surfaces and transferred to insulators. *Applied Physics Letters* **93**, 113103 (2008).

103. Berger C*, et al.* Electronic confinement and coherence in patterned epitaxial graphene. *Science* **312**, 1191-1196 (2006).

104. Liang X, Fu Z, Chou SY. Graphene transistors fabricated via transfer-printing in device active-areas on large wafer. *Nano letters* **7**, 3840-3844 (2007).

105. Gómez-Navarro C*, et al.* Electronic transport properties of individual chemically reduced graphene oxide sheets. *Nano letters* **7**, 3499-3503 (2007).

106. Li X, Wang X, Zhang L, Lee S, Dai H. Chemically derived, ultrasmooth graphene nanoribbon semiconductors. *science* **319**, 1229-1232 (2008).

107. Li X*, et al.* Large-area synthesis of high-quality and uniform graphene films on copper foils. *science* **324**, 1312-1314 (2009).

108. Li X, Cai W, Colombo L, Ruoff RS. Evolution of graphene growth on Ni and Cu by carbon isotope labeling. *Nano letters* **9**, 4268-4272 (2009).

109. Jothi PR, Kannan S, Velayutham G. Enhanced methanol electro-oxidation over in-situ carbon and graphene supported one dimensional NiMoO4 nanorods. *Journal of Power Sources* **277**, 350-359 (2015).

110. Lukowski M, Daniel A, Meng F, Forticaux A, Li L, Jin S. Enhanced Hydrogen Evolution Catalysis from Chemically Exfoliated Metallic MoS2 Nanosheets. *Journal of the American Chemical Society* **135**, 10274-10277 (2013).

111. Benck J, Chen Z, Kuritzky L, Forman A, Jaramillo T. Amorphous molybdenum sulfide catalysts for electrochemical hydrogen production: insights into the origin of their catalytic activity. *ACS Catalysis* **9**, 1916-1923 (2012).

112. Kibsgaard J*, et al.* Designing an improved transition metal phosphide catalyst for hydrogen evolution using experimental and theoretical trends. *Energy & Environmental Science* **8**, 3022-3029 (2015).

113. Conway B, Tilak B. Interfacial processes involving electrocatalytic evolution and oxidation of H2, and the role of chemisorbed H. *Electrochimica Acta* **47**, 3571-3594 (2002).

114. Kresse G, Hafner J. Norm-conserving and ultrasoft pseudopotentials for first-row and transition elements. *Journal of Physics: Condensed Matter* **6**, 8245 (1994).

115. Blöchl P. Projector augmented-wave method. *Phys Rev B* **50**, 17953-17979 (1994).

116. Perdew J, Burke K, Ernzerhof M. Generalized gradient approximation made simple. *Phys Rev Lett* **77**, 3865-3868 (1996).

117. Grimme S, Antony J, Ehrlich S, Krieg H. A consistent and accurate ab initio parametrization of density functional dispersion correction (DFT-D) for the 94 elements H-Pu. *Chem Phys* **132**, 154104 (2010).

118. Grimme S, Ehrlich S, Goerigk L. Effect of the damping function in dispersion corrected density functional theory. *Journal of Computational Chemistry* **32**, 1456-1465 (2011).

119. Shoemaker C, Shoemaker D. The crystal structure of the δ phase Mo-Ni. *Acta Crystallographica* **16**, 997-1009 (1963).

120. Wang Y, Woodward C, Zhou S, Liu Z, Chen L. Structural stability of Ni-Mo compounds from first-principles calculations. *Scripta Matrialia* **52**, 17-20 (2005).

121. Kondo T*, et al.* Atomic-scale characterization of nitrogen-doped graphite: Effects of dopant nitrogen on the local electronic structure of the surrounding carbon atoms. *Phys Rev B* **86**, 035436 (2012).

122. Shoemaker Ct, Shoemaker D. The crystal structure of the δ phase Mo–Ni. *Acta Crystallographica* **16**, 997-1009 (1963).

123. Wang Y, Woodward C, Zhou S, Liu Z-K, Chen L-Q. Structural stability of Ni–Mo compounds from first-principles calculations. *Scripta Materialia* **52**, 17-20 (2005).

124. Wertheim GK, Wernick JH, Crecelius G. Surface effects on valence in rare-earth intermetallic compounds. *Physical Review B* **18**, 875 (1978).

125. Roustila A, Severac C, Chêne J, Percheron-Guégan A. Hydrogen effects on the electronic and microstructural properties of Ce, Ni, and $CeNi_2$ intermetallic compound. *Surface Science* **311**, 33-44 (1994).

126. Lebugle A, Axelsson U, Nyholm R, Mårtensson N. Experimental L and M core level binding energies for the metals ^{22}Ti to ^{30}Zn. *Physica Scripta* **23**, 825-827 (1981).

127. Brainard WA, Wheeler DR. An XPS study of the adherence of refractory carbide silicide and boride rf-sputtered wear-resistant coatings. *Journal of Vacuum Science & Technology* **15**, 1800-1805 (1978).

128. Bianchi CL, Cattania MG, Villa P. XPS characterization of Ni and Mo oxides before and after "in situ" treatments. *Applied Surface Science* **70**, 211-216 (1993).

129. Takano I, Isobe S, Sasaki TA, Baba Y. Nitrogenation of various transition metals by N^{+2}-ion implantation. *Applied Surface Science* **37**, 25-32 (1989).

130. Conway BE, Tilak BV. Interfacial processes involving electrocatalytic evolution and

oxidation of H_2, and the role of chemisorbed H. *Electrochimica acta* **47**, 3571-3594 (2002).

131. Liang ZX, Ahn HS, Bard AJ. A study of the mechanism of the hydrogen evolution reaction on nickel by surface interrogation scanning electrochemical microscopy. *Journal of the American Chemical Society* **139**, 4854-4858 (2017).

132. Hu K, Jeong S, Wakisaka M, Fujita J, Ito Y. Bottom-Up Synthesis of Porous NiMo Alloy for Hydrogen Evolution Reaction. *Metals* **8**, 83 (2018).

133. Ito Y*, et al.* High-Quality Three-Dimensional Nanoporous Graphene. *Angew Chem Int Ed* **53**, 4822-4826 (2014).

134. Chen YY*, et al.* Self - Templated Fabrication of MoNi4/MoO3 - x Nanorod Arrays with Dual Active Components for Highly Efficient Hydrogen Evolution. *Advanced Materials* **29**, 1703311 (2017).

135. Bianchi CL, Cattania MG, Villa P. XPS characterization of Ni and Mo oxides before and after "in situ" treatments. *Applied surface science* **70**, 211-216 (1993).

136. Ito Y, Qiu HJ, Fujita T, Tanabe Y, Tanigaki K, Chen M. Bicontinuous nanoporous N - doped graphene for the oxygen reduction reaction. *Advanced Materials* **26**, 4145-4150 (2014).

137. Ito Y, Christodoulou C, Nardi MV, Koch N, Sachdev H, Müllen K. Chemical vapor deposition of N-doped graphene and carbon films: the role of precursors and gas phase. *ACS nano* **8**, 3337-3346 (2014).

138. Sheng W, Gasteiger H, Shao-Horn Y. Hydrogen Oxidation and Evolution Reaction Kinetics on Platinum: Acid vs Alkaline Electrolytes. *Journal of The Electrochemical Sociery* **157**, B1529-B1536 (2010).

139. Zou X, Zhang Y. Noble Metal-Free Hydrogen Evolution Catalysts for Water Splitting. *Chemical Society Reviews* **44**, 5148-5180 (2015).

140. Nørskov JK, Bligaard T, Rossmeisl J, Christensen CH. Towards the computational design of solid catalysts. *Nature chemistry* **1**, 37 (2009).

141. Tsai C, Abild-Pedersen F, Nørskov JK. Tuning the MoS2 edge-site activity for hydrogen evolution via support interactions. *Nano letters* **14**, 1381-1387 (2014).

142. Zheng Y*, et al.* Toward design of synergistically active carbon-based catalysts for electrocatalytic hydrogen evolution. *ACS nano* **8**, 5290-5296 (2014).

143. Liu L, Chen W, Li Y. An overview of the proton conductivity of nafion membranes through a statistical analysis. *Journal of membrane science* **504**, 1-9 (2016).

144. Ji H*, et al.* Capacitance of carbon-based electrical double-layer capacitors. *Nature communications* **5**, 3317 (2014).

145. Mauritz KA, Moore RB. State of understanding of Nafion. *Chemical reviews* **104**, 4535-4586 (2004).

146. Sun Z, Yan Z, Yao J, Beitler E, Zhu Y, Tour JM. Growth of graphene from solid carbon sources. *Nature* **468**, 549 (2010).

147. Hao Y*, et al.* Probing layer number and stacking order of few - layer graphene by Raman spectroscopy. *small* **6**, 195-200 (2010).

148. Jin Z, Yao J, Kittrell C, Tour JM. Large-scale growth and characterizations of nitrogen-doped monolayer graphene sheets. *Acs Nano* **5**, 4112-4117 (2011).

149. Zan R, Bangert U, Ramasse Q, Novoselov K. Imaging of Bernal stacked and misoriented graphene and boron nitride: experiment and simulation. *Journal of microscopy* **244**, 152-158 (2011).

150. Zhao H*, et al.* Growth and Raman spectra of single-crystal trilayer graphene with different stacking orientations. *ACS nano* **8**, 10766-10773 (2014).

151. Lin Y-C, Teng P-Y, Yeh C-H, Koshino M, Chiu P-W, Suenaga K. Structural and chemical dynamics of pyridinic-nitrogen defects in graphene. *Nano letters* **15**, 7408-7413 (2015).

152. Henkelman G, Uberuaga BP, Jónsson H. A climbing image nudged elastic band method for finding saddle points and minimum energy paths. *The Journal of chemical physics* **113**, 9901-9904 (2000).

153. Lusk MT, Wu DT, Carr LD. Graphene nanoengineering and the inverse Stone-Thrower-Wales defect. *Physical Review B* **81**, 155444 (2010).

154. Jia Y*, et al.* Defect graphene as a trifunctional catalyst for electrochemical reactions. *Advanced Materials* **28**, 9532-9538 (2016).

155. Jiao Y, Zheng Y, Davey K, Qiao S-Z. Activity origin and catalyst design principles for electrocatalytic hydrogen evolution on heteroatom-doped graphene. *Nature Energy* **1**, 16130 (2016).